AGU PUBLICATIONS

Reviews of Geophysics

REVIEW ARTICLE
10.1002/2015RG000511

Key Points:
- First comprehensive review of stratospheric aerosol since 2006
- Differences between in situ and space-based inferences of stratospheric aerosol properties have been resolved
- Improved understanding of the role of minor volcanic eruptions and nonsulfate aerosols on the stratospheric aerosol layer has been achieved

Correspondence to:
S. Kremser,
stefanie@bodekerscientific.com

Citation:
Kremser, S., et al. (2016), Stratospheric aerosol—Observations, processes, and impact on climate, *Rev. Geophys.*, *54*, 278–335, doi:10.1002/2015RG000511.

Received 9 NOV 2015
Accepted 17 MAR 2016
Accepted article online 24 MAR 2016
Published online 7 MAY 2016

Stratospheric aerosol—Observations, processes, and impact on climate

Stefanie Kremser[1], Larry W. Thomason[2], Marc von Hobe[3], Markus Hermann[4], Terry Deshler[5], Claudia Timmreck[6], Matthew Toohey[6,7], Andrea Stenke[8], Joshua P. Schwarz[9], Ralf Weigel[10], Stephan Fueglistaler[11,12], Fred J. Prata[13], Jean-Paul Vernier[2], Hans Schlager[14], John E. Barnes[15], Juan-Carlos Antuña-Marrero[16], Duncan Fairlie[2], Mathias Palm[17], Emmanuel Mahieu[18], Justus Notholt[17], Markus Rex[19], Christine Bingen[20], Filip Vanhellemont[20], Adam Bourassa[21], John M. C. Plane[22], Daniel Klocke[23], Simon A. Carn[24], Lieven Clarisse[25], Thomas Trickl[26], Ryan Neely[27,28], Alexander D. James[22], Landon Rieger[21], James C. Wilson[29], and Brian Meland[29]

[1]Bodeker Scientific, Alexandra, New Zealand, [2]NASA Langley Research Center, Hampton, Virginia, USA, [3]Forschungszentrum Jülich GmbH, Institute of Energy and Climate Research, Jülich, Germany, [4]Leibniz Institute for Tropospheric Research, Leipzig, Germany, [5]Department of Atmospheric Science, University of Wyoming, Laramie, Wyoming, USA, [6]Max Planck Institute for Meteorology, Hamburg, Germany, [7]GEOMAR Helmholtz Centre for Ocean Research Kiel, Kiel, Germany, [8]ETH Zurich, Zurich, Switzerland, [9]NOAA Earth System Research Laboratory, Boulder, Colorado, USA, [10]Institute for Physics of the Atmosphere, Johannes Gutenberg University, Mainz, Germany, [11]Department of Geosciences, Princeton University, Princeton, New Jersey, USA, [12]Program in Atmospheric and Oceanic Sciences, Princeton University, Princeton, New Jersey, USA, [13]Nicarnica Aviation, Kjeller, Norway, [14]Institute of Atmospheric Physics, Deutsches Zentrum fuer Luft- und Raumfahrt, Cologne, Germany, [15]Mauna Loa Observatory, NOAA, Hilo, Hawaii, USA, [16]Meteorological Institute of Cuba, Camagüey, Cuba, [17]IUP University of Bremen, Bremen, Germany, [18]Institute of Astrophysics and Geophysics, University of Liège, Liège, Belgium, [19]Helmholtz Center for Polar and Marine Research, Alfred Wegener Institute, Potsdam, Germany, [20]Royal Belgian Institute for Space Aeronomy, Brussels, Belgium, [21]Institute of Space and Atmospheric Studies, University of Saskatchewan, Saskatoon, Saskatchewan, Canada, [22]School of Chemistry, University of Leeds, Leeds, UK, [23]Deutscher Wetterdienst, Offenbach, Germany, [24]Department of Geological and Mining Engineering and Sciences, Michigan Technology University, Houghton, Michigan, USA, [25]Service de Chimie Quantique et Photophysique, Université libre de Bruxelles, Brussels, Belgium, [26]IMK-IFU, Karlsruher Institut für Technologie, Karlsruhe, Germany, [27]School of Earth and Environment, University of Leeds, Leeds, UK, [28]National Centre for Atmospheric Science, School of the Earth and Environment, University of Leeds, Leeds, UK, [29]Department of Mechanical and Materials Engineering, University of Denver, Denver, Colorado, USA

Abstract Interest in stratospheric aerosol and its role in climate have increased over the last decade due to the observed increase in stratospheric aerosol since 2000 and the potential for changes in the sulfur cycle induced by climate change. This review provides an overview about the advances in stratospheric aerosol research since the last comprehensive assessment of stratospheric aerosol was published in 2006. A crucial development since 2006 is the substantial improvement in the agreement between in situ and space-based inferences of stratospheric aerosol properties during volcanically quiescent periods. Furthermore, new measurement systems and techniques, both in situ and space based, have been developed for measuring physical aerosol properties with greater accuracy and for characterizing aerosol composition. However, these changes induce challenges to constructing a long-term stratospheric aerosol climatology. Currently, changes in stratospheric aerosol levels less than 20% cannot be confidently quantified. The volcanic signals tend to mask any nonvolcanically driven change, making them difficult to understand. While the role of carbonyl sulfide as a substantial and relatively constant source of stratospheric sulfur has been confirmed by new observations and model simulations, large uncertainties remain with respect to the contribution from anthropogenic sulfur dioxide emissions. New evidence has been provided that stratospheric aerosol can also contain small amounts of nonsulfate matter such as black carbon and organics. Chemistry-climate models have substantially increased in quantity and sophistication. In many models the implementation of stratospheric aerosol processes is coupled to radiation and/or stratospheric chemistry modules to account for relevant feedback processes.

1. Introduction

The presence of primarily aqueous sulfuric acid aerosol in the stratosphere during a period not associated with volcanic activity was first observed by Christian Junge and coworkers [*Chagnon and Junge*, 1961; *Junge and Manson*, 1961]. Rather than being distributed throughout the entire middle atmosphere, the measurements

showed that stratospheric aerosol occurs in a distinct layer between 15 and 25 km altitude with a peak near 20 km [*Junge et al.,* 1961] that extends over a broad range of latitudes [*Hofmann et al.,* 1975]. Strictly, an aerosol is defined as a suspension of fine particles in a gas; however, following common usage, we use "aerosol" to refer to the particle component only [*Seinfeld and Pandis*, 2006]. In this paper, using aerosol refers to a population of similarly composed particles, while using aerosols refers to collections of aerosol, in which composition may vary. The top of the stratospheric aerosol layer is mainly determined by sedimentation and evaporation of the aerosol due to stratospheric temperatures rising with altitude [*Hofmann et al.,* 1985]. The base of the aerosol layer is commonly associated with the tropopause since upper tropospheric aerosol levels are often much lower than in the stratosphere. The stratospheric aerosol layer is often referred to as the "Junge layer."

Understanding the processes controlling stratospheric aerosol formation and residence in the stratosphere is tightly bound to understanding the processes governing sulfur in the stratosphere. Stratospheric sulfur is found in a variety of gaseous molecules, such as carbonyl sulfide (OCS), sulfur dioxide (SO_2), and sulfuric acid (H_2SO_4), but about 25% of the sulfur resides in sulfuric acid/water (H_2SO_4-H_2O) solution droplets [*SPARC*, 2006]. This solution dominates the composition of stratospheric aerosol, supplemented by smaller amounts of meteoritic and other nonsulfate material. While a contribution from anthropogenic SO_2 emissions has been intensely debated since the early 1990s, the stratospheric sulfur and aerosol budget are clearly dominated by natural sources, such as direct volcanic injections of large amounts of SO_2 and aerosols, which stand out as the largest source over the past decades.

The primary factor controlling stratospheric aerosol variability is episodic but powerful volcanic eruptions injecting sulfur directly into the lower stratosphere. That volcanically derived aerosols have global effects was first noted in the worldwide observation of optical phenomena after the 1883 eruption of Krakatau [*Simkin and Fiske*, 1983]. Tambora, an earlier cataclysmic eruption, is believed to have caused "the year without summer" in 1816. The Mount Pinatubo eruption in 1991 increased the stratospheric sulfur burden by as much as a factor of 60 above nonvolcanic levels, with the levels remaining elevated by a factor of 10 well into 1993 [*McCormick et al.,* 1995]. After the eruption of Pinatubo it was first hypothesized [*Hansen et al.,* 1992] and later demonstrated in climate records [*Robock and Mao*, 1995] that the impact of strong volcanic eruptions on surface temperature is a cooling on the order of a few tenths of a degree Celsius. Recently, it was further shown that the stratospheric aerosol layer is also modulated by weaker eruptions, and that these modulations have had a small but significant impact on global surface temperatures [*Solomon et al.,* 2011].

SPARC (Stratosphere-troposphere Processes And their Role in Climate), a core project of the World Climate Research Programme, published the Assessment of Stratospheric Aerosol Properties in 2006 [*SPARC*, 2006], which summarized the state of knowledge of stratospheric aerosol, their primary sulfurous precursors, and the scientific advancements in making atmospheric measurements and modeling. Perhaps, the most enduring outcome of this effort was bringing together the in situ, ground-based, and space-based aerosol measurement community with the climate modeling community. This joint community has endured and is now organized as the SPARC Stratospheric Sulfur and its Role in Climate (SSiRC) activity.

One outcome of the collaboration between these communities is the creation of global stratospheric aerosol climatology of optical and other bulk properties such as aerosol surface area density (SAD, which is the total surface area of aerosol in a unit volume of air) for the period from 1979 to 2002, which is currently extended to span 1960 to 2011. This data set remains, with further developments, to be a crucial forcing input to many chemistry-climate model initiatives and coupled model intercomparison projects. A significant challenge to the creation of the stratospheric aerosol climatology was the finding that, during nonvolcanic periods, the extinction coefficients calculated from in situ measurements are systematically lower by more than a factor of 2 relative to space-based measurements, and that SAD calculations from space-based measurements were often lower by a similar factor compared to in situ observations [*SPARC*, 2006]. With no mechanism to understand these discrepancies, the climatology produced manifested these uncertainties [*SPARC*, 2006]. Another effort was to understand trends in stratospheric aerosol, away from volcanic influences, by using instrument-based measurements, as opposed to a derived aerosol property like aerosol mass, from a number of ground, balloon, and space-based platforms. Despite limited periods without volcanic influence, the analysis of nonvolcanic stratospheric aerosol indicated that there was no long-term trend in background (nonvolcanic) aerosol levels.

A significant part of the *SPARC* [2006] report was conducting thorough comparisons of a number of chemistry-climate models and aerosol observations by a number of in situ and space-based instruments. For instance, model simulations and satellite observations of aerosol extinction coefficient after major volcanic eruptions agreed fairly well for visible wavelengths but not in the infrared. In this paper, we will refer to "major volcanic eruptions" as volcanic eruptions that inject more than 1 Tg of sulfur into the stratosphere, such as the eruption of El Chichón in 1982 or Mount Pinatubo in 1991. Model results showed some other deficiencies such as the inability to reproduce the vertical distribution of aerosol between 17 and 20 km altitude. To some extent, the quality of these comparisons was hampered by the limited availability of measurements of key precursors like OCS, SO_2, and primary aerosol; aerosol formed in the troposphere and transported into the stratosphere. This was particularly true for SO_2, where the lack of SO_2 measurements in the upper troposphere and stratosphere hindered the understanding of the role of human activities on stratospheric aerosol. While there was speculation that SO_2 from global emissions and, in particular, those from developing countries in low latitudes, such as China, could be influencing stratospheric aerosol levels, evidence for this SO_2 presence in the upper troposphere and its subsequent transport across the tropical tropopause was lacking. While the model simulations exhibited their own deficiencies in aerosol morphology, they tended to support the concept that the space-based data sets of SAD underestimated aerosol surface area density in the lower stratosphere during low aerosol loading periods. In general, disagreements between the various data sets and model simulations indicated that significant questions remain regarding the ability to characterize stratospheric aerosol during volcanically quiescent periods, in particular, in the lower stratosphere.

Over the past decade, there has been considerable progress in addressing some of the unanswered science questions indicated in the key findings of the *SPARC* [2006] report. The scientific progress that has been achieved since 2006 is the foundation of this review, along with identifying the outstanding questions related to stratospheric aerosol.

An interest has developed for the purposeful modification of the stratospheric aerosol layer for solar radiation management, often referred to as geoengineering. This topic is not covered in this review as there are a significant number of recent modeling studies exploring the possibility of solar radiation management by artificially enhancing the amount of stratospheric aerosol [e.g., *English et al.,* 2012; *Niemeier and Timmreck*, 2015]. Furthermore, stratospheric aerosol and thus indirectly sulfur play a significant role in the global stratosphere by hosting heterogeneous chemical reactions with profound consequences for the midlatitude ozone layer [*Fahey et al.,* 1993; *Mills et al.,* 1993]. In the high-latitude cold winter stratosphere the H_2SO_4-H_2O droplets will grow into liquid and solid polar stratospheric cloud (PSC) particles and host rapid chlorine activating reactions. While these processes are important and related to aerosol, this review does not address the specifics of the role of stratospheric aerosol in the chemical processes of the stratosphere and the impact of stratospheric aerosol on PSCs as there is a project underway to complete a separate review of PSCs under the auspices of SPARC.

The paper is organized as follows: Section 2 presents an overview about the dynamical, chemical, and microphysical processes that are relevant to stratospheric aerosol. The volcanic and nonvolcanic sources of stratospheric aerosol will be discussed in section 3. A short summary and the latest advancements in atmospheric in situ, ground-based, and satellite-based measurements will be presented in section 4 followed by an overview about the observed changed in stratospheric aerosol (section 5). Section 6 addresses the latest developments in modeling stratospheric aerosol and its impact on climate with state-of-the-art climate models. The highlights in stratospheric aerosol research and main advances since the latest stratospheric aerosol assessments are summarized in section 7, the conclusions of this paper.

2. Overview of the Processes Relevant to Stratospheric Aerosol

The life cycle and aerosol distribution in the stratosphere is governed by a complex interplay of (i) atmospheric transport, including troposphere to stratosphere exchange through direct injections such as volcanic eruptions and transport of tropospheric precursor gases across the tropical tropopause layer (TTL), and stratospheric transport through the large-scale Brewer-Dobson Circulation (BDC) and (ii) chemistry and microphysics, including aerosol formation, growth, and removal, through sedimentation and in air traversing the extratropical tropopause. An overview of these processes is given below, followed by more detailed descriptions on how various source gases and processes contribute to stratospheric aerosol (section 3). Figure 1 illustrates the relevant processes that govern the life cycle and distribution of stratospheric aerosol.

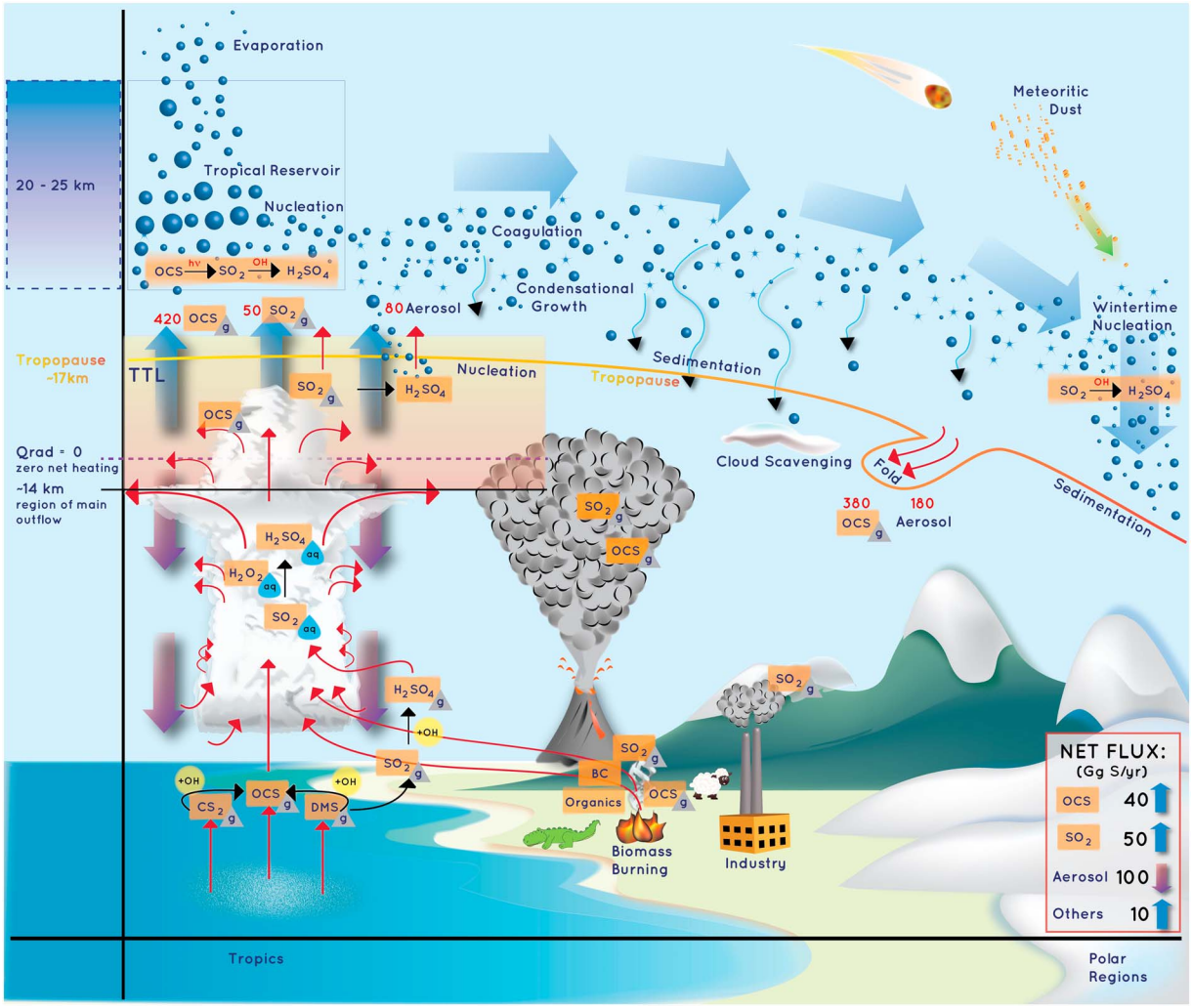

Figure 1. Schematic of the relevant processes that govern the stratospheric aerosol life cycle and distribution. The large blue arrows indicate the large-scale circulation, while the red arrows indicate transport processes. The black arrows indicate chemical conversions between compounds. The different chemical species are marked as either gas phase (grey triangle) or aqueous phase (blue drop). The blue thin arrows represent sedimentation of aerosol from the stratosphere to the troposphere. Note that due to its long tropospheric lifetime, carbonyl sulfide (OCS) does not necessarily require deep convection to be transported into the TTL (as shown in the figure). The red numbers represent the flux of OCS and sulfur dioxide (SO_2) as well as the flux of aerosol in Gg S/yr based on model simulations from *Sheng et al.* [2015]. The approximate net flux of sulfur containing compounds across the tropopause is shown in the grey box [*Sheng et al.*, 2015], where the 10 Gg S/yr contribution from "others" can be mostly attributed to dimethyl sulfide (DMS) and hydrogen sulfide (H_2S). Other chemical compounds shown in this figure are carbon disulfide (CS_2), sulfuric acid (H_2SO_4), and black carbon (BC). The sulfur chemistry is described in more detail in section 2, while the role and importance of the sulfur compounds in maintaining the stratospheric aerosol layer are described in more detail in section 3.

2.1. Atmospheric Transport

Apart from volcanic eruptions that directly inject sulfur into the stratosphere, precursors of stratospheric aerosol enter the stratosphere from the troposphere through three distinct pathways: (i) quasi-isentropic transport from the TTL into the extratropical lowermost stratosphere, (ii) cross-isentropic transport from the TTL into the tropical stratosphere by slow radiatively driven ascent, and (iii) direct injection of air into the stratosphere by exceptional overshooting convection that sometimes crosses the tropopause in the tropics (not shown in Figure 1).

For (i) and (ii) the TTL is the major source region of air. The tropical tropospheric circulation is a balance between localized diabatic upward transport predominantly in moist convection and large-scale radiative subsidence. The transition from the tropospheric large-scale radiative subsidence to dynamically and/or radiatively forced large-scale ascent occurs some distance, about 2 km, or 30 K in potential temperature, below the tropical cold point tropopause [*Folkins et al.*, 1999; *Fueglistaler et al.*, 2009], the temperature minimum between the

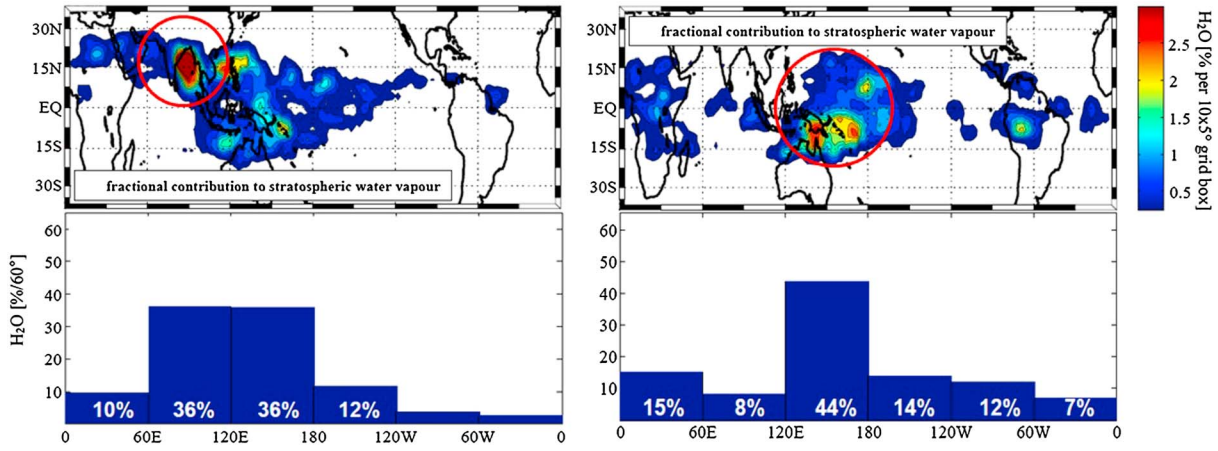

Figure 2. (top row) The density of "Lagrangian Cold Points" (LCPs) acquired by air parcels in a Lagrangian calculation, expressed by the fractional contribution to stratospheric water vapor from different geographical areas (percentage contribution per individual 10° × 5° grid box). (bottom row) The longitudinal distribution of the water vapor entry, i.e., the values from the upper panels integrated over latitude. (left column) Typical Northern Hemispheric summer (1996). (right column) Typical Northern Hemispheric winter (1995/1996). Red circles highlight the key region for transport into the stratosphere in summer and winter. (Figure is adapted from *Kremser et al.* [2009]).

troposphere and stratosphere. Consequently, to reach the stratosphere, air in moist convection must cross the level of "zero net radiative heating" ($Q_{rad} = 0$), located at about 15.5 km [*Folkins et al.,* 1999]. Air detraining from deep convection above the $Q_{rad} = 0$ level experiences further diabatic ascent, and those air masses that remain within the tropics where $Q_{rad} > 0$ can enter the stratosphere (Figure 1). The subsequent cross-isentropic ascent is slow, and it may take weeks to months to cross the cold point tropopause. Heterogeneity in radiatively active trace constituents (mainly water vapor and clouds) induces heterogeneity in radiative heating rates which in turn leads to dispersion [*Tzella and Legras*, 2011; *Bergman et al.,* 2012a], and the Eulerian climatological mean $Q_{rad} = 0$ level is primarily useful as a concept rather than as a unique physical locale. For a more detailed discussion see the review by *Fueglistaler et al.* [2009].

During the slow cross-isentropic ascent of air in the tropics to the cold point tropopause the temperature decreases. The corresponding decrease in water vapor saturation mixing ratio allows ongoing dehydration and concomitant washout of soluble species, while insoluble or weakly soluble species can reach the stratosphere with little loss. In contrast, very deep convection can transport cloudy air from the troposphere to above the cold point tropopause in a very short time, and consequently detrained air and associated aerosol and aerosol precursors are not washed out while ascending into the stratosphere. While overshooting convection is thought to be highly efficient locally in supplying tropospheric air to the stratosphere, its importance relative to the radiatively balanced slow ascent remains poorly quantified. Satellite observations by the Cloud-Aerosol Lidar with Orthogonal Polarization (CALIOP) showed very low aerosol loading up to 20 km during the Southern Hemisphere convective season, suggesting efficient transport of clean tropospheric air in the southern tropics up to and above the tropopause, affecting aerosol concentrations up to the lower stratosphere [*Vernier et al.,* 2011a]. Sparse in situ tracer measurements [*Corti*, 2008], and studies with cloud-resolving numerical models [*Jensen et al.,* 2007; *Chemel et al.,* 2009; *Hassim and Lane*, 2010; *Frey et al.,* 2015], show that very intense convection may indeed penetrate the tropical tropopause into the lower stratosphere, but reliable upscaling from individual storms to the entire tropics remains unsolved.

The pronounced zonal asymmetry of tropical tropospheric dynamics, convection, and tropopause temperatures illustrate the distinct, seasonally varying geographic patterns of transport into the stratosphere. For water vapor and sulfur/aerosol-related species that are subject to washout, the characteristics of the most recent dehydration event of air entering the stratosphere are more relevant than the properties of the conventionally defined tropopause (lapse rate or cold point). The "Lagrangian Cold Point" (LCP) [*Fueglistaler et al.,* 2005]—the point where an air mass experiences the lowest temperature during ascent into the stratosphere—is a useful idealization of the point of last dehydration. Figure 2 shows the density distribution of the LCPs and the relative contribution to stratospheric water vapor for a Northern Hemispheric winter and a Northern Hemispheric summer. The key pathways that determine the stratospheric composition are through the Asian Monsoon Circulation in Northern Hemispheric summer (also clearly seen in trace gas observations [*Randel et al.,* 2010]) and through

convection followed by radiatively driven ascent above the West Pacific warm pool and the maritime continent in Northern Hemispheric winter [*Fueglistaler et al.,* 2005; *Bergman et al.,* 2012a].

The Asian monsoon has attracted much attention due to the north-west shift of the upper level circulation in the TTL relative to the centers of deep convection, where air may cross the $Q_{rad} = 0$ level taking air away from the convective region where photochemical reaction along the transport of air masses may occur [*Park et al.,* 2008; *Devasthale and Fueglistaler*, 2010; *Randel et al.,* 2010; *Bergman et al.,* 2012a]. The upper level circulation of the Asian monsoon has also attracted much interest because of its role in quasi-isentropic exchange between the extratropical lower stratosphere and the TTL [*Konopka et al.,* 2009; *Abalos et al.,* 2013; *Ploeger et al.,* 2013]. This quasi-horizontal exchange takes place via mixing processes in the vicinity of the subtropical jets. While horizontal transport takes place mostly at the flanks of the circulation, the air inside the anticyclone has been found to be strongly isolated and of mainly tropospheric composition due to the convective outflow from below [*Park et al.,* 2008]. It is believed that a significant fraction of this isolated air eventually ends up in the stratosphere [*Bergman et al.,* 2012a]. Hence, the Asian monsoon anticyclone has been identified as a transport pathway for pollution from Asia to enter the stratosphere [*Randel et al.,* 2010]. Recent transport modeling studies confirm this statement and show that emissions from Asia have an impact on the composition of the lower stratospheric air masses of the Northern Hemisphere [*Vogel et al.,* 2015]. This idea is also supported by recent observations of an enhanced aerosol layer in the Asian Monsoon anticyclone (see section 5) within a few kilometers of the tropopause [*Vernier et al.,* 2011c]. However, direct observation of this material entering the stratosphere is still missing.

In the stratosphere, strong zonal winds lead to fast homogenization of aerosols and tracers in the zonal direction, while vertical and meridional transport is controlled by the BDC [*Holton et al.,* 1995; *Butchart*, 2014]. The BDC results from the breaking of upward propagating waves in the stratosphere that lead to a diabatic residual circulation [*Holton*, 2004]. The residual circulation is characterized by ascent over the tropics, poleward motion in the extratropics, and subsidence over the high latitudes, in particular over the winter polar vortex, and two-way quasi-horizontal mixing (or "stirring") over the extratropics, also referred to as the "stratospheric surf zone" [*McIntyre and Palmer*, 1983]. Both the mean residual circulation and meridional mixing control the transport of aerosols and tracers [*Shepherd*, 2002] and the stratospheric "age of air" [*Waugh and Hall*, 2002]. While meridional transport is relatively efficient within the TTL, above the TTL (from about 70 hPa, 18.5 km, upward) meridional mixing between the tropics and extratropics is suppressed, prompting the notion of a "tropical pipe" [*Plumb*, 1996] or, considering limited exchange with the extratropics, a "tropical leaky pipe" [*Neu and Plumb*, 1999]. The BDC is often further separated into a "shallow branch" up to about 70 hPa, which is active year round in the lower tropical/subtropical stratosphere of both hemispheres, and a weaker "deep branch" above 70 hPa, which occurs in the extratropical middle stratosphere in the winter hemisphere [*Plumb*, 2002]. Transport of aerosols and tracers out of the tropics depends also on the quasi-biennial oscillation (QBO) [*Baldwin et al.,* 2001], with stronger poleward transport occurring during the westerly phase of the oscillation [*Jäger*, 2005].

As a result of the slow diabatic ascent over low latitudes and diabatic descent over the high latitudes, air entering the stratosphere at low latitudes in the ascending branch of the BDC may remain in the stratosphere for years, whereas air entering the stratosphere in quasi-isentropic transport from the tropical upper troposphere into the extratropical lowermost stratosphere subsides back to the troposphere within months [*Holton et al.,* 1995]. Consequently, aerosols injected into the stratosphere by volcanoes over the midlatitude and high latitude generally remain in the hemisphere of the eruption and return to the troposphere within months (see also section 3.1.1). Aerosols injected into the tropical stratosphere above about 20 km, as, for example, by the eruptions of El Chichón (1983) and Pinatubo (1991), remain in the stratosphere for years and are eventually spread over both hemispheres [*Robock*, 2000].

Using stratospheric aerosol as a tracer of atmospheric dynamics, for example, the circulation patterns related to the QBO and the BDC, is complicated by sedimentation, particularly of ash and other large particles, and by evaporation (section 2.3). During the easterly phase of the QBO, aerosols have been observed to be confined around the equator and transported vertically as high as 35 km, while, during the westerly phase, meridional transport leads to a broadening of the tropical pipe in latitude while simultaneously producing the subtropical "horns" reported by *Trepte and Hitchman* [1992]. Ascent of volcanic plumes following several eruptions (e.g., Soufriere Hills in May 2006, Nabro in June 2011, Kelud in February 2014) from the lower tropical to middle

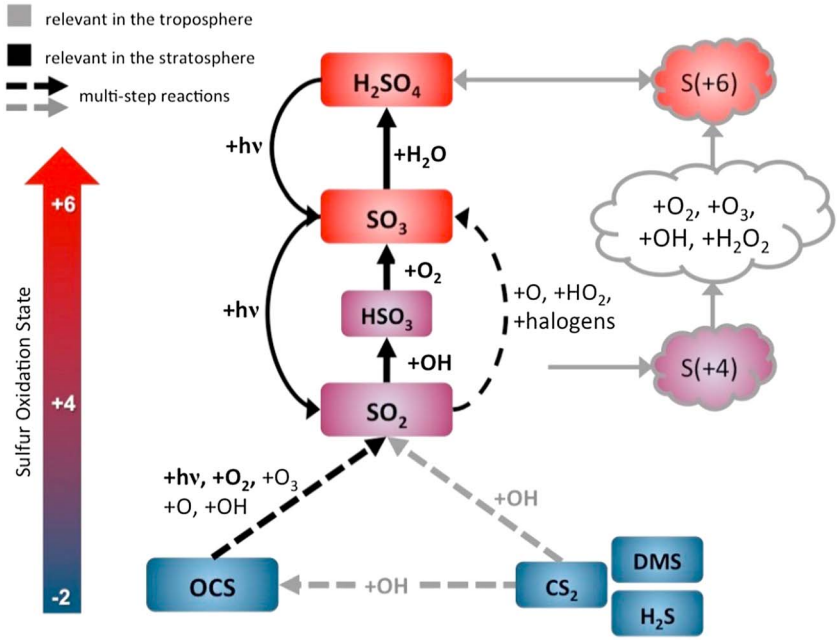

Figure 3. Primary atmospheric sulfur species and conversion reactions in gas (left part) and aqueous phase (right part). Grey arrows represent conversions mainly relevant in the troposphere, while black arrows indicate mainly stratospheric reactions. Important reactions are highlighted in bold. Several conversions involve multistep reactions (dashed) with intermediate products, which are not shown here. The color coding shows the oxidation state of the different sulfur compounds. Sulfur dioxide (SO_2) can dissolve in cloud, fog or rain droplets, and moist aerosols, where S(+4) ($= [SO_2 \cdot H_2O] + [HSO_3^-] + [SO_3^{2-}]$) can be oxidized by various substances to S(+6) ($= [H_2SO_4 \cdot H_2O] + [HSO_4^-] + [SO_4^{2-}]$). Other chemical compounds shown in this figure are carbonyl sulfide (OCS), carbon disulfide (CS_2), dimethyl sulfide (DMS), hydrogen sulfide (H_2S), hydroxyl (OH), ozone (O_3), hydrogen peroxide (H_2O_2), hydrogen sulfite (HSO_3), and sulfuric acid (H_2SO_4). For more information on the chemical reaction see section 2.2.

tropical stratosphere can also be used to derive mean diabatic ascent of the BDC [*Vernier et al.,* 2009; *Fairlie et al.,* 2014]. In the polar regions, diabatic subsidence occurring within the relatively isolated winter vortex is reflected in the very low aerosol levels observed relative to the air outside the vortex boundary [*Thomason and Poole*, 1993].

2.2. Sulfur Chemistry

Since sulfur can exist with oxidation states from −2 to +6 [*Seinfeld and Pandis*, 2006] it can form a wide variety of organic and inorganic sulfur compounds. The primary atmospheric sulfur species and conversion reactions that lead to the formation of the gaseous precursor of stratospheric sulfate aerosols, namely, sulfuric acid (H_2SO_4), are shown in Figure 3. Chemical conversions in the oxidizing Earth's atmosphere normally occur only from lower to higher oxidation states, with the exception of photodissociation reactions of oxidized sulfur compounds. Therefore, any sulfur compounds that are released into the atmosphere from surface sources and not taken up by surface sinks will ultimately be converted to H_2SO_4, which is typically condensed to aerosol in the presence of water vapor. In the troposphere, this sulfate aerosol is efficiently removed by wet and dry deposition. It is important to note that the sulfur cycle cannot be closed by atmospheric processes alone. Sulfur is used by living organisms either as fuel or as oxidizing agent in their metabolisms and as a structural component in living cells. Furthermore, biochemical reactions largely balance the atmospheric oxidation and close the global biogeochemical sulfur cycle. Without this, reduced sulfur compounds, i.e., sulfur compounds where sulfur has an oxidation state of −2, as opposed to oxidized compounds such as SO_2 or H_2SO_4, would not be present in the atmosphere in substantial amounts that are observed, and little sulfur would reach the stratosphere, except during large volcanic eruptions. This biological control on the nonvolcanic sulfur cycling can lead to complex feedback mechanisms when changes in climate induce changes to ecosystems.

In the atmosphere, most reduced sulfur compounds readily react with the hydroxyl radical (OH). Consequently, their chemical lifetimes are short, i.e., on the order of a few days or less and, thus, much shorter than the time it typically takes to transport air into the stratosphere. Many reactions are either much faster or much slower

than the transport to the stratosphere in the relevant transport regime, and uncertainties on the reaction rates are not critical for our ability to model stratospheric sulfate.

Below, we will briefly review those reactions and respective rate constants that are most critical in the context of sulfur transport to, and cycling in, the stratosphere. More complete descriptions of atmospheric sulfur chemistry can be found in *English et al.* [2011] and *Sheng et al.* [2015]. Recommended rate constants for all known sulfur reactions can be found in *Sander et al.* [2011].

The conversion from SO_2 to H_2SO_4 can proceed via different routes, and the conversion rate strongly depends on the prevailing conditions (Figure 3). In the free troposphere and lower stratosphere, reaction of SO_2 with OH dominates. The rate coefficient for this reaction recommended by *Sander et al.* [2011] has not changed recently. With a given 1σ uncertainty of less than 30% at atmospheric temperatures, the SO_2 conversion rate can be reasonably well constrained if OH concentrations are sufficiently well known. Typical SO_2 lifetimes are on the order of days to weeks [*Rex et al.,* 2014], with longer lifetimes of several weeks prevailing in the dry lower stratosphere where OH concentrations are low.

For the stratospheric sulfur budget, changes in OH concentrations within the TTL are of special interest as they can affect the SO_2 flux into the stratosphere. So far, there is little consensus about the spatial and temporal variability of OH concentrations, as measurements are limited and models show a substantial diversity in terms of simulated OH levels, spatial distributions, and calculated trends [*Naik et al.,* 2013; *Voulgarakis et al.,* 2013]. Furthermore, a study by *Park et al.* [2010] suggests that OH concentrations in the TTL are around 2 times higher (about 2×10^6 molecules/cm^3) than simulated by current state-of-the-art models. *Rex et al.* [2014] showed that OH concentrations may be substantially lower in the tropical West Pacific, compared to the tropical average, making transport of any SO_2 emitted in this region to the stratosphere more likely.

In the boundary layer, SO_2 lifetimes can be quite short under polluted conditions, for example, 19 ± 7 h in summer and 58 ± 20 h in winter in the eastern USA [*Lee et al.,* 2011]. This limits the amount of SO_2 from anthropogenic emissions being transported to the free troposphere or higher. Furthermore, uptake into cloud droplets leads to a much faster conversion of SO_2 to H_2SO_4 than in the gas phase. There are several pathways for SO_2 oxidation in aqueous phase by reaction with ozone (O_3), hydrogen peroxide (H_2O_2), oxygen (O_2) (catalyzed by iron, Fe(III), Manganese, Mn(II)), and others, with the conversion rates for O_3 and O_2 being strongly pH dependent [*Seinfeld and Pandis*, 2006]. In the presence of clouds, the tropospheric lifetime of SO_2 is reduced to days or even hours [*Lelieveld*, 1993].

Aerosol loads and concentrations of reactive chemicals can be strongly enhanced in volcanic plumes, leading to a very special chemistry [*von Glasow*, 2010]. SO_2 loss rates depend on both atmospheric and plume conditions, and lifetimes have been found to range from a few minutes to several weeks [*Oppenheimer et al.,* 1998, and references therein]. More recently, *Krotkov et al.* [2010] derived a lower limit of 8–9 days for the SO_2 lifetime inside the 2008 Kasatochi plume from SO_2 burdens obtained from measurements by the Ozone Monitoring Instrument (OMI), and *Beirle et al.* [2014] derived an effective SO_2 lifetime of 1–2 days from SO_2 column densities observed by the Global Ozone Monitoring Experiment-2 (GOME-2) in evolving plumes from the Kilauea volcano. *Oppenheimer et al.* [1998] pointed out that the SO_2 conversion to aerosol can be particularly fast inside convective eruption columns, which can have a direct impact on the amount of sulfur reaching the stratosphere. These results also suggest that space-based measurements of SO_2 by the Total Ozone Mapping Spectrometer (TOMS) and other instruments could potentially underestimate the total sulfur injection into the stratosphere following a major eruption as this fast conversion of SO_2 to aerosol does not necessarily imply that the sulfur is lost and does not reach the stratosphere.

Sheng et al. [2015], using kinetic and photochemical rate parameters from *Sander et al.* [2011], reported that OCS is primarily converted to SO_2 through photodissociation (about 80%) in the stratosphere, and reactions with O and OH account for 17% and 3% of that conversion. OCS photodissociation occurs exclusively in the UV, and the photolysis rate increases with altitude [*Chin and Davis*, 1995]. The largest fraction of OCS is converted in the tropics above 25 km altitude, where *Höpfner et al.* [2013] find a maximum in SO_2 that they ascribe to production from OCS photolysis.

Above 35 km, H_2SO_4 photolysis produces SO_2. The rate of this photochemical reaction has long been underestimated. At the beginning UV photolysis was postulated as source for SO_2 in the upper stratosphere and mesosphere [*Rinsland et al.,* 1995; *Mills et al.,* 1999] but subsequently ruled out by studies reporting

insufficient UV absorption cross sections [*Burkholder et al.,* 2000; *Hintze et al.,* 2003; *Robinson et al.,* 2003]. *Vaida et al.* [2003] postulated that the excitation of vibrational overtones by visible and near-infrared light leads to photolysis of H_2SO_4, producing sulfur trioxide (SO_3) and H_2O. The estimated photolysis rates were sufficient to explain the observed SO_2 concentrations above the aerosol layer [*Mills et al.,* 2005a, 2005b]. Those photolysis rates were updated by *Feierabend et al.* [2006] using new cross sections, and by *Miller et al.* [2007] using an altitude-dependent quantum yield. More recently, *Lane and Kjaergaard* [2008] reinvestigated the photodissociation of H_2SO_4 including the absorption of Lyman α photons. Absorption in the Lyman α region seems to be important above 70 km, while at lower altitudes H_2SO_4 photolysis is likely to proceed via the absorption of visible light. UV absorption is unlikely to play a significant role [*Lane and Kjaergaard*, 2008].

2.3. Aerosol Microphysical Processes

There are several aerosol microphysical processes that govern the total aerosol number concentration and size distribution. These processes also influence the lifetime and composition of atmospheric aerosols. For the stratosphere, the large number of processes can be reduced to five major processes: nucleation, coagulation, condensation, evaporation, and sedimentation. As a detailed description of these processes can be found in, for example, *Seinfeld and Pandis* [2006], only a brief description is provided below.

2.3.1. Nucleation

The H_2SO_4 vapor partial pressure in the stratosphere is generally supersaturated, and as a result gaseous H_2SO_4 quickly condenses. Water vapor is always relatively abundant; and therefore, co-condensation of H_2SO_4 and water is the preferred process [*Hamill et al.,* 1990; *Curtius et al.,* 2005] generally forming new aerosols via binary homogeneous nucleation, which is well established in the literature [e.g., *Vehkamäki et al.,* 2002]. Low temperatures, low particle surface areas, and high relative humidities are ideal conditions for binary homogeneous nucleation. Moreover, the onset of gas to liquid heterogeneous nucleation may occur at much lower saturation ratios in the presence of condensation nuclei such as ions or meteoritic smoke particles [*Merikanto et al.,* 2007]. The impact of nonsulfate materials on the formation of stratospheric aerosol on a global scale is not well understood to date. The main nucleation regions for stratospheric aerosol are the TTL [*Brock et al.,* 1995], in particular the lower TTL [*Weigel et al.,* 2011] and the polar middle stratosphere [*Campbell et al.,* 2014].

2.3.2. Coagulation and Condensation

Once new aerosols are formed, they can then further grow through coagulation and condensation. Coagulation is the process of aerosols at various sizes and composition colliding with each other and combining into a single larger particle. Coagulation is therefore mainly dependent on aerosol number concentration. The uptake of water and H_2SO_4 (condensational growth) is mainly controlled by the H_2SO_4 uptake and thereby H_2SO_4 concentrations and, thus, by the thermodynamic properties of H_2SO_4 and ambient temperatures. While nucleation of new particles and coagulation occur over a short time period [*Deshler*, 2008] and at high number concentrations, condensational growth (and evaporation) can occur during most of the stratospheric aerosol lifetime. Growth of larger particles is much slower, and the coagulation rate of larger particles is reduced because of their slower random motion [*Jacob*, 1999]. The growth rate of freshly nucleated particles in the stratosphere is not captured well by measurements. A comparison of model simulations with airborne aerosol measurements suggests growth rates on the order of 0.1 nm h^{-1} [*Lee et al.,* 2011] similar to those found in the polar atmospheric boundary layer [*Kulmala et al.,* 2004]. Furthermore, in situ measurements of organic particulate matter [*Friberg et al.,* 2014; *Murphy et al.,* 2014] suggest that at least in the lower stratosphere organics play a role in particle growth. Model simulations by *English et al.* [2011] suggest that coagulation, and not nucleation, controls the number concentration of particles with a radius larger than 10 nm. Their results also indicate that the effect of Van der Waals forces on coagulation needs to be included in coagulation schemes to realistically simulate the aerosol concentrations in the upper troposphere/lower stratosphere (UTLS), a region of the atmosphere that can be broadly defined as the region ±5 km around the tropopause [*Gettelman et al.,* 2011].

2.3.3. Evaporation and Sedimentation

The stratospheric aerosol spatial distribution in the form of a distinct aerosol layer is partly due to the microphysical processes of evaporation and sedimentation (gravitational settling). In the stratosphere, evaporation repartitions sulfur between the particulate and the gas phase, whereas sedimentation irreversibly redistributes sulfur downward and, to some degree, leads to its transport and therefore loss to the troposphere.

For instance, aerosols in the tropical stratosphere are transported upward by the BDC (section 2.1). Within this uplift, there is size segregation as larger aerosols with appreciable terminal velocities (proportional to the radius squared) move upward either more slowly or downward if they are sufficiently large. Thus, stratospheric aerosols are typically small particles with a radius below 0.2 μm during periods that are unaffected by volcanic eruptions [*SPARC*, 2006]. If the aerosol moves into a warmer environment, such as above approximately 32–35 km altitude, the aerosol evaporates. As a result, virtually all sulfur resides in the gas phase in this altitude region and aerosol concentrations decrease rapidly close to this altitude. Therefore, ground-based and satellite-based lidar measurements often base their calibrations on this relatively aerosol-free region [*Vernier et al.,* 2009]. The new gas phase sulfur is eventually transported to high latitudes where, in the downward branch of BDC, it encounters lower temperatures favorable for recondensation to sulfate aerosols. The large-scale transport and isentropic mixing of aerosols together with nucleation/condensation and sedimentation result in a quasi-steady relative maximum in particle number concentration at around 20 km (Junge layer), depending on latitude [*Deshler*, 2008].

Aerosol in the vicinity of the tropopause can be transported into the troposphere by a variety of mechanisms including directly by sedimentation of large aerosol. Sedimentation is a particularly important stratospheric loss mechanism in the aftermath of a major eruption like Pinatubo and a critical element of the vertical distribution of sulfur throughout the stratosphere. As a result, it is vitally important that chemistry-climate models (section 6) accurately model the size and growth processes of aerosol and account for nonconservative transport of aerosol to reproduce the observed distributions of aerosol and sulfur throughout the stratosphere.

3. Sources of Stratospheric Aerosols

Stratospheric aerosol originates from the input of aerosol and precursor gases into the stratosphere (Figure 1). The aerosol layer is maintained by precursor gases such as OCS [*Crutzen*, 1976] and nonvolcanic SO_2 as well as tropospheric sulfate particles [*Brock et al.,* 1995] that enter the stratosphere predominantly by vertical transport through the TTL [*Fueglistaler et al.,* 2009]. During ascent of air masses through the TTL a large fraction of aerosol and soluble precursors is expected to be removed from the air through uptake by ice particles and subsequent sedimentation. In contrast, insoluble sulfur containing gases such as OCS may reach the stratosphere with little loss (section 2.1). The total transport of sulfur is sensitive to the residence time in the TTL, the detrainment level, and the dehydration and washout efficiency [*Sinnhuber and Folkins*, 2006; *Aschmann et al.,* 2011; *Dinh and Fueglistaler*, 2014]. The total net mass flux from the troposphere to the stratosphere of material that is eventually transformed into aerosol during volcanically quiescent periods was reported to be 820 t/d [*SPARC*, 2006]. It is not clear, however, if the nominal mass flux reported in *SPARC* [2006] is intended to include primary aerosol, but the magnitude suggests that it is for gas precursors only. However, the total net mass flux obtained from the stratospheric sulfur budget shown in Figure 6.12 in *SPARC* [2006] is somewhat smaller with 718 t aerosol/d which converts to a net flux of 64.2 Gg S/yr of sulfur containing compounds across the tropopause (with 1 t aerosol/d = 0.0894 Gg S/yr assuming aerosol is 75% by mass of H_2SO_4). Including primary aerosol transport given in Figure 6.12 increases the flux to about 1450 t aerosol/d. Recently, using the coupled aerosol Solar Climate Ozone Links chemistry-climate model (SOCOL-AER), *Sheng et al.* [2015] have inferred that the total net mass flux of sulfur containing compounds that get transformed into aerosol is about 103 Gg S/yr, corresponding to a flux of 1152 t aerosol/d; the contribution of the different sulfur containing compounds to the overall flux is shown in Figure 1. This estimated total mass flux is about 1.5 times the amount given in *SPARC* [2006]. The total net mass flux changes to 181 Gg S/yr, corresponding to about 2024 t aerosol/d, if primary aerosol is included [*Sheng et al.,* 2015]. As a result, the currently best available estimates of the net sulfur flux from the troposphere into the stratosphere are significantly larger than those reported in *SPARC* [2006] but are based on one model study only.

Major volcanic eruptions may directly inject SO_2 (section 3.1.1) and ash (section 3.2.1) into the stratosphere, leading to enhanced aerosol concentrations lasting up to several years. Because of this strong influence it is quite common to separate between volcanically influenced and volcanic quiescent periods when investigating the impact of stratospheric aerosol on chemistry and climate. The impact of volcanic eruptions on stratospheric aerosol and their contribution to stratospheric sulfur depends on the explosiveness of volcanic eruptions as well as the geographical location of the eruption (section 3.1.1). *Newhall and Self* [1982]

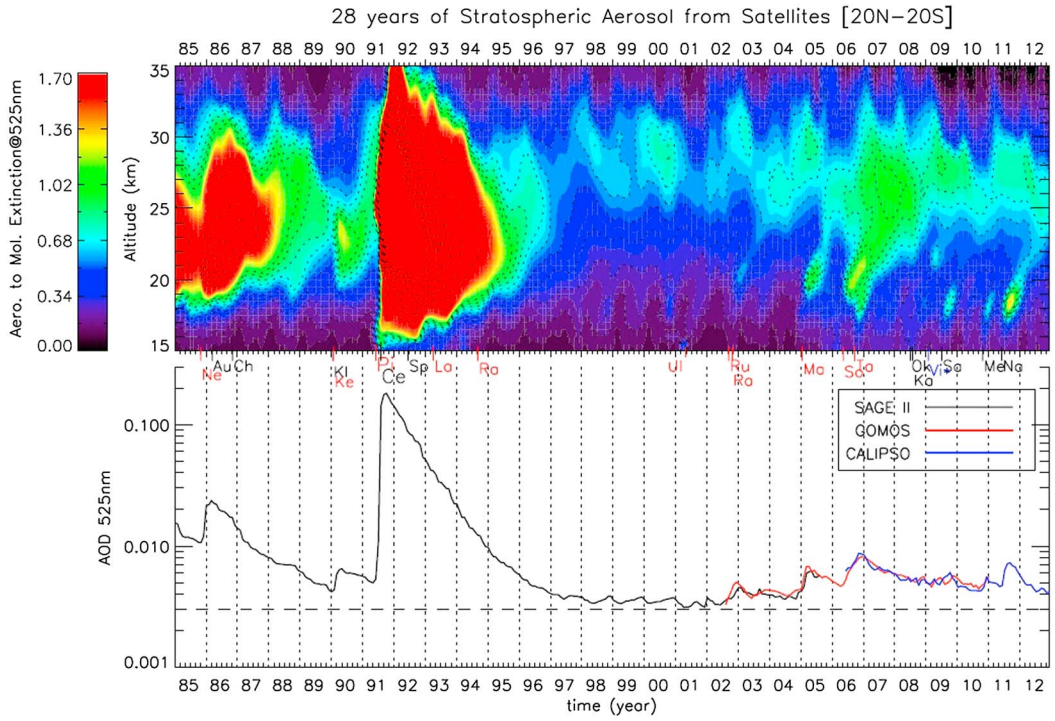

Figure 4. (top) Monthly mean aerosol-to-molecular extinction ratio profile at 525 nm in the tropics (20°N to 20°S) from January 1985 through to December 2012 as derived from SAGE II extinction in 1985–2005 and CALIPSO backscatter between 2006 and 2012. The effect of clouds below 18 km is removed based on their wavelength dependence (SAGE II) and depolarization properties (CALIPSO) compared to aerosols. Extinction ratios from CALIPSO measurements were derived as described in *Vernier et al.* [2011b]. Black contours represent the extinction ratio in log scale from 0.1 to 100. The times of notable volcanic eruptions occurring during the period are denoted by their first two letters on the horizontal axis, where tropical eruptions are noted in red. The eruptions are Nevado del Ruiz (Ne), Augustine (Au), Chikurachki (Ch), Kliuchevskoi (Kl), Kelut (Ke), Pinatubo (Pi), Cerro Hudson (Ce), Spur (Sp), Lascar (La), Rabaul (Ra), Ulawun (Ul), Ruang (Ru), Reventador (Re), Manam (Ma), Soufrière Hills (So), Tavurvur (Ta), Okmok (Ok), Kasatochi (Ka), Sarychev (Sa), Merapi (Me), and Nabro (Na). Vi* denotes the time of the Victoria forest fires with stratospheric aerosol injection. (bottom) Mean stratospheric aerosol optical depth (AOD) in the tropics (20°N to 20°S) between the tropopause and 40 km since 1985 from the SAGE II (black line), GOMOS (red line), and CALIPSO (blue line). This figure is an update of Figures 1 and 5 originally appearing in *Vernier et al.* [2011b].

proposed an index mostly based on the volume of pulverized rock (tephra) emitted during an eruption, which is also correlated with the maximum column height, i.e., the magnitude of the eruption. To date, the volcanic explosivity index (VEI) is used by volcanologists, atmospheric physicists, and climate scientists to describe the size of a volcanic eruption, i.e., the VEI is a relative measure of the explosiveness of volcanic eruptions. This section reviews first the contribution of different sulfur-containing gases to the stratospheric aerosol layer and then the role of nonsulfate compounds.

3.1. Contributions From Sulfur Containing Compounds

3.1.1. Volcanic Eruptions as a Source of Stratospheric Sulfur

In general, emissions from volcanic eruptions consist of ash, SO_2, and other volcanic gases such as water vapor, carbon dioxide (CO_2), hydrogen chloride (HCl), and hydrogen sulfide (H_2S) in highly variable combinations. Some components such as HCl are effectively removed by rainout within the troposphere; others, like ash, have limited climate impact due to their low residence times in the stratosphere (section 3.2.1). Most importantly, even though highly variable, explosive volcanic eruptions are the key source of SO_2 to the stratosphere. In past decades, volcanic injections of SO_2 into the stratosphere like those by El Chichón (1982) and Pinatubo (1991) have dominated stratospheric aerosol and sulfur levels over many years; for example, Pinatubo injected about 18 to 19 Tg of SO_2 as inferred from TOMS and TIROS (Television Infrared Observation Satellite) Observational Vertical Sounder (TOVS) measurements [*Guo et al.,* 2004a]. The Pinatubo eruption led to a peak global aerosol mass loading between 19 and 30 Tg as estimated from

Table 1. Estimated Atmospheric SO_2 Emissions to the UTLS From Volcanic Eruptions in the Last 10 Years[a]

Volcano	Date	Latitude/Height	SO_2 (Tg)	Reference
Kasatochi	Aug 2008	52°N 6–20 km	1.2 to 2.2	*Prata et al.* [2010] *Kristiansen et al.* [2010] *Krotkov et al.* [2010]
Sarychev Peak	Jun 2009	48°N 10–15 km	1.0 to 1.5	*Haywood et al.* [2010] *Carn and Lopez* [2011]
Nabro	Jun 2011	13°N 15–20 km	1.0 to 1.5	*Clarisse et al.* [2014] *Carboni et al.* [2016]
Manam	Jan 2005	4°S 21–24 km	0.3 to 0.6	*McCormick et al.* [2012]
Merapi	Nov 2011	8°S 12–17 km	0.3 to 0.5	*Surono et al.* [2012]
Grimsvotn	May 2011	64°N 10–20 km	0.3 to 0.4	*Sigmarsson et al.* [2013]
Soufriere Hills	May 2006	17°N 15–22 km	0.2 to 0.5	*Prata et al.* [2007] *Carn and Prata* [2010]
Redoubt	Mar 2009	60°N 10–19 km	0.2 to 0.5	*Lopez et al.* [2013]
Calbuco	Apr 2015	42°S 15–21 km	0.2 to 0.5	*Carn et al.* [2016]
Copahue	Dec 2012	38°S 5–20 km	0.2 to 0.5	*Carn et al.* [2016]
Okmok	Jul 2008	53°N 12–16 km	0.2 to 0.4	*Prata et al.* [2010] and *Thomas et al.* [2011]
Rabaul	Oct 2006	4°S 15–20 km	0.2 to 0.3	*McCormick et al.* [2013]
Puyehue-Cordon Caulle	Jun 2011	41°S 12–18 km	0.1 to 0.4	*Carn et al.* [2016]
Kelut	Feb 2014	8°S 16–22 km	0.1 to 0.3	*Carn et al.* [2016]
Jebel-at-Tair[b]	Sep 2007	15°N 9–17 km	0.05 to 0.08	*Eckhardt et al.* [2008] *Clarisse et al.* [2008]

[a]The emissions are based on satellite data, and only the events that had a large impact on the aerosol concentrations in the upper troposphere/lower stratosphere are listed. *Carn et al.* [2016] provide a review of the data and methods used to determine the mass loadings. Relevant references for all eruptions are given in the last column. The volcanic eruptions are sorted by their estimated atmospheric SO_2 emissions, starting with the largest amounts.
[b]There are several other eruptions detected with similar mass emissions as Jebel-at-Tair. Jebel-at-Tair is included as representative because of its high injection height and emissions underwent significant atmospheric transport.

space-based measurements [*McCormick and Veiga*, 1992; *Lambert et al.,* 1993; *Baran and Foot*, 1994]. Based on these estimates, *Dhomse et al.* [2014] estimated a peak aerosol loading between 3.7 and 6.7 Tg of sulfur. Since background estimates of stratospheric aerosol loading are 115–130 Gg of sulfur [*Sheng et al.,* 2015], the peak estimates from Pinatubo are 30 to 60 times higher than background levels. Recent modeling studies support lower stratospheric sulfur levels than those inferred from the TOMS and TOVS observations [*Dhomse et al.,* 2014; *Mills et al.,* 2016]. The difference between the initial and the persistent sulfur levels is important and generally supports a more complex development process following a major eruption than has been considered in the past. These major volcanic eruptions are relatively rare, and no comparable event has occurred since 1991. However, both historic and recent trends in stratospheric aerosol can be largely attributed to volcanic eruptions [*Deshler et al.,* 2003; *Vernier et al.,* 2011b]. After the 1991 Pinatubo eruption, the decade 1992–2000 was characterized by a notable absence of large volcanic eruptions reaching the UTLS (Figure 4). With an *e*-folding time of about 1 year for sulfate aerosol [*Robock*, 2000], stratospheric aerosol levels reached pre-Pinatubo levels by 1998. The 1999–2002 period represents the lowest stratospheric aerosol levels observed since measurements began in the 1970s [*Deshler et al.,* 2006] (Figure 4). In the 2000 to 2012 period, a series of medium sized eruptions in the tropics [*Vernier et al.,* 2011b] are suggested as the cause of the observed aerosol increase, although other possibilities have been suggested (section 5).

The annual flux of SO_2 to the UTLS from volcanic eruptions varies greatly from year to year, from $<$0.1 Tg to 24 Tg of SO_2 emitted by volcanoes in the past 30 years. *Carn et al.* [2016] estimated an average annual flux of

SO_2 from explosive volcanic eruptions of about 1.6 Tg to the UTLS, of which about 1 Tg enters the stratosphere. Table 1 lists a compilation of volcanic eruptions reaching the UTLS as observed by satellite instruments over the last 10 years (with SO_2 emissions ranging from 0.05 to 2 Tg). These volcanic eruptions potentially have a small but measureable impact on stratospheric aerosol levels as they inject aerosol and sulfur to near the tropopause [*Carboni et al.*, 2016]. The tropopause acts as barrier for rapid ascent but allows slow ascent into the stratosphere via dynamical processes (section 2.1). In a long-term sense, since the TTL is the main entrance region for tropospheric air into the stratosphere (section 2.1), tropical volcanic eruptions dominate as a source of stratospheric SO_2, but higher-latitude eruptions occasionally produce noteworthy hemispheric impacts. While the majority of the SO_2 flux from volcanic eruptions to the stratosphere is due to explosive volcanic eruptions, emissions from effusive eruptions can also reach the UTLS [*Carn et al.,* 2016].

3.1.2. Carbonyl Sulfide

OCS is the longest-lived and most abundant reduced sulfur gas in the atmosphere. *Crutzen* [1976] was first to suggest that upward OCS transport maintains the stratospheric aerosol layer in times of volcanic quiescence, and recent model studies support this finding [*Brühl et al.,* 2012; *Sheng et al.,* 2015]. The OCS flux to the stratosphere is typically determined as a fraction of the total mass flux across the tropopause and relies on a prescribed and constant tropospheric OCS mixing ratio. While this is not an unreasonable assumption, a more exact estimate of the OCS flux should account for the regional, seasonal, and long-term variability in tropospheric OCS. Furthermore, a more complete understanding of the tropospheric OCS budget is necessary to predict what might occur as a response to future changes in climate.

3.1.2.1. OCS Observations, Variability, and Trends

Since the *SPARC* [2006] report, the observational record has been significantly expanded. Reanalyzing infrared solar spectra from Jungfraujoch, *Rinsland et al.* [2008] have extended the modern instrumental OCS record back to 1951. Tropospheric and stratospheric column amounts and, to some extent, vertical profiles of OCS are retrieved from high-resolution spectra operationally recorded by Fourier transform infrared spectrometers (FTIR) at several Network for the Detection of Atmospheric Composition Change (NDACC) (http://www.ndacc.org) sites. In situ measurements of OCS mixing ratios are carried out by flask sampling, gas chromatography, and, more recently, ultrasensitive infrared spectroscopy [*Stimler et al.,* 2010b]. Besides regular surface observations at an increasing number of sites in both hemispheres [*Montzka et al.,* 2007], vertical profiles have been measured in situ during regular aircraft flights over the continental United States throughout an entire year [*Montzka et al.,* 2007] and during balloon flights in the tropics and northern high latitudes [*Krysztofiak et al.,* 2015]. At the time the *SPARC* [2006] report was written, the only available spaceborne OCS observations had been made during the Atmospheric Laboratory for Applications and Science (ATLAS) shuttle missions in 1985, 1992, 1993, and 1994 [*Kaye and Miller*, 1996] using the ATMOS (Atmospheric Trace Molecule Spectroscopy Experiment) instrument. Since then *Barkley et al.* [2008] presented global upper tropospheric and stratospheric OCS concentrations derived from spectra measured by the Atmospheric Chemistry Experiment-Fourier Transform Spectrometer (ACE-FTS). This data set represents the first continuous satellite record of OCS, starting in 2004. The ACE-FTS instrument is still active to date. One limitation of ACE is the strong dependence of the latitudinal coverage on season that is inherent in the solar occultation viewing geometry (cf. section 4.3). Two new satellite data sets from the tropospheric emission spectrometer (TES) [*Kuai et al.,* 2014] and the Michelson Interferometer for Passive Atmospheric Sounding (MIPAS) [*Glatthor et al.*, 2015] are expected to complement the ACE-FTS record and provide a complete global coverage of OCS.

The ACE-FTS observations show OCS mixing ratios $>$400 ppt (parts per trillion) right above the tropical tropopause and a rapid decrease with altitude and latitude [*Barkley et al.,* 2008]. *Barkley et al.* [2008] also noted elevated OCS concentrations in the UTLS at low southern latitudes, confirming earlier observations from the shuttle missions and a ship-based FTIR campaign [*Notholt et al.,* 2003]. Both studies suggest that the enhancement is largely driven by OCS emissions from biomass burning.

The results presented in the *SPARC* [2006] report suggested a significant seasonality of OCS concentrations in both hemispheres based on observations across the globe, with lowest concentrations in the Northern Hemisphere in late summer (September) and in the Southern Hemisphere in winter (July), driven by terrestrial vegetation uptake and ocean fluxes, respectively [*Kettle et al.,* 2002a]. The seasonality and understanding

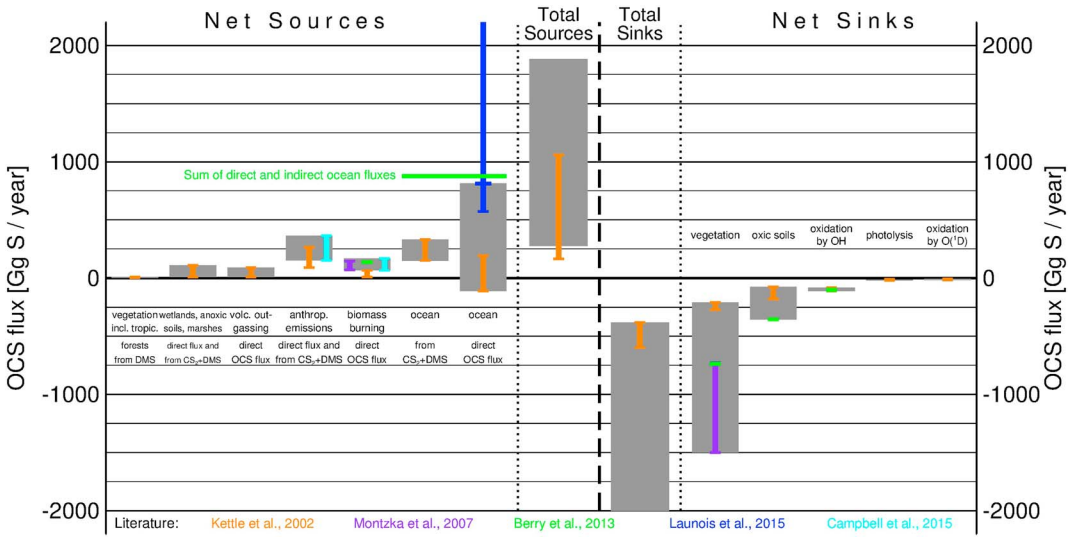

Figure 5. Tropospheric OCS budget as represented in the current literature. The grey bars show the realistic ranges for the different source and sink terms as well as the total sources and sinks. Also included are individual source and sink estimates by *Kettle et al.* [2002a] (orange), *Montzka et al.* [2007] (purple), *Berry et al.* [2013] (green), *Launois et al.* [2015] (blue), and *Campbell et al.* [2015] (cyan). The OCS sink terms due to chemical reactions go back to the study by *Chin and Davis* [1993] and comprise both tropospheric and stratospheric losses. Later, the same authors estimated the total stratospheric OCS loss to 30 Gg S/yr with a 71% contribution from photolysis, 22% from reaction with $O(^1D)$, and 7% from reaction with OH [*Chin and Davis*, 1995]. This increases the chemical loss terms slightly, in particular for photolysis.

of the driving processes were corroborated by *Montzka et al.* [2007] and *Xu et al.* [2001] as well as by mean OCS vertical profiles obtained from the Intercontinental Chemical Transport Experiment-North America during July and August 2004 revealing a considerable OCS drawdown in the boundary layer due to plant uptake during the growing season [*Campbell et al.,* 2008].

Based on earlier studies of Antarctic ice core enclosures and firn air, *SPARC* [2006] reported a rise in atmospheric OCS levels from preindustrial 330–370 ppt to presently around 500 ppt, which is supported by more recent studies [*Aydin et al.,* 2008, 2014]. The long-term rise in OCS mixing ratios correlates with historic anthropogenic emission inventories estimated by *Campbell et al.* [2015]. However, the trend cannot be fully explained by the emission increase, leading *Campbell et al.* [2015] to speculate on a significant contribution due to a historical decline in plant uptake of OCS.

For the modern measurement era, *SPARC* [2006] suggested a small negative trend of 0.5–1.0%/yr from the late 1970s to the mid-2000s for tropospheric OCS based on the instrumental atmospheric data record available at the time. This has not been confirmed by more recent studies that either find no statistically significant temporal trend in atmospheric OCS [*Montzka et al.,* 2007; *Rinsland et al.,* 2008; *Coffey and Hannigan*, 2010] or even a nonmonotonic buildup of OCS since about 2001 of up to 1%/yr at ground-based FTIR stations in the Southern Hemisphere [*Kremser et al.,* 2015].

3.1.2.2. Tropospheric OCS Budget

The global OCS trend has direct implications on the OCS budget. Taking 1%/yr as an upper limit for a statistical trend in either direction limits the source/sink imbalance to about ± 50 Gg/yr. This number is well within the uncertainty margins of the spatially and seasonally gridded inventory of OCS sources and sinks presented by *Kettle et al.* [2002a]. Several recent studies have suggested modifications of individual source and sink strengths compared to *Kettle et al.* [2002a], and an updated budget is shown in Figure 5. Large uncertainties in several individual source and sink estimates and consequently in the overall budget remain, making it a challenge to determine from the sources and sink inventories alone whether the budget is currently closed or not.

An upward revision of the vegetation sink has been suggested based on plant chamber experiments [*Sandoval-Soto et al.,* 2005; *Stimler et al.,* 2010a] as well as on studies analyzing the spatiotemporal variability in atmospheric observations [*Montzka et al.,* 2007; *Campbell et al.,* 2008; *Suntharalingam et al.,* 2008]. *Montzka*

et al. [2007] showed that the seasonal variability and vertical gradients at 10 Northern Hemispheric measurement sites are largely driven by vegetation uptake. This is estimated to be larger by about a factor of 6 compared to the uptake estimated by the traditional method of scaling OCS uptake to net primary production. It was also pointed out in *Montzka et al.* [2007] that the somewhat shifted seasonality of OCS compared to CO_2 suggests an additional response to influences other than net primary production. This might be related to soil uptake, which has also been suggested to be higher than previously thought in a chamber experiment study by *van Diest and Kesselmeier* [2008]. An upward revision of the surface sinks by a factor of 2 or even higher compared to *Kettle et al.* [2002a] bears two important implications. One is a reduced tropospheric lifetime of OCS on the order of 2.5 years [*Montzka et al.,* 2007] as opposed to the 5.7 years proposed previously by *Ulshöfer and Andreae* [1997]. The second implication would be a corresponding upward revision of the sources to balance in the global OCS budget. In a three-dimensional inverse atmospheric modeling approach, *Berry et al.* [2013] suggested a large additional ocean source that is predominantly located in the tropics. This is supported by *Launois et al.* [2015] who used an oceanic general circulation and biogeochemistry model to estimate direct marine OCS emissions of 813 Gg S/yr, about 45% of which are emitted in the tropics between 30°N and 30°S. However, sea-air fluxes of OCS measured and modeled by *Kettle et al.* [2001] and *von Hobe et al.* [2003] during several cruises in different regions do not support such a large global flux. Furthermore, an inverse atmospheric modeling approach by *Kettle et al.* [2002b] that uses lower oceanic OCS fluxes than *Berry et al.* [2013] closes the OCS budget within the uncertainties. Thus, a large uncertainty in the direct oceanic OCS flux remains, and its contribution to the global budget (Figure 5) is not well constrained. More measurements in and over oceans, particularly in tropical regions, are needed to resolve this issue. A 40% upward revision of the direct and indirect anthropogenic sources seems warranted by the results of *Campbell et al.* [2015], who have updated emission factors particularly for the rayon industry and, for the first time, presented temporally and spatially resolved inventories as opposed to climatological emission inventories.

3.1.2.3. OCS Flux

Information about cross-tropopause fluxes of sulfur containing species and their contribution to the stratospheric sulfate aerosol burden are usually received from model calculations. *SPARC* [2006] reported a net OCS flux as calculated by the two-dimensional Atmospheric and Environmental Research (AER) model of sulfate aerosol [*Weisenstein et al.,* 1997] of 31.7 Gg S/yr. A similar OCS flux of 36 Gg S/yr was simulated by *Takigawa et al.* [2002] using a three-dimensional atmospheric general circulation model. Both model studies suggested a contribution of OCS to the total flux of gaseous sulfur into the stratosphere of around 50%, although *Takigawa et al.* [2002] did not consider other precursor gases than OCS and SO_2. *Brühl et al.* [2012] evaluated the OCS flux using a more comprehensive atmospheric chemistry general circulation model. Based on the mass flux across the 100 hPa level within the tropics and the OCS mixing ratio, they calculated a total OCS flux of 150 Gg S/yr. However, their net flux, i.e., the amount of stratospheric OCS converted to aerosol, is 35 Gg S/yr, which is in agreement with the earlier studies. Using the aerosol model AER coupled to a three-dimensional chemistry-climate model, SOCOL-AER, *Sheng et al.* [2015] estimated a net OCS flux across the tropopause of 40.7 Gg S/yr, corresponding to 23% of the total (= gaseous and aerosol) sulfur flux. This calculated flux is about 30% larger than the estimate by the two-dimensional model [*SPARC*, 2006]. Interestingly, the net flux amounts to only about 10% of the one-way flux, indicating that a large fraction of OCS is transported back to the troposphere without being converted to sulfate aerosol. Nevertheless, a substantial fraction of the stratospheric aerosol burden, namely, between 56% [*Sheng et al.,* 2015] and 70% [*Brühl et al.,* 2012], is expected to originate from OCS. Missing surface emissions of short-lived sulfur species or an underestimated transport of primary aerosol and/or SO_2 into the stratosphere were discussed as potential reasons for the model spread [*Sheng et al.,* 2015]. The model results are supported by observation-based net OCS flux estimates of 34–66 Gg S/yr and 49 ± 14 Gg S/yr by *Barkley et al.* [2008] and *Krysztofiak et al.* [2015], respectively.

3.1.3. Short-Lived Compounds

Significant amounts of sulfur are released from various surface sources in the form of carbon disulfide (CS_2), dimethyl sulfide (DMS), and hydrogen sulfide (H_2S). None are directly transported to the stratosphere in any substantial amounts, because all three compounds readily react with OH, resulting in lifetimes on the order of hours. Deep tropical convection systems, however, might provide a pathway for short-lived gases to reach the TTL. *Marandino et al.* [2013] presented ship measurements of DMS made during a cruise through the tropical western Pacific. These DMS measurements were used in a Lagrangian transport model to investigate the amount of DMS that is transported into the TTL. Their results suggest that up to 30 g S/month, emitted from an area of 5.75×10^4 m^2, in the form of DMS can reach altitudes above 17 km through intense vertical transport

where it can potentially be transported further into the stratosphere, providing a source of stratospheric aerosol. However, further measurements of DMS seawater concentrations in the tropical western Pacific are required to quantify the potential contribution of DMS to stratospheric aerosol.

Short-lived precursors make a significant contribution to the tropospheric budget of SO_2, which is the main oxidation product of the OH reaction for all three gases (section 2.2 and Figure 1). More importantly, the OH reactions of DMS and CS_2 represent significant tropospheric sources for the long-lived OCS (section 2.2), which are included in the OCS budget estimate presented in Figure 5. The conversion efficiency for CS_2 to OCS has been measured to be 0.83 ± 0.08 in the laboratory by *Stickel et al.* [1993] and has not been updated since. The CS_2 budget has been reasonably well constrained [*Watts*, 2000]. An upward revision of the anthropogenic CS_2 emissions has recently been made by *Campbell et al.* [2015] (section 3.1.2.1). The fraction of DMS that is converted to OCS is lower; a value of $0.7 \pm 0.2\%$ that was reported by *Barnes et al.* [1994] and supported by a more recent study by *Albu et al.* [2008] is commonly used to derive the OCS source strength from DMS. The global distribution and magnitude of DMS sources still bear substantial uncertainties, in particular with respect to oceanic emissions. *Lana et al.* [2011] have updated the database of surface seawater DMS concentrations and emission fluxes by *Kettle et al.* [1999] and *Kettle and Andreae* [2000]. Compared to the previous studies, they find lower concentrations in polar latitudes and higher concentrations in previously undersampled regions such as the southern Indian Ocean. They estimate global oceanic DMS emissions of 28.1 (17.6–34.4) Tg S/yr. *Land et al.* [2014] calculate 19.6 Tg S/yr using the same DMS database [*Lana et al.,* 2011] but 2008/2009 satellite data for wind speed and sea surface temperature as well as a different sea-air flux parameterization. These numbers are within the range of previous estimates [*Kettle and Andreae*, 2000; *Elliott*, 2009], with a large uncertainty still introduced by the parameterization of sea-air fluxes. Model studies suggest a significant climate sensitivity of the marine DMS emissions [*Halloran et al.,* 2010; *Cameron-Smith et al.,* 2011; *Land et al.,* 2014], which may indirectly influence the OCS budget in future climate scenarios.

3.1.4. Sulfur Dioxide

The major influence of volcanic eruptions on stratospheric SO_2 and aerosol has been demonstrated [*Guo et al.,* 2004a; *Vernier et al.,* 2011b], but significant uncertainties concerning the relative importance of the different stratospheric SO_2 sources during volcanically quiescent periods remain [*Solomon et al.,* 2011; *Brühl et al.,* 2012]. In this section the SO_2 observations available for the stratosphere and tropopause region and the resulting SO_2 distribution are reviewed.

3.1.4.1. Observations of SO_2 in the Stratosphere

First remote sensing observations of SO_2 in the stratosphere were reported for volcanically perturbed conditions including Upper Atmosphere Research Satellite-Microwave Limb Sounder (UARS-MLS) and ATMOS measurements of the Mount Pinatubo eruption cloud by *Read et al.* [1993] and *Rinsland et al.* [1995]. Very recently, global altitude-resolved SO_2 distributions were reported from infrared limb emission observations by MIPAS on Envisat for a 10 year period (2002–2012) derived from monthly and zonally averaged MIPAS spectra [*Höpfner et al.,* 2013] and single limb spectra [*Höpfner et al.,* 2015], covering an altitude region of 10–40 km. Figure 6 provides an overview of the MIPAS global time series of SO_2 monthly mean distribution at various altitudes (altitudes between 10 and 20 km) for 10° longitude bins. Most striking are the periods with strong enhancements of the SO_2 volume mixing ratios due to volcanic eruptions. During volcanic quiescence periods SO_2 mixing ratios are, in general, highest in the northern midlatitudes in the lowermost stratosphere ranging between 40 and 100 ppt and decreasing above to an altitude of approximately 25 km. In the midstratosphere (about 25 to 35 km), MIPAS observed a relative maximum in SO_2, which is most pronounced in the tropics with mixing ratios of approximately 50 ppt. This maximum results from the photochemical production of SO_2 from OCS oxidation and is in agreement with climate model simulations [*Brühl et al.,* 2012]. Above 35 km, the SO_2 mixing ratios are slightly increasing toward higher altitudes due to SO_2 formation by photolysis of H_2SO_4. This result is consistent with available balloon-borne in situ H_2SO_4 profile measurements showing a decrease of the H_2SO_4 mixing ratios above about 35 km [*Schlager and Arnold*, 1987]. For volcanically enhanced SO_2 in the stratosphere, MIPAS observations compare reasonably well with available ATMOS and ACE-FTS remote sensing measurements [*Höpfner et al.,* 2013].

In situ measurements of SO_2 up to an altitude of 20.4 km have only been reported by *Inn and Vedder* [1981]. SO_2 mixing ratios analyzed from cryogenic samples taken during flights of the ER-2 research aircraft over

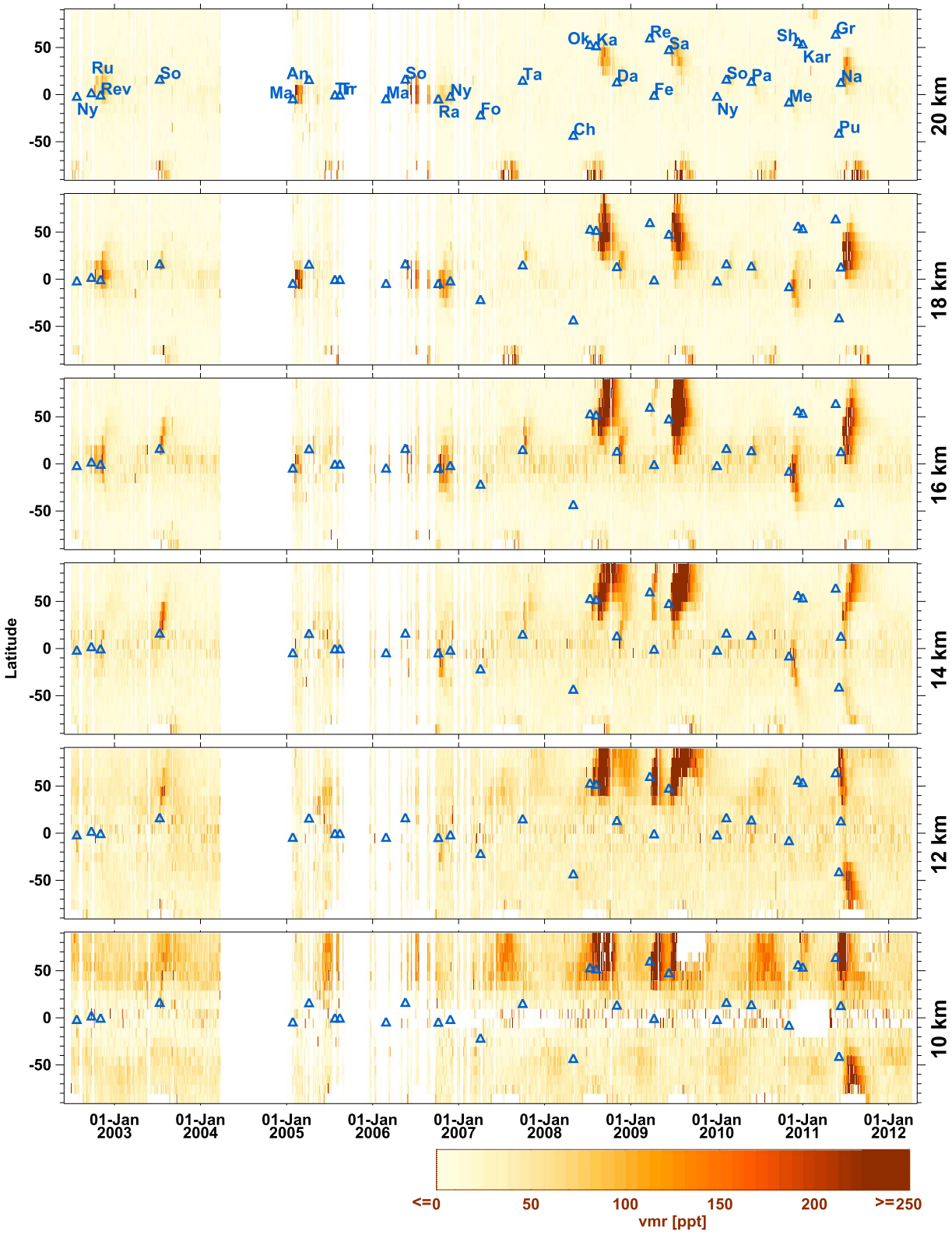

Figure 6. Time series of MIPAS SO_2 distributions with a time resolution of 2 days. SO_2 volume mixing ratios are color coded (values larger than 250 ppt are given the color of 250 ppt). Volcanic eruptions are marked by blue triangles. (Figure is adapted from *Höpfner et al.* [2015]).

California and Alaska range between 36 and 50 ppt at altitudes between 15.2 and 20.3 km. Airborne in situ measurements of SO_2 in the altitude range from 8 to 15 km were summarized for USA campaigns by *Thornton et al.* [1999]. The in situ SO_2 measurements for the European campaigns were compared with MIPAS observations, and reasonable agreement between both data sets was found [*Höpfner et al.,* 2015]. Mean mixing ratios of SO_2 at these altitudes are highly variable and range between 5–800 ppt at northern midlatitudes, 8–120 ppt in the tropics, and 5–20 ppt at southern midlatitudes. The large SO_2 enhancements observed in the vicinity of the tropopause are often connected to an uplift of polluted air masses by warm conveyor belts (see section 3.1.4.2). Additional in situ measurements in the stratosphere at altitudes above 15 km are needed for validation of the remote sensing measurements and to build an enhanced observational basis for model improvement and validation.

3.1.4.2. Elevated SO_2 in Stratospheric Air Influenced by Warm Conveyor Belts

The efficiency of SO_2 vertical transport from the planetary boundary layer of major anthropogenic SO_2 emission regions to the tropopause region and lowermost stratosphere is poorly known, due mainly to poorly known heterogeneous SO_2 loss by cloud processes occurring during uplift such as washout, rainout, and liquid-phase conversion to sulfate. Uplift of SO_2 in the planetary boundary layer may occur by deep convection and so-called warm conveyor belts (WCBs), which are strongly ascending airstreams in extratropical cyclones. The strongest SO_2 source regions related to fossil fuel combustion are located over East Asia, Europe, and eastern North America. The frequency of WCBs occurrence is most pronounced downstream of the major SO_2 emission regions in East Asia and North America [*Eckhardt et al.,* 2004; *Madonna et al.*, 2014]. Air mass uplift by WCBs occurs within 1–2 days. After 2–3 days traveltime in the upper troposphere, about 5% of all air mass trajectories within WCBs enter the stratosphere according to climatology by *Eckhardt et al.* [2004]. While this is a small fraction of tropospheric air within WCBs entering the stratosphere, source regions for some of this air in major anthropogenic SO_2 emission regions or near high-latitude volcanoes allow a possible contribution to stratospheric aerosol.

SO_2-rich pollution plumes in the upper troposphere lifted by East Asian WCBs [*Fiedler et al.,* 2009a, 2009b] and North American WCBs [*Arnold et al.,* 1997] have been detected previously by aircraft measurements. Recently, satellite-borne remote sensing observations of rapid transpacific transport of anthropogenic SO_2 plumes in the upper troposphere originating in East Asia were presented by *Clarisse et al.* [2011] for observations obtained from the Infrared Atmospheric Sounding Interferometer (IASI) and by *Hsu et al.* [2012] for OMI measurements. Furthermore, ^{133}Xe released by the nuclear power plant accident at Fukushima/Daiichi has been used as tracer to unambiguously demonstrate the transport of East Asian planetary boundary layer air to the UTLS in Europe mediated by a West Pacific WCB [*Baumann and Schlager*, 2012], illustrating the wide range of possibilities for the transport of SO_2 to the UTLS in WCBs.

In the lowermost stratosphere, SO_2 will experience near complete conversion to gas phase sulfuric acid via reactions involving OH and water vapor [*Reiner and Arnold*, 1994]. Subsequently, the sulfuric acid will condense on preexisting particles or nucleate to form new particles. The contribution of either of these pathways to the stratospheric sulfate aerosol layer still needs to be quantified and remains an open question.

3.2. Contribution of Nonsulfate Compounds

A large amount of recent research has focused on stratospheric aerosol components other than the dominant H_2SO_4 and H_2O components. Nonsulfate components of stratospheric aerosol include organic aerosols as well as solid refractory aerosols from natural sources, for example, volcanoes (section 3.2.1) and pyrocumulonimbus (section 3.2.3), from meteoric ablation (section 3.2.4), or from anthropogenic origin (e.g., space debris, rocket emissions, and soot from fossil fuel burning). Refractory aerosol implies nonvolatile or temperature stable atmospheric particles—for a refractory aerosol, or parts of it, to evaporate the aerosol needs to be exposed to temperature $>> 500^{\circ}C$. Nonsulfate aerosols can significantly contribute to the stratospheric aerosol composition, not necessarily by mass, but even traces of these compounds can influence chemical and microphysical processes.

Stratospheric aerosol is more diverse than commonly recognized and not necessarily connected to a single, specific source. For refractory aerosols, there are three known regions in the middle atmosphere where their presence is of particular interest: (i) The upper stratosphere, the mesosphere, and the winter polar regions where the contribution of Meteoric Smoke Particles (MSPs) dominates. For example, a belt of MSPs between 25 and 45 km altitude was observed by satellites following the explosion of the Chelyabinsk bolide in Russia

[*Gorkavyi et al.,* 2013]. Cosmic dust, originating from comets and asteroids [*Plane et al.,* 2015], ablates on atmospheric entry; the resulting metal atoms become oxidized and polymerize into MSPs. Subsidence in the polar vortex leads to fast transport (timescale of weeks to months) of refractory particles from the mesosphere to the lower stratosphere [*Curtius et al.,* 2005; *Weigel et al.,* 2014]. (ii) The lower to middle stratosphere in the equatorial region where refractory aerosols originate in the troposphere, e.g., due to volcanic eruptions (section 3.1.1) or due to combustion processes (sections 3.2.2 and 3.2.3). Aerosol that reaches the tropical lower stratosphere will be vertically lifted by the BDC. This has been demonstrated previously for aerosol from volcanic eruptions [*Vernier et al.,* 2011b]. (iii) The lower stratosphere, a region characterized by a mixture of the materials transported into this region by three main pathways: from above due to the BDC, from below due to troposphere-stratosphere-exchange processes, as well as from equatorward transport out of the polar regions, when the polar vortex breaks down at the end of winter.

Refractory aerosol plays an important role in the stratosphere. They provide surfaces for condensation of sulfuric acid and water forming sulfate aerosol following major volcanic eruptions, therefore limiting new particle formation. Furthermore, refractory aerosol may provide heterogeneous nuclei for the formation of solid phase PSC particles and thereby promoting dehydration and denitrification of the polar stratosphere [*Fahey et al.,* 2001].

Moreover, refractory aerosol such as soot has the potential to change the optical properties of the predominantly liquid stratospheric aerosol. The lower stratosphere between the poles and equator provides a "natural laboratory" for the processing and possible conversion of the nonsulfate material approaching from different source regions. It is likely that almost all refractory species are embedded and potentially dissolved in liquid sulfuric acid aerosol [*Murphy et al.,* 2014]. Solubility, reactivity, and charge-driven mechanisms control the effectiveness of chemical conversion. The physicochemical properties of such impure sulfuric acid aerosol strongly depend on the properties and quantities of the respective solutes.

In the following, the state of knowledge for some specific nonsulfate aerosol types, beyond the discussion given in the *SPARC* [2006] assessment and the review by *Peter and Grooß* [2012], is reviewed.

3.2.1. Volcanic Ash

Volcanic ash is tephra and is characterized by a very broad size distribution (submicrometer to millimeter sized) [*Rose and Durant*, 2009], with highly irregular particle shapes and often complex composition, but with a high percentage of silicon (Si). Glass, crystals, and gas bubbles are often found in volcanic ash sampled during or after ashfall. Direct measurements of ash particles in the atmosphere are very rare. Some airborne sampling has been undertaken during and shortly after a few eruptions, e.g., Mount St Helens [*Hobbs et al.,* 1981], Hekla [*Rose et al.,* 2006], Kasatochi, Sarychev, and Eyjafjallajökull [*Andersson et al.,* 2013], and some Ecuadorian and Colombian volcanic plumes [*Carn et al.,* 2011]. During the satellite era, several imaging and sounding instruments have been used to infer properties of ash clouds [*Prata*, 2009]. *Griessbach et al.* [2014] presented a method to differentiate signatures of ash clouds from other aerosol types in infrared limb spectra, allowing instruments such as Envisat-MIPAS to detect the presence and vertical resolution of ash clouds.

There are virtually no direct measurements of the size distribution in the months immediately following a large volcanic eruption. Satellite instruments have been used successfully to monitor volcanic ash throughout the atmosphere and can provide a crude estimate of the amount of ash emitted to the atmosphere for eruptions with VEI $>$ 2. *Clarisse and Prata* [2015] describe retrieval techniques required to transform infrared satellite measurements of volcanic ash into geophysical parameters, such as optical depth, particle effective radius, mass loading, and total mass. Figure 7 shows estimates of the ash mass emitted to the atmosphere for a few eruptions between 1982 and 2012. Typically, emissions range from about 10 Gg to 1000 Gg. *Guo et al.* [2004b] estimated the fine ash (radii $<$ 63 μm) mass emitted by Pinatubo to be about 50 Tg in June 1991 and about 3 Tg from Cerro Hudson in August 1991. *Schneider et al.* [1999] estimated about 7 Tg from the 1982 eruption of El Chichón. There are no reliable estimates of ash emissions from large eruptions occurring in the presatellite era, but based on VEI and by extrapolation from satellite estimates of more recent eruptions a conservative value of about 500 Tg for Tambora (1815) can be estimated. For the Toba supereruption of about 73,500 years ago, *Rampino and Self* [1992] estimated between 1 and 10 Pg of ash emitted to the atmosphere, much of this must have been stratospheric.

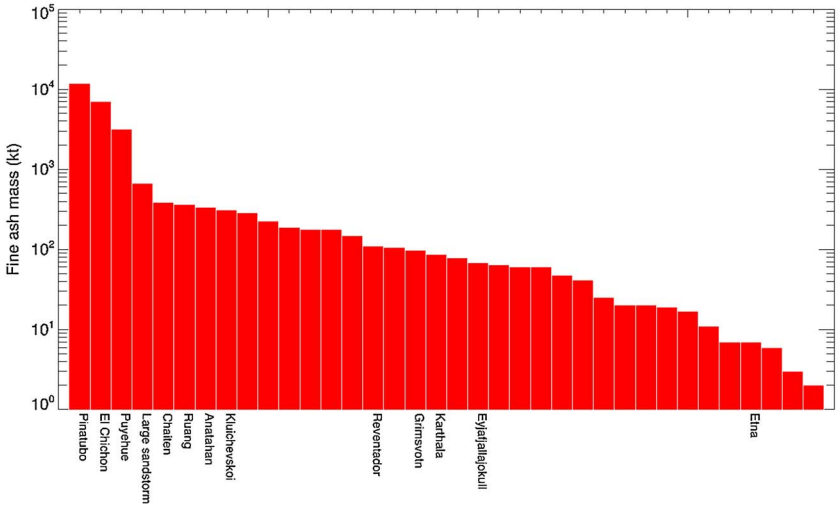

Figure 7. Fine ash mass (radii < 63 μm) from a selected number of eruptions between 1982 and 2012. Estimates are based on satellite retrievals and typically are accurate to approximately 50%. To avoid overloading of this figure, only a few selected volcanic eruptions are named here.

The climate impact of ash, as opposed to sulfate, is not expected to be significant because of the rapid loss of mass due to sedimentation. *Bertrand et al.* [2003] have estimated the radiative impact of ash emissions from the Mount Etna eruptions in 2002. *Bertrand et al.* find the shortwave forcing (SWF = cloudy sky-clear sky forcing at the top of the atmosphere) to be of similar size to that of meteorological clouds having similar opacity, but the longwave forcing is greater than that of meteorological clouds. Furthermore, global aerosol model simulations showed that volcanic fine ash leads to an additional radiative heating during the first days after the eruption [*Niemeier et al.,* 2009]. Dependent on the geographical location of the volcanic eruption, the initial transport direction may change due to the presence of volcanic fine ash as the additional heating causes strong disturbances in the flow pattern, changes wind directions, and increases wind speed.

3.2.2. Black Carbon and Organic Aerosols

Distinct differences between the upper troposphere and lower stratosphere observed in some parameters such as ozone concentrations and temperature gradient, are generally accompanied by more gradual transitions of tropospheric-sourced aerosol concentration across the cold point tropopause, although sharp transitions in aerosol concentrations have been observed in the tropics and subtropics [*Brock et al.,* 1995; *Borrmann et al.,* 2010]. Aerosols originating in the troposphere, including organic carbon (OC, a complex class of materials containing carbon with substantial hydrogen), black carbon (BC, formed by incomplete combustion of fossil fuels, biofuels, and biomass, is the most strongly light absorbing and refractory component of soot), and other species mix through the tropopause and mix with particles of stratospheric origin such as secondary sulfate and meteoric materials [*Blake and Kato*, 1995; *Hudson et al.,* 2004; *Nguyen et al.,* 2008; *Froyd et al.,* 2009]. In the tropics and midlatitudes these tropospheric particles can still account for significant fractions of the aerosol mass 2 km above the cold point tropopause [*Froyd et al.,* 2009].

The tropospheric accumulation-mode particles (0.1–1.0 μm in diameter) in the lower stratosphere come from all possible low-altitude sources, with substantial contributions from OC and BC aerosols from biomass burning (BB). BB contributes about 10% (up to 50%) by number of particles between 0.25 and 2 μm diameter to aerosols in the lower stratosphere in the northern midlatitude [*Hudson et al.,* 2004]. Based on model studies, aircraft emissions make up about 0.5% of the total global fossil fuel emission of BC, with potentially significant contributions to aerosol number and BC mass in the lowermost stratosphere [*Hendricks et al.,* 2004]; these particles can be transported along the BDC [*Schwarz et al.,* 2013]. Recent model studies demonstrate regional influences of tropospheric processes, for example, the Asian tropopause aerosol layer contains sulfate and primary and secondary OC components, while a corresponding North American layer does not contain primary OC [*Yu et al.,* 2015]. In contrast to tropospheric contributions, meteoritic dust contributes only very small amounts of OC to the stratosphere [*Jenniskens et al.,* 2000].

OC and BC, as other stratospheric aerosol, have a long residence time in the stratosphere, but their relative abundance decreases with height above the tropopause due to in situ production of sulfate and the lack of significant in situ production of OC and BC in the lower stratosphere [*Murphy et al.,* 2007]. As a result, OC and BC become increasingly minor components in aerosols above the tropopause in, for example, the midlatitudes [*Schwarz et al.,* 2008]. Below these altitudes aerosols are composed of OC and sulfate in comparable amounts [*Friberg et al.,* 2014], while BC typically contributes only 1% of the total aerosol mass loading in the UTLS [*Schwarz et al.,* 2008]. The mass mixing ratio of BC appears to reach fairly constant values near 1 ng of BC/kg of air in this altitude range [*Murphy et al.,* 2014]. Hence, it is not likely that BC is a strong contributor to either aerosol number or mass in the UTLS.

Although the contributions of OC and BC to optical scattering will approximately scale with their relative contributions to aerosol mass, OC and BC will disproportionately affect optical absorption. BC absorbs efficiently across the visible region, while the OC absorption is spectral, with more efficiency in the blue. BC's absorption causes heating that was on average about 1% but up to 25% of that due to UV absorption by ozone in the TTL [*Gao et al.,* 2008b]. BC in the lower stratosphere also has the potential to nucleate ice formation [*Kärcher et al.,* 2007], with highly uncertain indirect impacts on climate [*Bond et al.,* 2013].

3.2.3. Smoke Particles From Biomass Burning

Biomass burning is an important source of atmospheric aerosols. In its most vigorous form, as pyrocumulonimbus (PyroCb), biomass burning can inject particles directly into the lower stratosphere. PyroCbs are fire-started or fire-augmented thunderstorms [*Fromm et al.,* 2010], where the sensible heat released by the fire starts or enhances deep convection. Due to the increased number of cloud condensation nuclei and the increased vertical updraft velocity within a PyroCb, precipitation in such clouds and, thus, scavenging of smoke particles are suppressed [*Rosenfeld et al.,* 2007]. As a result, a significant fraction of the particles injected at the cloud base can reach the outflow regions at the cloud top. One case study of a PyroCb indicated possible lofting of particles as high as 7 km above the tropopause within the month following the PyroCb [*Fromm et al.,* 2005].

Biomass burning particles consist in varying fractions of organics, soot, and inorganic cores [e.g., *Reid et al.,* 2005]. *Dahlkötter et al.* [2014] estimated that the amount of black carbon injected into the upper troposphere by a single PyroCb can be as large as 126 Mg, which, according to their estimate, is on the same order of magnitude as the daily black carbon emissions by the global aircraft fleet. A North American PyroCb was observed to reach up to 3 km above the tropopause, increasing aerosol extinction by a factor of 4 in the UTLS compared to background conditions [*Damoah et al.,* 2006]. After the Australian "Black Saturday" fire in February 2009, a soot plume was observed by satellites in the lower stratosphere (up to 22 km) for several weeks [*Siddaway and Petelina*, 2011]. However, an analysis by *Pumphrey et al.* [2011] showed that this event was not typical.

The frequency of PyroCbs reaching the stratosphere is not well known. According to a study by *Guan et al.* [2010], analyzing 11 years of satellite measurements, globally, on average, about 17 PyroCbs per year reach altitudes above 8 km, primarily over North America and North-East Asia. A similar order of magnitude was derived by *Gonzi et al.* [2015], who used satellite fire data for 2006 in combination with a plume rise and a chemistry transport model. Based on in situ particle mass spectrometer measurements, *Murphy et al.* [2014], however, excluded pyroconvection as a dominant source of the carbonaceous aerosols in the lower stratosphere. This was supported by *Friberg et al.* [2014], using elemental composition analysis of particles sampled in the lowermost stratosphere.

3.2.4. Meteoric and Extraterrestrial Aerosol Material

The global input rate of cosmic dust particles into the Earth's upper atmosphere is quite uncertain: recent estimates vary by 2 orders of magnitude from about 3 to 300 t/d [*Plane*, 2012]. One reason for this large range is that the mass distribution of the particles (0.1 μg to 1 mg) and their entry velocity distribution (11 to 72 km s^{-1}) are challenging to measure directly [*Plane*, 2012]. Measurements either cover a subset of the mass/velocity distributions or sample only a fraction of the ablation products, e.g., radar observations of meteors [*Mathews et al.,* 2001; *Pifko et al.*, 2013], lidar (light detection and ranging) measurements of the vertical flux of sodium (Na) and iron (Fe) produced by meteoric ablation [*Huang et al.,* 2015], and measurements of the surface accumulation flux of cosmic spherules [*Taylor et al.,* 1998] and MSPs [*Gabrielli et al.,* 2004] in polar snow and ice.

The size range of MSPs in the atmosphere covers clusters of molecules (diameter ≈ 1 nm) up to hundreds of nanometer diameter particles. The evolution of the nucleation mode (diameter < 10 nm) of MSPs was

numerically investigated [*Bardeen et al.,* 2008; *Megner et al.,* 2008]. The size distribution of refractory aerosols in the middle atmosphere is constrained to a diameter between 1 nm and 20 μm because micrometer-sized particles experience relatively fast removal due to sedimentation. *Dhomse et al.* [2013] modeled the atmospheric redistribution of radioactive particles following the reentry of a satellite power unit at an altitude of 46–60 km in 1964: this study showed that submicrometer MSPs take about 4 years to reach the surface.

3.2.4.1. Detection and Chemical Composition of Refractory Aerosols

The abundance of refractory aerosol, most likely of meteoric origin, has been derived from incoherent scatter radar spectra from above 70 km altitude. These observations were confirmed by rocket-borne measurements of charged aerosols at 80–90 km [*Amyx et al.,* 2008; *Friedrich et al.,* 2012; *Rapp et al.,* 2012; *Plane et al.,* 2014]. Satellite observations of MSP optical extinction between 35 and 80 km altitude have also been reported [*Hervig et al.,* 2009]. Airborne in situ measurements at altitudes of up to 21 km [*Curtius et al.,* 2005; *Weigel et al.,* 2014] showed subsidence of nonvolatile aerosol material with about 100 particles per mg air, contributing up to 75% of detected stratospheric particles within the Arctic vortex. In the Antarctic vortex, balloon-borne in situ measurements indicated that the nonvolatile fractions were about 60% above 20 km except in the new particle formation layer between 21 and 24 km altitude were it drops to below 20%. Below and above this layer the nonvolatile particles have mixing ratios of 100–200 per mg air [*Campbell and Deshler*, 2014].

The chemical fingerprint of MSPs was identified by in situ laser ablation mass spectrometry, showing a characteristic magnesium to iron ratio in the midlatitude lowermost stratosphere [*Cziczo et al.,* 2001; *Murphy et al.,* 2014]. The first scanning electron microscopy (SEM) images of particles sampled at 20–37 km altitude go back to the work of *Bigg et al.* [1970]. *Mackinnon et al.* [1982] showed SEM images together with chemical composition analysis of particles collected in the stratosphere, of which a significant fraction was attributable to its extraterrestrial origin. *Della Corte et al.* [2013] sampled 0.4 and 9 μm diameter particles, including calcite-type and adherent pure carbon smoke nanoparticles (diameter 10–70 nm), when flying through the debris cloud of a meteoric fireball.

3.2.4.2. Interactions Between Sulfate and Nonsulfate Stratospheric Aerosol

Laboratory studies and numerical modeling simulations have been performed to investigate the potential of MSPs to provide condensation surfaces for water vapor and to initialize ice cloud formation [*Saunders et al.,* 2010]. *Hervig et al.* [2012] found that mesospheric ice particles in polar mesospheric clouds can contain over 1% by mass of MSPs. *Frankland and Plane* [2015] showed that the subsequent sublimation of the H_2O ice will leave behind a refractory residue. Impactor sampling in the middle and upper stratosphere showed that the collected solid particles act as nucleation cores for sulfate particles [*Bigg*, 2012]. The impact of MSPs on H_2SO_4 and HNO_3 on global scales was studied by *Saunders et al.* [2012] and *Frankland et al.* [2015], using laboratory experiments and global circulation models.

One implication of refractory aerosol in the stratosphere may be its impact on the physicochemical properties of the dominant sulfur aerosol. *Cziczo et al.* [2001] found that in about half of all analyzed stratospheric particles were high concentrations of meteoric iron (0.5–1 wt %). Iron, magnesium, and nickel seem to dissolve readily in concentrated H_2SO_4 [*Saunders et al.,* 2012], leaving silicon-aluminum-oxygen solid residual particles [*Murphy et al.,* 2014]. The dissolution of MSPs in sulfuric acid aerosol is probably a source of negative ions that mitigate the acidity of stratospheric aerosol [*Prather and Rodriguez*, 1988].

Modified acidity could subsequently affect the freezing properties of binary HNO_3-H_2O or ternary HNO_3-H_2SO_4-H_2O solution droplets, which could be important for Polar Stratospheric Clouds (PSC) formation [*Chang et al.,* 1999]. *Wise et al.* [2003] investigated the solubility of iron and magnesium compounds within H_2SO_4, and the possible impact on particle freezing. At certain H_2SO_4 concentrations the solutes of these metals increase the freezing threshold temperature by up to 20 K compared to pure H_2SO_4 solution droplets [*Wise et al.,* 2003].

Although not yet well quantified globally, the atmospheric abundance of MSPs appears to be significant. The upper limit of the estimated global cosmic dust mass flux of up to 300 t/d [*Plane*, 2012] is approximately 15% of the total net stratospheric aerosol mass flux, which consists of nonvolcanic primary aerosol and aerosol precursor gases, estimated by *Sheng et al.* [2015]. Moreover, the concentration of meteoric material is locally very variable. Interactions between MSPs and condensable vapors, i.e., of H_2SO_4, HNO_3, H_2O, are observed in the atmosphere and have been studied in the laboratory. Condensational growth of the refractory cores

increases their sedimentation speed and removal, resulting in a vertical redistribution of aerosols and condensable material from the lower stratosphere toward the surface.

4. Measurements of Stratospheric Aerosol

The earliest inferences concerning particles in the stratosphere, date to the 1920s when systematic twilight observations became available. *Volz* [1975] described twilight measurements gleaned from atmospheric turbidity records following the 1912 Katmai eruption. More direct sampling of stratospheric aerosol began with the pioneering in situ observations of *Junge and Manson* [1961] and *Rosen* [1964]. Shortly after these observations were made, surface-based lidar was developed. Regular observations of stratospheric aerosol with in situ instruments began in 1971 and with lidar in 1974. Balloon-borne optical particle counters provide vertically resolved in situ particle size and number concentration measurements. Lidar measurements provide vertically resolved measurements of atmospheric backscatter from both molecules and aerosol at one or more wavelengths. There are several lidar sites investigating stratospheric aerosol ranging from 90°S to 80°N and an in situ record that has continued to the present [*Deshler*, 2008]. The balloon-borne and lidar measurements were complemented by satellite-based measurements starting in the late 1970s (e.g., Stratospheric Aerosol Measurement, SAM, II and Stratospheric Aerosol and Gas Experiment, SAGE) providing a global coverage of stratospheric aerosol measurements [*Yue et al.,* 1989]. Measurements from passenger and research aircrafts since the late 1980 have provided additional unique information about UTLS aerosol properties. The various observation platforms and the development of new and improved observational tools and techniques of aerosol properties are discussed in detail below, followed by a description of the qualitative and quantitative advancements made since *SPARC* [2006].

4.1. Balloon-Borne and Airborne In Situ Measurements

Three sets of in situ instruments have made up the bulk of stratospheric aerosol size distribution measurements since such measurements began in the late 1950s. These are the University of Wyoming's balloon-borne optical particle counters (WOPCs) and condensation nuclei (CN) counters [*Hofmann et al.,* 1975; *Deshler et al.,* 2003], the University of Denver's airborne focused cavity aerosol spectrometer (FCAS) [*Jonsson et al.,* 1995] and nucleation-mode aerosol size spectrometer (NMASS) [*Brock et al.,* 2000], and the particle counters and particle impactor sampler on board the civil aircraft for regular investigation of the atmosphere based on an instrument container (CARIBIC) [*Hermann and Wiedensohler*, 2001; *Nguyen et al.,* 2006]. In addition, there have been episodic aircraft measurements of CN using an instrument similar to the NMASS from 45°N to 25°S [*Borrmann et al.,* 2010; *Weigel et al.,* 2011]. Once all sampling biases are removed from the measurements, the native quantity from these instruments is an aerosol size distribution. Moments of the size distribution like surface area density (second moment) and total volume density (third moment) can then be calculated. If the size resolution is fine enough, moments can be calculated directly from histograms of size (FCAS, NMASS, and CARIBIC). For coarser measurements, such as the WOPC, the measurements are often fit with unimodal/bimodal lognormal size distributions for moment calculations. Table A1 includes a summary of the temporal and spatial distribution of the size distribution measurements from these three sets of instruments.

In situ measurements of stratospheric aerosol size distribution require sensitivity to sizes less than 1 μm and to only one particle in the beam at a time. Size is determined by the scattered light intensity, assuming spherical particles and Mie scattering (WOPC and FCAS), while the number concentration is determined by the pulse frequency. Theoretical estimates of instrument response are checked with standard calibration aerosol, which are also used for calibrating instruments prior to deployment. Due to the range in scattering intensity for particles between 0.05 and 10 μm, exceeding 1000 μm, multiple gain stages are required. The FCAS is sensitive to particle radii between 0.05 and 0.5 μm with 20 channels, the WOPC to particles between 0.15 and 2.0 μm in 8–12 channels. In addition to aerosol size spectrometers, CN counters are designed to measure the total aerosol concentration through exposing particles to a supersaturated region to force particles to grow to optically detectable sizes before the particles are counted. The Wyoming CN counter is nominally sensitive to 10 nm particles. The NMASS is a battery of five CN counters with a different condenser temperature. Thus, each CN counter has a different lower radius cut point at approximately 2, 4, 8, 15, and 26 nm. Since particles enter the scattering chamber through an inlet, care is required to account for aerosol changes due to heating and evaporation [*Jonsson et al.,* 1995] or particle losses in the air inlet and downstream

sampling lines [*Krämer et al.,* 2013]. For the stratosphere such instruments are deployed on balloons and aircraft. As a result, the measurements are spatially and temporally limited.

Uncertainties in the fundamental measurements are driven by uncertainties in the measured size and number concentration. Uncertainties in size of 10% or less for the WOPC and 2.5% for FCAS are due to (i) variations in scattering response, (ii) variations in particle index of refraction or shape for similarly sized particles, and (iii) pulse width broadening of photodetectors. Uncertainties in number concentration of 10% or more are due to the consistency of multiple calibrations and Poisson counting statistics. Thus, uncertainties increase as particle concentration decreases. Finally, there are uncertainties in the assumptions of temperature distributions in the sampling inlets with subsequent impact on the evaporation of water from the sampled particles and on measurements of sampling efficiency of the inlet for instruments on aircrafts. The WOPC, FCAS, and NMASS all account for the evaporation of water from sulfuric acid and water particles as the particles pass into the scattering chamber. WOPC measurements from 1990 to 2010 have recently been corrected for a systematic calibration bias, affecting the measurements during periods of low aerosol loading [*Kovilakam and Deshler*, 2015]. Such uncertainties lead to overall precisions on aerosol moments of ±40% for WOPC [*Deshler et al.,* 2003] and ±25% for FCAS [*Jonsson et al.,* 1995].

4.2. Ground-Based Lidar Measurements

Measurements of stratospheric aerosol using a lidar began soon after the visible wavelength laser was developed in the early 1960s [*Fiocco and Grams*, 1964]. These measurements began nearly simultaneously with in situ measurements of stratospheric aerosol. The technique relies on detecting the light from a pulsed laser, which is backscattered from air molecules and the ensemble of particles in the volume of air illuminated by the laser. To obtain the aerosol backscatter coefficients, the backscatter signal must be calibrated by comparison with the Rayleigh backscatter signal in altitude ranges without aerosol, typically at altitudes above 30 km. The Rayleigh component of the backscatter signal is directly determined from the atmospheric density calculated using temperature and pressure measurements from nearby radiosonde measurements, satellite measurements, or climatologies. The vertical sampling interval is typically 75 m [e.g., *Jäger*, 2005], and the sampling is performed during nighttime. While aerosol backscatter coefficients are the native measurement, aerosol extinction coefficients are needed for radiative transfer calculations. This requires an assumption about extinction-to-backscatter ratio, also known as the Lidar Ratio, which can vary widely. Tropospheric values vary from 20 to 70 sr^{-1} km^{-1} or more, peaking around 50 sr^{-1} km^{-1} [*Illingworth et al.,* 2015]. Stratospheric values of the Lidar Ratio vary much less and have been calculated from measurements with a Raman lidar [*Wandinger et al.,* 1995], the WOPC in situ measurements [*Jäger and Deshler*, 2002, 2003], and by comparing lidar with SAGE II measurements [*Antuña et al.,* 2003]. The ratios for the stratosphere are typically between 45 and 50 sr^{-1} km^{-1} at 532 nm, and with the lower values representing newer aerosol. Detailed information on particle size and number can only be inferred by using multiple laser wavelengths [*Post*, 1996]. Information on particle shape is possible if the lidar has channels to receive both the polarized and cross polarized signals. The extent of cross polarization is an indication of nonspherical particles in the sampling volume and is useful in distinguishing between cirrus and aerosol.

Lidar measurements of extinction coefficients are possible but limited to periods of strong volcanic activity when an attenuation of the backscattered light in the aerosol layer can be distinguished. The two methods that can be applied to retrieve aerosol extinction coefficients are Raman backscattering [*Ansmann et al.,* 1992] or spectrally filtering the atmospheric return in a separate detection channel for eliminating its narrow-band aerosol component (so-called high-spectral-resolution lidar) [*Eloranta*, 2005]. While both techniques have been widely used with tropospheric lidars, extinction channels have only more recently been added to stratospheric aerosol lidars.

Long-term measurements using lidar began in the mid-1970s, and two sites have maintained a continuous record since then (Table A1) [e.g., *Hofmann et al.,* 2009; *Trickl et al.,* 2013]. Once the instrument is in place, the advantage of lidar measurements is their ability to make relatively frequent routine measurements at minimal cost. However, lidars are restricted spatially, except for spaceborne lidar (such as the Cloud-Aerosol Lidar with Orthogonal Polarization (CALIOP); http://www-calipso.larc.nasa.gov/). For ground-based lidars, clouds, except for thin cirrus, generally prevent stratospheric lidar measurements, introducing a bias toward clear weather conditions. Lidar measurements of stratospheric aerosol have generally been used for long-term monitoring of trends, seasonal cycles, and identification of new layers.

Ground-based lidars remain very useful, providing unique information for complementing and validating satellite instruments, for filling gaps between satellite missions, and for filling gaps in vertical profiles, where the stratospheric burden exceeds the dynamic range of other measurement approaches, such as limb-viewing space-based measurements (section 4.3) during periods of high aerosol loading. Also in the near future, beyond the end of the existing and planned satellite missions, there may not be appropriate satellite instruments at the time of the next volcanic eruption. In that situation, it is possible that ground-based lidar stations might be a nearly exclusive source of information.

Uncertainties in the lidar backscatter result mainly from statistical uncertainty in the return signal. The error at a given altitude includes the signal error at that altitude, the error in the normalization altitudes, and the error in calculating the extinction between these altitudes [*Russell et al.,* 1979]: assumptions about the aerosol properties and molecular density also contribute. Further uncertainty arises from the assumption that the signal at a given altitude range is pure molecular backscatter or that the ratio of aerosol and molecular scatter is known at that altitude. Modern lidars normalize assuming a molecular-only dependence in backscatter at altitude ranges around 30 km and higher, but historically some lidars normalized to the tropopause region where the signal is stronger and the atmosphere was thought to be relatively clear of aerosol. However, aerosol is never completely absent in either region, and the unresolved aerosol contribution leads to an underestimate of stratospheric aerosol throughout the profile. Furthermore, light absorption by ozone at 532 nm may introduce small uncertainties and must be accounted for.

Since the lidar signal is corrected for aerosol extinction, errors in the extinction-to-backscatter ratio also contribute to the total backscatter error at a given altitude. This contribution is small during volcanic quiescence periods when the extinction is small, but could be significant following large volcanic eruptions. There are two analysis methods to deal with the circular problem of needing to know the aerosol extinction profile before the aerosol profile can be calculated. The first single-pass method [*Klett*, 1985] derives the backscatter coefficients directly from the backscatter signal, even allowing for the application of Lidar Ratios varying with altitude. The second method starts with an assumed aerosol backscatter profile and then iterates the retrieval until the profile converges to a self-consistent backscatter profile [*Jäger*, 2005].

From the backscatter coefficients, extinction coefficients, or other aerosol properties such as number, surface area, and volume can be derived by mathematical approaches such as Mie theory based on a measured aerosol size distribution [*Jäger and Deshler*, 2002, 2003; *Jäger*, 2005]. The highest uncertainties would arise from fresh aerosol immediately following volcanic eruptions, when the composition, shape, and sizes are changing rapidly. The uncertainties in the derived quantities would decrease as the aerosol distribution ages.

Ground-based lidar data sets of stratospheric aerosol remain disperse, and many of them are not openly available. The only existing effort in this direction has been led by the Network for the Detection of Atmospheric Composition Change lidar working group (http://ndacc-lidar.org/), with the participation of 30 ground-based lidar instruments. In addition, a set of global lidar measurements from Mount Pinatubo was collected in the past, but several of the ground-based lidar measurements produced at that time are still missing [*Antuña et al.,* 2002]. Preserving lidar data sets is crucial to depicting the stratospheric aerosol burden during volcanic eruptions such as Mount Pinatubo and El Chichón. These data sets are an important part of the available data for these events and the return to quiescence periods.

4.3. Space-Based Measurements

Depictions of the long-term, global stratospheric aerosol distribution, often used as inputs to chemistry-climate models, are primarily based on a series of space-based measurements of aerosol optical properties. In and prior to the *SPARC* [2006] report, the data set was a composite of measurements made by a number of satellites with concomitant requirements for homogenizing the measurements across the instruments. This was mostly straightforward since these satellite instruments used essentially the same method to measure aerosol properties: solar occultation. These include the four members of the SAM/SAGE series (see Table A1). SAGE II, which operated between 1984 and 2005, is the most prominent member of this series: it observed the stratosphere through the recovery of the El Chichón eruption (1982), the Pinatubo enhancement (1991–1996), the clean period from 1999 to 2002 and into the post-2002 variable period [*Thomason et al.,* 2008]. The solar occultation group also includes the Polar Ozone and Aerosol Measurement (POAM II) instrument (1994–1996) [*Randall et al.,* 2000], the POAM III instrument (1998 to 2005) [*Randall et al.,* 2001], and the Halogen Occultation Experiment (HALOE) that made aerosol extinction coefficient measurements

at four infrared wavelengths between 2.45 and 5.26 μm [*Hervig et al.,* 1996]. These instruments are discussed in detail in *SPARC* [2006] (and elsewhere), and that discussion will not be repeated here.

Exceptions to the solar occultation instrument are the Cryogenic Limb Emission Spectrometer (CLAES) (1991–1993) and Improved Stratospheric and Mesospheric Sounder (ISAMS) (1991–1992), which use atmospheric limb emission to infer aerosol absorption coefficient in the stratosphere. Their measurements occurred during the peak of the Pinatubo enhancement [*Lambert et al.,* 1996; *Massie et al.,* 1996] and, as such, are available throughout a period in which many SAGE II observations are missing in the lower stratosphere due to the extreme opacity of the Pinatubo-derived aerosols.

While these measurements are robust over a broad range of aerosol levels, each approach has limitations. Solar occultation measurement locations are dependent on the details of the platform orbit and, at best, provide near-global coverage on a quasi-monthly basis, in contrast to limb emission instruments such as CLAES, where a near-global depiction of aerosol properties is possible on a daily basis [*Toohey et al.,* 2013a]. During extremely high aerosol loading (e.g., the peak of the Pinatubo event) the very high atmospheric opacity, particularly at near-infrared and shorter wavelengths, leads to termination of measurements well above the tropopause, leading to important gaps in the stratospheric aerosol record [*Thomason et al.,* 1997]. Conversely, during low aerosol loading periods it is challenging to extricate the aerosol signature at infrared wavelengths because the signal is dominated by absorption of gaseous species [*Thomason*, 2012]. Identifying the presence of clouds in all these observations is often difficult or ambiguous [*Kent et al.,* 2003].

As the *SPARC* [2006] report was completed, solar occultation measurements of stratospheric aerosol stopped: the SAGE II, SAGE III, POAM III, and HALOE missions all ended between August and December 2005. As a result the post-*SPARC* [2006] satellite data record depends on new instruments and entirely different techniques for measuring aerosol. The new approaches include limb scatter, nadir-viewing lidar, and stellar occultation. While all these techniques provide near-global stratospheric aerosol spatial depictions on short, even daily, timescales [*Toohey et al.,* 2013b], they still present unique challenges to a homogeneous long-term aerosol data set.

The limb scatter technique is employed by the Optical Spectrograph and InfraRed Imaging System (OSIRIS) (2002-present) [*Bourassa et al.,* 2007] and involves observing the illuminated atmosphere on the sunlit portion of the orbit without directly observing the Sun. With multiple profiles typically scanned each orbit, OSIRIS has provided over 850,000 aerosol extinction profiles since 2002 (compare to about 170,000 over the 20+ year SAGE II lifetime). The determination of an aerosol extinction coefficient profile from these measurements has a second-order dependence on knowledge of the aerosol size distribution [*Bourassa et al.,* 2007]. In practice, a sufficient determination of aerosol phase function can be made using limb scatter aerosol measurements at two or more wavelengths rather than relying on externally provided aerosol size information [*Rieger et al.,* 2014]. The vertical resolution is somewhat lower than SAGE II, but this is not critical for most applications. Observations in the lower stratosphere and the troposphere, particularly in the tropics, require some care as the presence of clouds and optically thick aerosol may have an impact on the inferred extinction levels; observations below 15 km altitude are often not available at middle and high latitudes [*Bourassa et al.,* 2012a; *Fromm et al.,* 2014].

Lidar measurements by the CALIOP (2006-present) offer the highest vertical resolution data of all space-based observations [*Vernier et al.,* 2011b]. Unlike the previous space-based instruments discussed, which measure extinction, CALIOP measures aerosol backscatter coefficient and polarization. Thus, CALIOP requires a change in the measured parameter (backscatter to extinction), similar to the ground-based lidar, that may add bias that impacts long-term aerosol data set continuity. Only nighttime CALIOP data are useful for stratospheric applications due to signal-to-noise issues, and even these observations have relatively low signal-to-noise levels and require substantial averaging to be useful (0.5 km vertical and 500 km horizontal) [*Vernier et al.,* 2011b]. The polarization measurement probably offers the least ambiguity in accounting for cloud presence of any space-based measurement [*Vernier et al.,* 2011b]. However, it is possible for solid aerosol such as ash to be incorrectly identified as "ice cloud" and to be then removed from aerosol-only evaluations, but this is not affecting climatological values above the tropopause. Absolute calibration uncertainty for CALIPSO is on the order of 2% (relative to molecular backscatter) [*Rogers et al.,* 2011] and leads to potential bias in the observations. This level of uncertainty is probably not

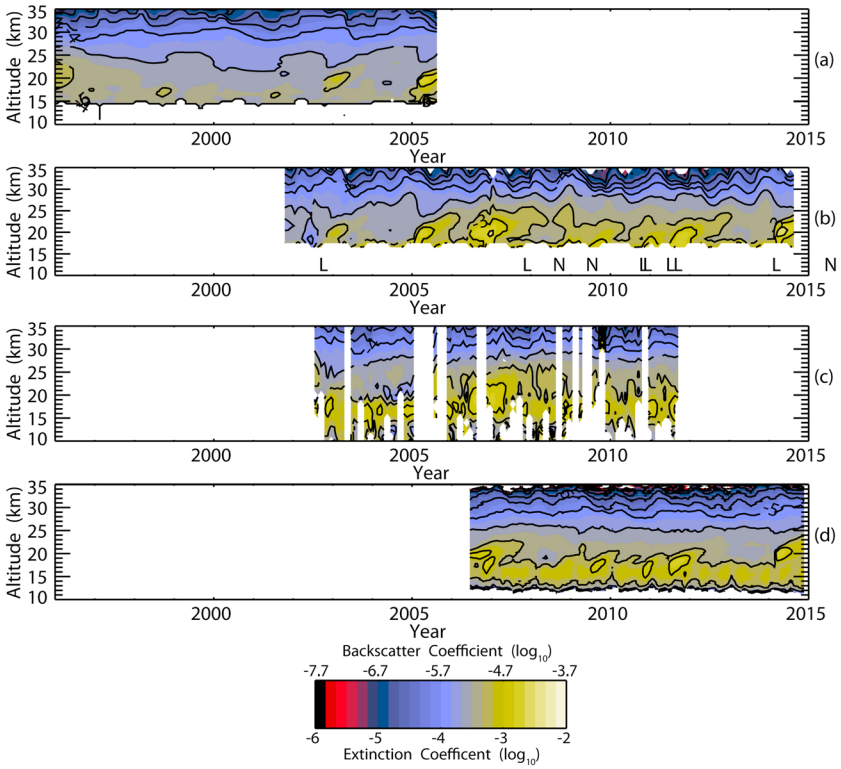

Figure 8. The 1 month by 0.5 km mean aerosol parameter between 10°S and 10°N as measured by (a) SAGE II (525 nm extinction coefficient), (b) OSIRIS (converted to 525 nm extinction coefficient), (c) GOMOS (500 nm extinction coefficient), and (d) CALIPSO (532 nm backscatter coefficient). The letter annotations in Figure 8b refer to the time of low latitude (L) and northern high-latitude/midlatitude eruptions (N) whose effects are visible in the figures. Contours are in log10 with black line contours every 0.5 units and color contours every 0.25 units. The color scale is the same for Figures 8a to 8c but has been scaled by a factor of 1/50 for Figure 8d to account for the conversion of midvisible backscatter coefficient to extinction coefficient at the same wavelength and, thus, improve the visual consistency of these images. For all instruments, white areas indicate missing data due to either times outside of the mission lifetime or periods where data are otherwise unavailable.

significant for tropospheric observations; however, it is a significant fraction of background stratospheric levels, which are only 5 to 10% above molecular levels.

Stellar occultation is similar to solar occultation except for the choice of target. An advantage of this method resides in the increased number of available light sources during each orbit at all times and geographical location. The Global Ozone Monitoring by Occultation of Stars (GOMOS) instrument (2002–2012) aboard the European Envisat platform used this method to deliver more than 375,000 aerosol extinction profiles. These measurements are somewhat noisier than solar occultation measurements, on an event-by-event basis, due to lower light intensities [*Vanhellemont et al.,* 2005, 2010], which is, however, compensated for by a much larger number of occultations per orbit. Other challenges include a crucial requirement to account for scintillation effects in the observations and a less critical dependence on individual star properties [*Vanhellemont et al.,* 2010]. Furthermore, the current GOMOS data version (IPFv6.01) delivers aerosol extinction coefficients at only one wavelength (500 nm). The limited information content prevents the use of spectral dependence to identify clouds using the methods commonly proposed in the literature. Therefore, the GOMOS data set requires caution using it below 20 km and particularly below the tropopause. The vertical resolution for GOMOS is somewhat broad compared to solar occultation (about 4 km) [*Vanhellemont et al.,* 2010], which is generally not a critical issue.

Several other Envisat instruments have shown potential for producing valuable space-based measurements of volcanically derived aerosols. In particular, *Griessbach et al.* [2015] have shown that MIPAS measurements can be used to discriminate between ash and sulfate aerosol associated with relatively modest volcanic

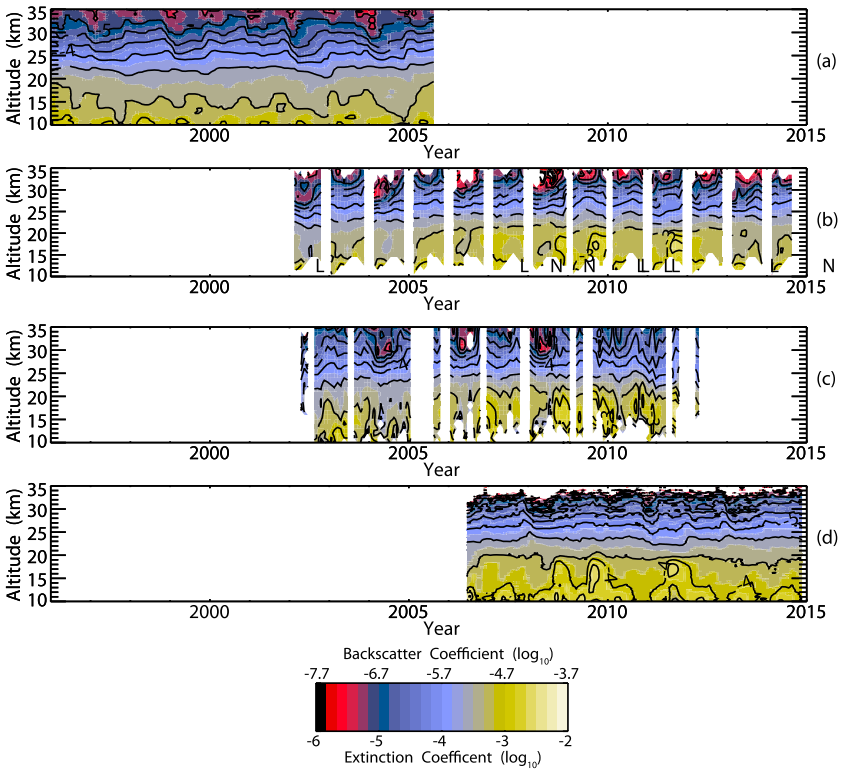

Figure 9. The same as Figure 8 but for 35° to 45°N.

injections into the UTLS for at least several months following an eruption. Similarly, IASI has demonstrated, following the 2008 Kasatochi eruption, a capacity for measuring SO_2, ash, and sulfate aerosol with fairly broad vertical resolution [*Karagulian et al.*, 2010]. To our knowledge neither of these instruments produces a routine stratospheric aerosol product but, nonetheless, demonstrates the potential to contribute to a broader understanding of the impact of volcanic events on the composition of the stratosphere.

4.3.1. Discussion of the Different Satellite-Based Data Sets

Figures 8 and 9 show midvisible aerosol extinction or backscatter coefficient for four of the instruments described above for the tropics (approximately 0°) and northern midlatitudes (approximately 40°N). Color scales and contours are the same for the extinction coefficient plots (SAGE II v7.0, OSIRIS v5.07, and GOMOS IPFv6.01). OSIRIS data have been scaled to 525 nm using the technique as described in *Rieger et al.* [2015]. The contours are different for the CALIPSO (v4) backscatter coefficient plots, but the color scale has been scaled by a factor of 50 to approximate the extinction-to-backscatter ratio observed for stratospheric aerosol [*Jäger and Deshler*, 2002, 2003]. Each satellite data set has been cleared for clouds presence using methods described in *Thomason and Vernier* [2013] for SAGE II, in *Rieger et al.* [2015] for OSIRIS, and in *Vernier et al.* [2009] for CALIPSO. Generally, cloud presence begins to reduce the available aerosol observations from slightly above the tropopause downward. GOMOS data products are currently not cloud cleared (section 4.3), and as a result, GOMOS data at and below the tropopause are possibly cloud contaminated. In Figure 8a, the end of the aerosol enhancement associated with the Pinatubo eruption is evident (particularly in the tropics) through at least mid-1998. The period between the apparent end of Pinatubo and mid-2002 is the cleanest period in the space-based aerosol record with measurements approximately 30% less than the previous lowest extinction levels observed in 1979 by SAGE. In 2002, the tropical analysis shows an aerosol enhancement associated with the September 2002 eruption of Ruang (Indonesia) initially centered at 20 km with the peak eventually rising to about 23 km. This feature is also captured by OSIRIS (Figure 8b) and GOMOS (Figure 8c). In early 2005, the eruption of Manam (Papua New Guinea) appears near 19 km (the last significant volcanic event of the SAGE II lifetime) and again shows evidence of lifting by the end of the SAGE II record 7 months later. Neither of these events is particularly noticeable in the Northern Hemisphere but both produce a measureable enhancement in the south (not shown).

The 2006 eruption of Soufriere Hills is apparent in OSIRIS, GOMOS, and CALIPSO data sets (Figures 8b–8d) and is the largest eruption until the Kelud eruption in 2014 which is observed in the CALIPSO and OSIRIS data sets (see Figures 8b and 8d). In 2008 and 2009, several middle- and high-latitude volcanic events and an unusual fire event (the "Black Saturday Bush Fires" in the Southern Hemisphere [*Siddaway and Petelina*, 2011]) had clear stratospheric impacts (no figure for the Southern Hemisphere is shown). All the data sets see tropical impacts from the Northern Hemisphere volcanic eruptions of Kasatochi, Okmok (which is substantially masked by the Kasatochi eruption), and Sarychev despite the relatively high latitude and primarily lower stratospheric location of the sulfur injection produced by these eruptions. The 2011 Nabro eruption has clear impacts in both the tropics and the midlatitudes as seen in Figures 8b, 8d, 9b, and 9d [*Clarisse et al.,* 2014]. These eruptions were reaching the UTLS, with primary impacts centered at about 19 km, but having some initial impact above 20 km. Later, material from these eruptions is observed at altitudes around 25 km due to transport by the general upwelling in the tropical stratosphere. The exception is the 2014 eruption of Kelud, which produced an aerosol enhancement initially focused between 18 and 23 km (Figures 8b and 8d), which implies the highest significant injection height of volcanic material since the Pinatubo eruption. Qualitatively, the records shown here, despite the diverse measurement approaches, indicate a reassuringly consistent picture of global aerosol variability during the past two decades. Despite this, it is not clear how the change in measurement paradigm affects the continuity and the consistency of the data record for the SAGE to OSIRIS/GOMOS/CALIPSO period. The key for maintaining the ability to infer trends across instrument changes depends on the consistency of the measurements, knowledge of bias, and the consistency of any bias. This is more complicated for aerosol since construction of a composite data set may require a change in wavelength (SAGE, OSIRIS, and GOMOS) or measurement type (e.g., extinction from backscatter; CALIPSO) that depends to some degree on a priori or poorly known aerosol attributes.

Bourassa et al. [2012a] show that SAGE III 755 nm and OSIRIS 750 nm aerosol extinction coefficient are consistently well correlated and biased no worse than about 10%. A more recent comparison of SAGE II and OSIRIS [*Rieger et al.,* 2015] shows a comparison of OSIRIS converted to 525 nm with SAGE II measurements at the same wavelengths. This is also consistent though the bias can be as large as 20%. A comparison of SAGE II, POAM III, and SAGE III showed broad agreement among these instruments [*Thomason et al.,* 2010]. Excluding measurements in the UV, SAGE II, and SAGE III, bias levels were no more than 10% at any wavelength and often much less. Similarly, the biases between SAGE III and POAM III were generally less than 20% except at very low extinctions, which were in poor agreement particularly at 1020 nm. *Vanhellemont et al.* [2010] showed comparisons of GOMOS 500 nm aerosol extinction with SAGE II at 525 and POAM III at 603 nm. They found biases on the order of +10 to −20% between 15 km and 25 km altitude with SAGE II, an agreement within 20% with SAGE III in the altitude range from 11 to 20 km, and an excellent agreement with POAM III below 20 km altitude but with rapidly decreasing quality above that.

In summary, the bias levels between instruments have been reported as generally less than 20% and fairly well behaved over time. This is an area where further work is required [*Rieger et al.,* 2015]. The degree to which this consistency is maintained governs the ability to infer trends or change across the instrument periods. However, it is difficult to imagine that trends (or differences between time periods) less than 10 to 20%, away from large volcanic events, can be inferred across instrument eras with confidence. To the degree to which they can be reconciled, the 13+ years OSIRIS data record offers the possibility of the most seamless continuity with the 21 year SAGE II record, particularly having the advantage of a 4 year overlap period [*Rieger et al.,* 2015].

4.4. Comparing Aerosol Measurements

Comparing aerosol measurements across airborne and balloon-borne in situ particle counters, surface-based lidar, and satellite-based solar occultation and limb scattering techniques is a challenge. Figures 8 and 9 show the results comparing various satellite instruments, which almost all provide the same native measurement, aerosol extinction. Comparing these measurements to in situ optical particle counters and lidar, whose native measurements are size distribution and backscatter, adds another level of difficulty. The approach taken here is to compare aerosol optical depth (AOD) from all three classes of instruments, and aerosol surface area and volume at selected altitudes for the airborne and satellite instruments. Given the multidecadal WOPC record from the University of Wyoming (40°N), we conduct these comparisons at that latitude. While comparing AODs from the various instruments/platforms will not allow differences in profile structure to be investigated,

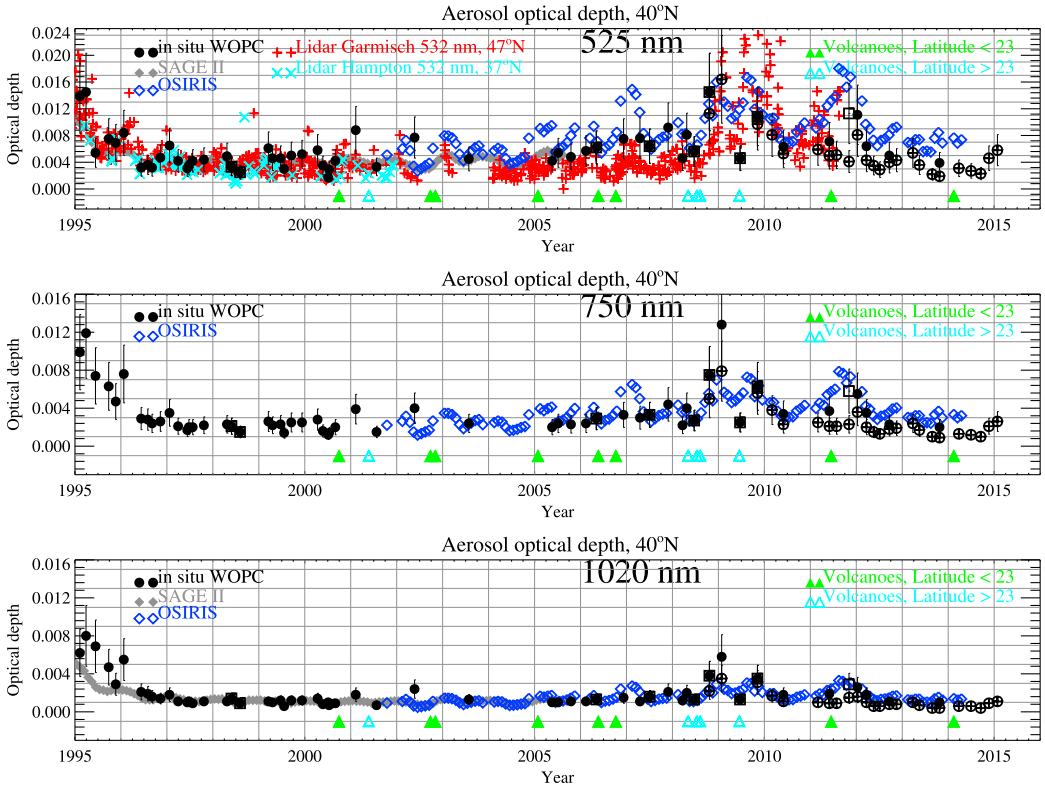

Figure 10. History (1995–2015) of aerosol optical depth (AOD) at 40°N at 525, 750, and 1020 nm calculated from profiles of in situ particle size measurements above Laramie, Wyoming, USA (41°N) (WOPC, black and grey dots with uncertainty bars), profiles of aerosol extinction at 525 and 1020 nm from SAGE II (blue dots) and at 750 nm from OSIRIS (blue diamonds), and integrated backscatter at 532 nm from two lidar sites, Garmisch-Partenkirchen, Germany (47°N, red pluses), and Hampton, Virginia, USA (37°N, cyan cross). Integrated backscatter is converted to AOD using an extinction-to-backscatter ratio of 50 [*Jäger and Deshler*, 2002, 2003]. Spectral extinctions are calculated from in situ particle size measurements using refractive indices appropriate for sulfuric acid and water aerosols. The occasional open black squares with uncertainty bars are from a second WOPC flown occasionally for comparison; a filled square indicates a nearly perfect match between the two WOPCs flown. The grey dots after 2008 are from a new instrument [*Ward et al.,* 2014] used for the WOPC record. The timing of volcanic eruptions at latitudes $<20°$ are shown by the green triangles, and eruptions at latitudes $>20°$ are shown with cyan triangles along the bottom of each panel. The AODs at 525 and 1020 nm from OSIRIS are derived from the version 5.07 measurements at 750 nm by assuming the constant particle size used in the retrieval.

the integral quantity illustrates how well the conversion to extinction from the nonnative instruments works, and how well all instruments compare in their profile integrals estimating AOD. The comparison of surface area and volume is chosen because of the importance of surface area for stratospheric chemistry, geometric cross section for radiative impacts, and volume for estimates of aerosol mass. These are primarily tests of the inversions used to convert aerosol extinction from satellite measurements to surface area and volume.

From 1995 to 2015, AOD above the thermal tropopause at 40°N at 525, 750, and 1020 nm, from in situ, satellite, and lidar measurements is shown in Figure 10. The in situ and lidar measurements are single daily measurements, while the satellite data are monthly zonal averages over 5° latitude bins. The thermal tropopause was identified from direct measurement for the in situ data, from nearby radiosonde measurements for the lidar data, and from the National Center for Environmental Prediction reanalysis for the satellite measurements. Missing data near the thermal tropopause are not an issue for the in situ and lidar data, while the satellite data are monthly zonal averages over 5° latitude bins, so missing extinction values are filled in with neighboring values. Overall, the agreement among the various platforms is within the measurement uncertainties, while there are some disturbing differences. The lidars, WOPC, and SAGE II measurements capture the decay of the Pinatubo aerosols and the relative minimum in aerosol in the late 1990s and early 2000s up to 2002. While there are a few days when the WOPC overestimates SAGE II, the SAGE II estimates fall within the ±40% precision of the WOPC estimates. The period 2002–2005 suffers from a lack of WOPC and lidar

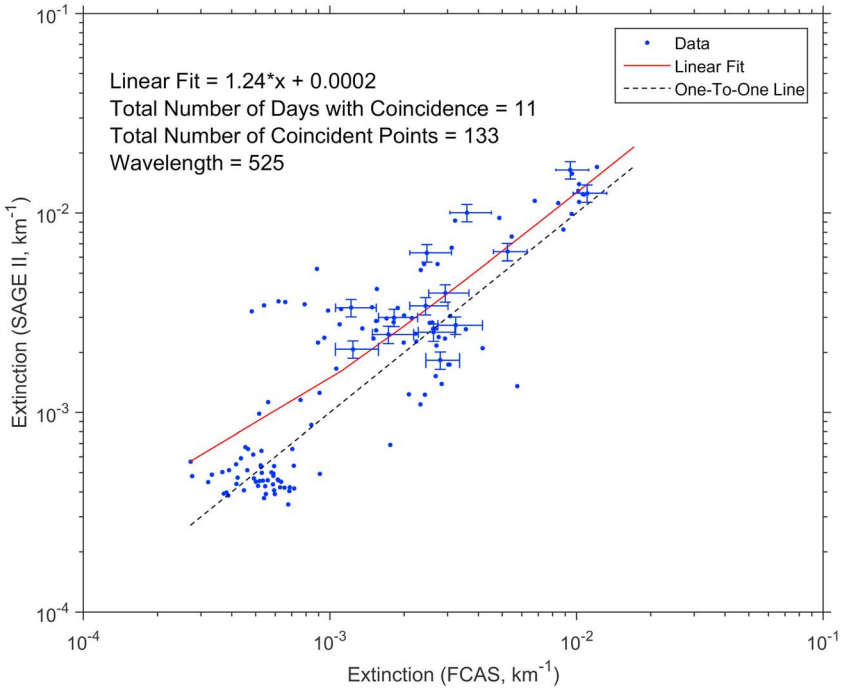

Figure 11. Scatterplot of 525 nm extinctions calculated from FCAS aircraft measurements and from coincident SAGE II measurements (blue dots) including their uncertainties for a selected number of measurements. The one-one line (dashed line) and a linear fit to the data (red line) are also included.

measurements, but SAGE II and OSIRIS agree well, particularly at 1020 nm. The increasing AOD beginning in the mid-2000s is most evident in OSIRIS which diverges from the Garmisch lidar measurements and WOPC that are in reasonable agreement. In 2008 the impact of several high-latitude eruptions is registered on all platforms and they come back into agreement. The disagreement between WOPC and OSIRIS, observed prior to 2009, is again manifested as the aerosol decays following Nabro in 2011. The impact of the low-latitude eruptions in 2002, 2005, and 2006 are most apparent in OSIRIS, while SAGE II registers the first two eruptions but without as much impact as seen in OSIRIS measurements. There is a slight seasonal oscillation in AOD with a minimum in summer, potentially caused by the elevated summer tropopause in the midlatitudes. The Garmisch and Hampton lidars are in agreement up to the end of the Hampton record in 2001, including the unusually high AOD in late 1998. This high AOD observed in 1998 is probably a signature of smoke from the Canadian wildfires in August 1998 [*Fromm et al.,* 2005]. The lidars are also in fair agreement, aside from the occasional outliers, with SAGE II up until 2001, in contrast to post-2004 when the Garmisch lidar underestimates SAGE II. This difference maybe is the result, in part, of a static extinction to backscatter ratio applied throughout the record but this has not been further explored.

Figure 11 demonstrates the reasonably good agreement of FCAS in situ measurements with SAGE II measurements as presented earlier [*Reeves et al.,* 2008]. Most comparisons are close to, and scattered around, the one-one line throughout the extinction range, 5×10^{-4} to 10^{-2} km^{-1}. There are a handful of measurements, when FCAS strongly underestimates moderate 525 nm extinctions from SAGE II.

The aerosol size distribution is essential for understanding and modeling the impacts of aerosol. Aerosol radiative impacts are related to cross sectional area, chemical impacts to surface area, and aerosol mass budget to aerosol volume, all of which can be derived from size distribution measurements. Obtaining these quantities from remote measurements requires somewhat complicated inversions and is poorly constrained. The initial inversions of SAGE II measurements relied on principal component analysis [*Steele et al.,* 1999], while another approach was applied to the infrared HALOE data [*Hervig et al.,* 1998; *Hervig and Deshler*, 2002]. These approaches to obtain aerosol surface area and volume have been in reasonable agreement with in situ measurements during periods of relatively high aerosol loading, such as following the eruptions of El Chichón and Pinatubo [*Thomason et al.,* 1997], but are less successful during the volcanically quiescent period

since 1997 [*Thomason et al.,* 1997; *Deshler et al.,* 2003; *Reeves et al.,* 2008]. Both *Deshler et al.* [2003] and *Reeves et al.* [2008] showed that SAGE II version 6.0 surface area densities underestimated the in situ measurements by factors of 1.5–3. Complicating this comparison, in situ WOPCs underestimated SAGE II extinction by 50% during the volcanically quiescent period. These differences have now been reconciled with corrections for a systematic counting efficiency problem that plagued the WOPC instruments in use from 1990 to 2010 [*Kovilakam and Deshler*, 2015] and with the SAGE II version 7.0 surface area calculations [*Thomason et al.,* 2008].

Thomason et al. [2008] developed a new method to calculate aerosol surface area from SAGE II measurements for periods of low aerosol loading, which are now available in the SAGE II version 7.0 data. *Thomason et al.* [2008] assumed that the aerosol can be described by two monodispersed lognormal distributions [*Deshler et al.,* 2003], but that only the particles $>0.2\,\mu m$ are observable by SAGE II. The median radius of the large particle distribution is determined from the ratio of the 525 to 1020 nm extinction and then the number concentration from either extinction measurement. The SAGE II minimum surface area density is then calculated from the large particle mode. But this must be supplemented by the small particles, which provide the majority of the surface area during volcanically quiescent periods. Since the median radius of the small mode is not observable by SAGE II, two assumptions are made: (1) the uncertainties observed in the 525 nm extinction result at least partly from the small particles, and thus, these uncertainties can be used to infer the median radius of the small particle mode, and (2) the total aerosol number concentration is $20\,cm^{-3}$. This latter assumption is a bit higher than measurements [*Campbell and Deshler*, 2014] but is meant to provide a maximum surface area density. With assumption 2, and the number concentration in the large particle mode, the number in the small particle mode is given. The maximum SAGE II surface area is then the sum of the surface areas from the small and large particle distributions. In practice the surface area density reported by SAGE II is the average of the minimum and maximum surface areas, which essentially becomes half the maximum surface area since the minimum surface area is significantly smaller than the maximum in periods of low aerosol loading. If aerosol loading is significant such that the 1020 nm extinction approaches 70% of the 525 nm extinction, then the surface area density is calculated by the method applied to SAGE II version 6.2 [*SPARC*, 2006].

Figure 12 provides a history of 1 km averages of aerosol surface area and volume centered at 17, 20, and 23 km at $40 \pm 5°N$ comparing in situ and satellite measurements. The SAGE II [*Thomason et al.,* 2008] and OSIRIS [*Rieger et al.,* 2015] estimates are monthly zonal averages. The estimates from OSIRIS use the aerosol size distribution in the retrievals, which assume a lognormal distribution with a 80 nm median radius and a width of 1.6 [*Bourassa et al.,* 2012a]. These assumptions provide the scattering cross section from Mie theory. Since extinction is this cross section times the number density, the measured extinction directly provides aerosol number density. The three lognormal size distribution parameters are then used to derive aerosol surface area and volume density. In situ measurements from the WOPC are shown as data points with precision error bars, since each point is a single measurement. The FCAS data are shown over a temporal range, when the aircraft measurements extended over a period of time, or as single points for shorter measurement campaigns. In this case the FCAS data represent a number of measurements at the same altitude, but the standard deviations do not exceed the size of the pluses in Figure 12.

The overall temporal variability in AOD, shown in Figure 10, is also visible in Figure 12. The impact of the low-latitude eruptions in 2006, the high-latitude eruptions in 2008–2009, and Nabro in 2011 is clearly visible in the measurements at 17 km in both the WOPC and OSIRIS data. The impact of the volcanic eruptions on aerosol surface area and volume decreases with altitude, such that these eruptions are barely discernible in the 20 km measurements.

SAGE II version 7.0 surface areas show a significant improvement in the agreement with in situ data, both WOPC and FCAS, compared to the older SAGE II version 6.2 data. This is a reflection of the improved algorithms now used for the SAGE II data [*Thomason et al.,* 2008], which increased the surface area estimates from SAGE II, version 6. It is also a reflection of improvements in the WOPC data resulting from the collection efficiency corrections applied by *Kovilakam and Deshler* [2015]. With these improvements both platforms are in good agreement with the sparse FCAS measurements, as is OSIRIS. The comparison between the WOPC and OSIRIS degrades with altitude. At 17 km the agreement of WOPC and FCAS with OSIRIS is good, and both capture the impact of the Nabro eruption in 2011. However, there is a clear separation of OSIRIS and WOPC at

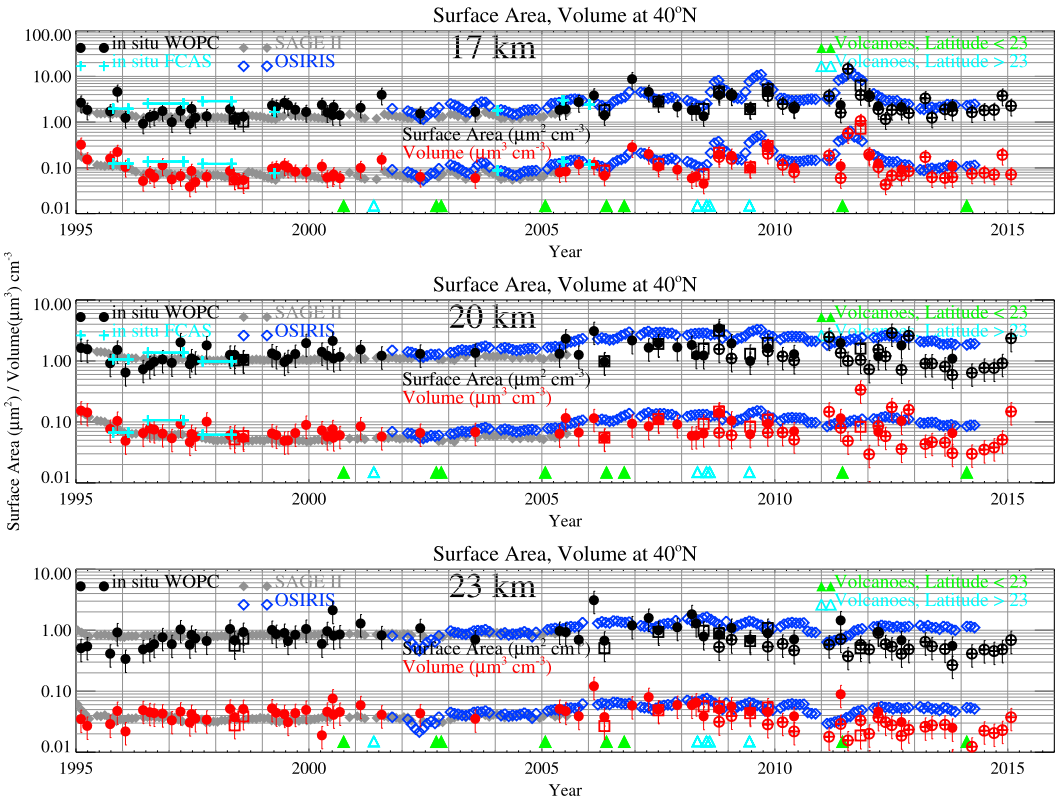

Figure 12. Stratospheric aerosol surface area and volume densities at 17, 20, and 23 km estimated from in situ aerosol size distributions from WOPC (black, red, and grey dots with uncertainty bars), FCAS (cyan pluses), extinction measurements from SAGE II (grey diamonds), and OSIRIS (blue diamonds). The satellite measurements are zonal averages at 40 ± 5°N. The timing of volcanic eruptions at latitudes <20° is shown in green triangles, while eruptions at latitudes >20° are shown in cyan triangles along the bottom of each panel. The occasional open square with uncertainty bars are from a second WOPC flown occasionally for comparison. The grey dots after 2008 are from a new instrument [*Ward et al.,* 2014] used for the WOPC record. The SAGE II surface areas are an average of the maximum and minimum surface areas estimated from SAGE II version 7.0 data [*Thomason et al.,* 2008]. The OSIRIS surface areas are derived from version 5.07 measurements of 750 nm extinction using the median particle size and distribution width assumed for the data retrieval.

20 and 23 km altitude, with OSIRIS estimates of surface area and volume densities greater than those derived from the in situ measurements. This may be a reflection of the assumptions on particle median radius and distribution width applied to the OSIRIS extinction measurements, which is the same at all altitudes, or it could reflect the shift to a new instrument for the WOPC measurements. Test flights with a new laser-based optical counter began in 2008, when the previous instrumentation was reaching the end of its life, which then became the dominant instrument for WOPC measurements at the beginning of 2010. The results from these measurements are shown as the grey filled circles between 2008 and 2015 in Figure 10. Measurements with the new instrument have been described by *Ward et al.* [2014]. The results of nine comparison flights are included in Figures 10 and 12 as duplicate measurements on the same day. Often, but not always, these show reasonable correspondence; however, there is a divergence of WOPC and OSIRIS and the new and old WOPC measurements as shown in Figure 12 at 20 and 23 km altitude. A similar divergence of WOPC and OSIRIS is observed in the post-2010 AOD comparisons (Figure 10).

Overall, the various stratospheric aerosol measurements demonstrate a satisfying consistency in reproducing quantities of geophysical interest across platforms and across measurement techniques. Together, these provide a cohesive picture of stratospheric aerosol since the early 1970s using lidar and in situ measurements, becoming global with the advent of SAM/SAGE in the late 1970s. The current agreement on surface area and volume across platforms is encouraging for modeling of the current and future atmosphere. The dependence on space-based measurements for global depictions of aerosol remains to have a potential for substantial uncertainties, particularly in the regions of the atmosphere where nucleation processes might be occurring.

Preparing for the Next Major Eruption

Injections of volcanic material into the stratosphere are relatively common, occurring on a timescale of about once per year. Most of these injections are small with little or no discernible impact on climate. Major volcanic eruptions that have an impact on climate generally occur on a multidecadal timescale and are impossible to predict much in advance. In this context, major volcanic eruptions refer to those that inject more than 1 Tg of sulfur into the stratosphere, such as the eruption of Tambora in 1815 or Mount Pinatubo in 1991. These major events can have a significant impact on climate by reducing solar radiation reaching the Earth's surface. Changes in regional and global weather patterns can not only impact surface air temperature but also rainfall and, thus, the availability of water for direct consumption and agriculture. As a result, depending on the magnitude of these changes, major volcanic eruptions could foster regional or global societal and political instability. Hence, an important focus for the climate science community is to understand the climate impact of a recent major eruption to advise national and international organizations, and nongovernmental organizations, on how to prepare for the next major volcanic eruption. What do we need to do to provide an accurate assessment of future climate impacts of a new major volcanic eruption? Alternatively, since the eruption of Mount Pinatubo is the best measured and most frequently modeled major volcanic eruption, we may ask "How much do we understand about the Pinatubo eruption, and where are our knowledge gaps?" Shortcomings in the ability of models to reproduce observed climate changes following this event provide insight into how to mitigate data gaps for future similar eruptions.

The ability to assess the impact of a volcanic eruption on seasonal to decadal scale climate variability and predictability depends crucially on representing the critical physical and chemical processes in climate models and providing realistic initial conditions. Climate simulation of major volcanic eruptions is an area with substantial progress over the last two decades [*Robock*, 2000; *Timmreck*, 2012]. Ongoing efforts such as those undertaken as a part of the Coupled Model Intercomparison Project Phase 6 (CMIP6) projects such as the Model Intercomparison Project on the climate response to Volcanic forcing (VolMIP) and Decadal Climate Prediction Panel focus on understanding the regional and large-scale short- and long-term climate effects of major eruptions and will lead to improvements in the model capabilities to accurately reproduce these climate effects. Accurate initial volcanic eruption and cloud parameters such as eruption length, amount of material released, its vertical distribution, and the initial rapid removal of sulfur on ice and ash particles, are essential for models to predict climate impacts realistically. While reasonable column estimates are available for SO_2 emissions from Pinatubo, very little is known about its initial vertical distribution. As a result, the vertical distribution of SO_2 in model simulations of the Pinatubo eruption varies significantly and is, in part, responsible for discrepancies in the simulated aerosol layer and inferred climate impacts between models. Space-based instruments like SAGE II provided substantial information regarding the dispersal of the Pinatubo plume. However, SAGE II was unable to measure the full depth of the Pinatubo layer in its densest periods due to its high opacity. While CALIPSO measurements would not be prone to these difficulties there are other challenges to using lidar-based observations. In any case, support from airborne and ground-based measurements is essential for a full characterization of the aftermath of a major eruption. Other current unknowns include understanding the role that chemical and other physical processes play within the original volcanic plume on the initial characteristics and distribution of aerosols. Furthermore, the degree to which the evolution of the volcanic layer depends on material directly injected as aerosols into the stratosphere, and the contribution of non-SO_2 aerosol precursors (sulfur and nonsulfur bearing) within the plume, is almost completely unknown. The role of ash in the aerosol nucleation process, its longevity, the impact of heterogeneous reactions on ash surfaces, and the radiative characteristics of the resultant aerosol mixtures are also not well understood. These issues need further investigation to understand future climate impacts of major volcanic eruptions.

Ultimately, preparing for the next major eruption places a burden on the science community to identify (i) what parameters need to be measured, (ii) existing or developing new instruments necessary to provide the required measurements, and (iii) a concept for a rapid climate model-based assessment of the short-term and long-term climate impact of any possible major volcanic eruption. A priority should be placed on developing a rapid-response capability to deploy balloon-borne or airborne instrumentation to obtain early (first days to weeks after the eruption) vertical profile measurements of the volcanic plume. Access to airspace and facilities can be an issue particularly for low-latitude and Southern Hemispheric eruptions. Hence, successfully obtaining early measurements in the tropics depends on developing cooperative relationships with science groups in these countries and preparatory exercise of the use of those facilities prior to a major volcanic event.

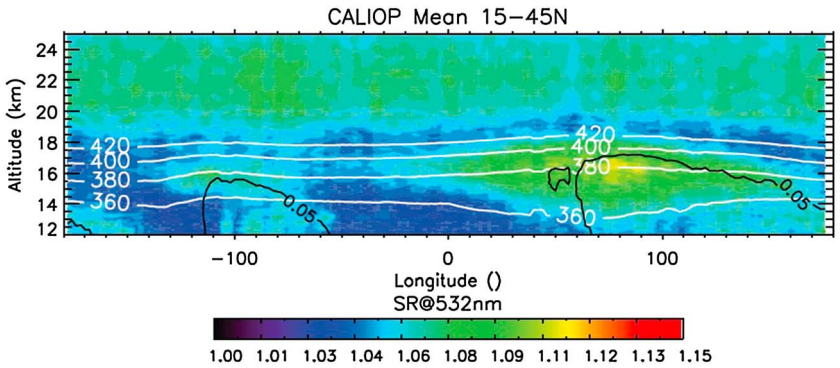

Figure 13. Latitudinal cross section of CALIOP scattering ratio averaged in July–August over five years (2006, 2007, 2008, 2010, and 2012) in which there is limited impact by volcanic activity between 15°N and 45°N. The contour denotes the mean volume depolarization contour of 0.05 (larger below the lines) and used a proxy for cloud presence. Figure is adapted from *Vernier et al.* [2015].

This consistency should improve our estimates of the chemical and radiative impact of stratospheric aerosol and guide our requirements for future stratospheric aerosol measurement activities.

5. Observed Changes in the Stratospheric Aerosol Loading

The remnants of Pinatubo were nearly entirely absent from the atmosphere by 1998. This is particularly clear in the tropics but is also true at higher latitudes where most tropical aerosol is transported on the way to permanent removal from the stratosphere in the polar vortex. The lowest stratospheric loading, as observed by multiple long-term measurement platforms (SAGE, in situ, and lidar; section 4) throughout the measurement era, occurred between 1999 and mid-2002. *Deshler et al.* [2006] found no significant trend in background aerosol for the period from the 1970s through 2004. Since 2002, stratospheric aerosol levels generally increased as observed by a number of platforms such as lidar [*Hofmann et al.,* 2009; *Trickl et al.,* 2013], CALIPSO [*Vernier et al.,* 2011b], and in situ and sun photometers [*Ridley et al.,* 2014], leading to discussion of a persistently variable but elevated stratospheric aerosol layer after 2002 [*Solomon et al.,* 2011]. The lowest stratospheric aerosol extinction coefficient levels observed by OSIRIS over its entire record (2002-present) occurred in early 2002. The next lowest OSIRIS values occur in 2013 but are still a factor of 1.6–2 larger at 20 km altitude and 1.3–1.4 larger at 24 km altitude compared to the 2002 levels. Elevated aerosol extinction coefficients, relative to 2002, are observed at all latitudes.

There has been considerable debate on the explanation for the observed increase. The initial suggestion was that the rapid rise in south Asian sulfur emissions [*Notholt et al.,* 2005] combined with deep convective activity during the South Asian Monsoon might contribute to this observed increase [*Hofmann et al.,* 2009]. Some observational evidence of this mechanism was found by *Vernier et al.* [2011c] who used CALIPSO observations that revealed the Asian Tropopause Aerosol Layer (ATAL) near 16 km in June to September (Figure 13) associated with the Asian monsoon anticyclone (see also section 2.1). A secondary aerosol maximum, but much weaker, in the UTLS can also be observed over Mexico and North America. An analysis of SAGE II data in these regions revealed similar features, but only after 1999 [*Thomason and Vernier*, 2013]. Contours for the CALIPSO cloud proxy (depolarization $>$ 0.05), shown in Figure 13, indicate a significant presence of ice clouds within ATAL and suggest a significant role for the convective transport of gas phase precursors and/or primary aerosol into the UTLS [*Vernier et al.,* 2015]. *Yu et al.* [2015] found that Asian emissions between 2000 and 2010 could be responsible for an associated increase of AOD within the ATAL by 0.002, which is in agreement with satellite observations presented by *Vernier et al.* [2015]. *Yu et al.* also found that ATAL is mostly composed of sulfates, surface-emitted organics, and secondary organics. A combined analysis of SAGE II and CALIPSO data sets suggests that aerosol levels over Asia from 13 to 18 km could have increased by a factor of 3–4 during the monsoon over the past 18 years [*Vernier et al.,* 2015]. This coincides reasonably well with the rapid increase in south Asian sulfur emissions [*Smith et al.,* 2011] as shown in Figure 14. Modeling by *Neely et al.* [2014] suggested that ATAL was predominantly the product of human-derived sulfur emissions with at least 30% of the sulfur coming from south Asia and suggested it existed prior

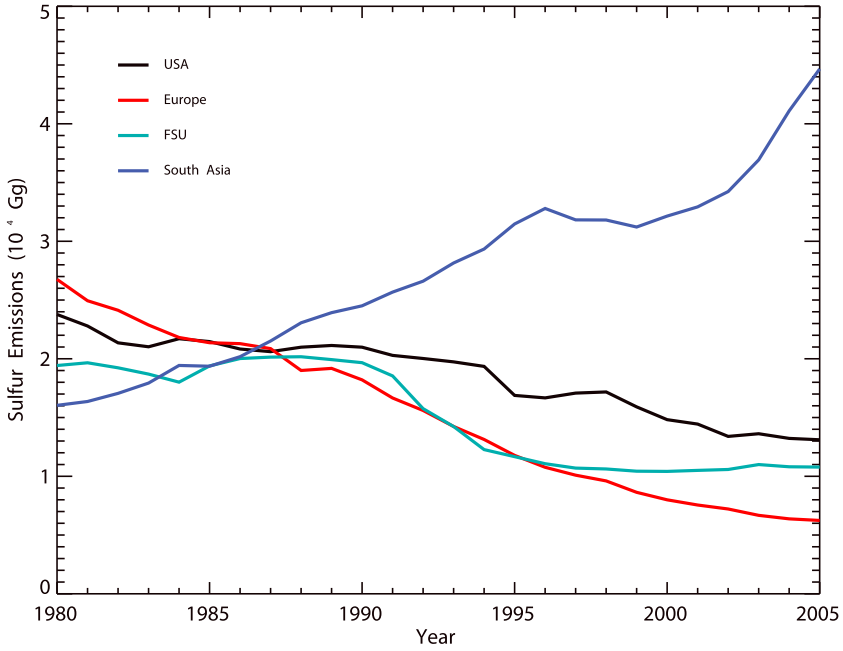

Figure 14. Global sulfur dioxide emissions by region (USA, Europe, Former Soviet Union (FSU), and South Asia). (Figure is adapted from *Smith et al.* [2011].)

to 1999 but was obscured by the remnant of the Pinatubo aerosol. Model studies performed by other groups suggest that the south Asian sulfur contribution to ATAL could be as high as 90% and generally supports the ATAL phenomenon as a recent development (see also section 3.1.4).

While the role of ATAL in modulating stratospheric aerosol levels remains unclear, *Vernier et al.* [2011b] found that low-intensity volcanic activity was the dominant source of stratospheric aerosol variability during the last 15 years. The space-based record clearly shows that the tropical stratosphere is modulated by a number of relatively small volcanic injections of aerosols and/or its precursors. Several of these injections reached only into the lower stratosphere, but eventually, the associated aerosols ascended into the mid-stratosphere through the tropical pipe associated with the BDC creating a volcanic aerosol "tape recorder." *Bourassa et al.* [2012b] suggested that the Asian monsoon provided a vehicle for the transport of aerosols and SO_2, associated with the Nabro eruption in 2011, into the stratosphere. While this specific attribution has proved somewhat controversial [*Fairlie et al.,* 2014; *Fromm et al.,* 2014], there seems little doubt that the monsoon is a possible pathway for tropospheric sulfur to enter the lower stratosphere and, thus, be a potential player in the observed increase in aerosol through the 2000s. Climate model simulations using the WACCM3 (Whole Atmosphere Community Climate Model, version 3) by *Neely et al.* [2013] compared emissions of minor volcanic eruptions and anthropogenic sources over the period from 2000 to 2010. The results of these simulations agree with the observations presented by *Vernier et al.* [2011b] and suggest that the variability in stratospheric aerosol is dominated by minor volcanic eruptions throughout the 2000s. Contributions of anthropogenic SO_2 via the Asian monsoon are minimal in comparison.

As Figure 8 shows, the tropical stratosphere has not been in a background state since the September 2002 eruption of Ruang [*Vernier et al.,* 2011b]. It is less obvious in the middle- and high-latitude aerosol records that volcanic activity is the predominant source of maintaining elevated aerosol levels after 2002. The transport of aerosol from low-latitude volcanic events (e.g., Manam, Soufriere Hills, and Kelud) is modulated by the stratospheric circulation that integrates and flattens out the pulses of aerosols from volcanic eruptions. The transport to higher latitudes can be slowed by the impedance to transport associated with the tropical pipe and modulated by the phase of the QBO [*Trepte and Hitchman*, 1992]. As a result, the signal of an eruption in extratropical measurements may appear gradually rather than as a single step increase [*Vernier et al.,*

2011b]. This broader and more diffuse volcanic signal complicates the effort to infer the significance of a human-derived source on stratospheric aerosol levels [e.g., *Hofmann et al.,* 2009]. While the importance of human impacts on stratospheric aerosol levels continues to be uncertain, there is some scientific consensus that the source of variability in stratospheric aerosol following the 1999–2002 clean period can be attributed primarily to episodic volcanic eruptions [*Vernier et al.,* 2011b; *Neely et al.,* 2013].

6. Stratospheric Aerosol Radiative Forcing and Climate Impact

Stratospheric aerosol plays a role in the radiative balance of the atmosphere by reflecting solar shortwave radiation back to space and by absorbing both longwave radiation emitted by the Earth and near-infrared solar radiation. The net change in radiative energy reaching the Earth's surface (radiative forcing) is negative for typical stratospheric aerosol size distributions. An increase in the stratospheric aerosol load produces anomalously negative radiative forcing and leads to global surface cooling. For example, after the Pinatubo eruption, a peak decrease of net radiative forcing of about 4 W/m^2, which is comparable in magnitude to the radiative forcing of doubling CO_2 [*Cess et al.,* 1993], was observed, along with a global mean surface temperature decrease of about 0.4°C [e.g., *Thompson et al.,* 2009]. Variations in stratospheric aerosol due to volcanic eruptions are the most prominent factor which shapes natural climate variability [*Hegerl et al.,* 2007].

Assessing the role of stratospheric aerosol in past climate variability requires knowledge of the history of aerosol and its radiative forcing. Therefore, climate models require information of stratospheric aerosol optical properties. Calculating these quantities online is numerically expensive, so that reliable offline forcing data sets are often used. These forcing data sets will be reviewed in section 6.1. The radiative volcanic aerosol forcing is strongly dependent on the eruption parameters (e.g., geographical location, eruption strength, material released, and timing), and the climate impact of eruptions cannot be properly assessed with prescribed forcing data sets only. This can only be done with coupled aerosol-climate models, which are the only tools to assess the specific contributions of natural (including volcanic) and anthropogenic SO_2 to the atmosphere's radiative balance and, therefore, their global and regional climate impact (section 6.2). Hence, the role of coupled aerosol-climate models becomes more and more important in climate science. These models will be discussed in section 6.2.2.

6.1. Aerosol Forcing Data Sets

Aerosol forcing data sets are composed of extinction coefficients, single scattering albedos, and asymmetry factors, all as a function of wavelength, integrated values as AOD, effective radius, or the Ångström exponent. In addition, chemistry-climate models require surface area densities and particle sizes as input for the heterogeneous chemistry modules. Radiative forcing data sets used within climate model simulations are briefly discussed below, starting with the paleorecords over millennial timescales (section 6.1.1) and then continuing with data sets for the recent decades (section 6.1.2).

6.1.1. Aerosol Forcing Data Sets From Proxy Records

Volcanic forcing reconstructions over millennial timescales are based primarily on volcanic sulfate measured in ice cores [*Gao et al.,* 2008a; *Crowley and Unterman*, 2013]. Under the assumption that sulfate deposition to Greenland and Antarctica varies linearly with stratospheric aerosol loading, volcanic sulfate fluxes derived from ice cores are scaled to stratospheric sulfur injections and loading [*Gao et al.,* 2008a] or directly to AOD [*Crowley and Unterman*, 2013]. In both cases, scaling from ice core sulfate to aerosol properties is based on observations of Pinatubo-derived aerosols. Therefore, the ice core-based data sets show reasonable agreement with observations for recent eruptions. Information regarding sulfur release from past eruptions can also be gained from chemical analysis of tephra [*Scaillet et al.,* 2003]. However, such analyses are necessarily local in scope and show often large differences from ice core-based estimates.

Ice cores provide invaluable information on past volcanism, but the forcing estimates derived from ice cores carry significant uncertainties. For example, due to spatial differences in deposition and transport, ice cores obtained from Antarctica and Greenland produce different estimates of average sulfur flux depending on which cores are used, and dating uncertainties affect the magnitude and timing of volcanic histories from ice cores [*Sigl et al.,* 2014]. Probably, the largest uncertainty in ice core-derived forcing concerns the scaling of surface sulfate deposition to stratospheric aerosol loading and radiative forcing. Modeling studies suggest

that atmospheric variability has a large impact on the relationship between stratospheric sulfur loading and deposition onto the ice sheets [*Toohey et al.,* 2013b]. It is also difficult to determine whether sulfate in ice cores is the result of stratospheric sulfate or tropospheric sulfate, which has a much shorter lifetime and smaller radiative impact. Analysis of the isotopic properties of ice core sulfate promises to help to determine the source altitude of sulfate; however, conclusions based on such isotopic analysis are presently debated [*Lanciki et al.,* 2012; *Schmidt et al.,* 2012].

6.1.2. Aerosol Forcing Data Sets for the Observational Past

For more than three decades and since the launch of the first SAM radiometer, stratospheric aerosol properties have been measured from space (section 4.3). Before satellite measurements, ground-based measurements of solar and stellar extinction are available dating back to around 1883 and have been used to produce stratospheric AOD estimates [*Sato et al.,* 1993; *Stothers*, 2001]. Such data, however, are spatially sparse, especially in the Southern Hemisphere before 1960, and AOD estimates often incorporate geological information concerning the magnitude and location of a volcanic eruption.

The first global two-dimensional reconstruction of aerosol optical parameters was produced by researchers at the Goddard Institute for Space Studies (GISS) [*Sato et al.,* 1993] based on SAGE observations and ground-based pyrometer measurements, supplemented with volcanological information for early eruptions. The data set begins in 1850, and updates extend the record to 2012, with recent years constructed from OSIRIS measurements. Using a combination of SAGE II-derived aerosol extinctions and CLAES-retrieved effective radii, supported by other observational data from the post-Pinatubo period, *Stenchikov et al.* [1998] developed a spectral, space, and time-dependent Pinatubo volcanic aerosol data set, which was later extended to the historical period (1850 to 1999) [e.g., *Schmidt et al.,* 2013]. The volcanic forcing data set of *Ammann et al.* [2003] uses a simple stratospheric transport model to produce self-consistent aerosol spatial patterns for eruptions of the twentieth century, producing higher spatial resolution for eruptions before the satellite era compared to other reconstructions.

As part of the *SPARC* [2006] report, a long-term stratospheric aerosol data set was developed that spanned the period from 1979 to 2002. In recent years, a new aerosol data record of size distributions has been developed for use in the SPARC Chemistry-Climate Model Initiative (CCMI). This "SAGE-4λ" data set has been extended to cover the period from 1960 to 2011: a description of a preliminary version of this data set for the SAGE II period (1984–2005) is available in *Arfeuille et al.* [2013].

SAGE-4λ employs the newest versions of satellite retrievals, which is improved considerably compared to versions used in previous volcanic forcing reconstructions. For the SAGE II time period (1984–2005), the values for aerosol number density, aerosol distribution width, and mode radius were obtained by fitting a log-normal size distribution (with three free parameters) to the extinction data at all available wavelengths, following a similar approach as described in *Bauman et al.* [2003] and [*Bingen et al.,* 2004]. From the size distribution, the radiative properties required to force climate models were calculated using Mie theory. The calculated extinction coefficients at infrared wavelengths (3–12 μm) show good agreement with HALOE and ISAMS data. For periods outside the SAGE II period, there is insufficient information to solve for the lognormal parameters and they are instead inferred from the correlation of the single extinction coefficient value and mode radius and aerosol distribution width with extinction coefficient obtained from the SAGE II period. For the presatellite period 1960–1978, stratospheric aerosol, including the volcanic eruptions Agung and Fuego, was simulated with an aerosol model [*Weisenstein et al.,* 1997] scaled to stellar/solar photometer data at 550 nm.

The continuing impediments in the development of a robust measurement-based long-term stratospheric aerosol climatology include accounting for times and locations for which observations are completely unavailable, the development of a more effective means of combining data from different sources, and expanding beyond conventional limitations in composition (sulfate only) and the use of a single-mode lognormal aerosol size distributions. In situ measurements of stratospheric aerosol often show, even during low aerosol loading, that bimodal or higher-order distributions are more appropriate. There are limited options to improve this via a solely internally derived size distribution. The ability to fill in missing data needs improvement particularly at high latitudes and during the Pinatubo period. The SAGE-4λ data set, as all similar data sets, is based on the assumption that stratospheric aerosol is solely composed of sulfate. This may need to be revisited in the future given improved knowledge of the complexity of composition

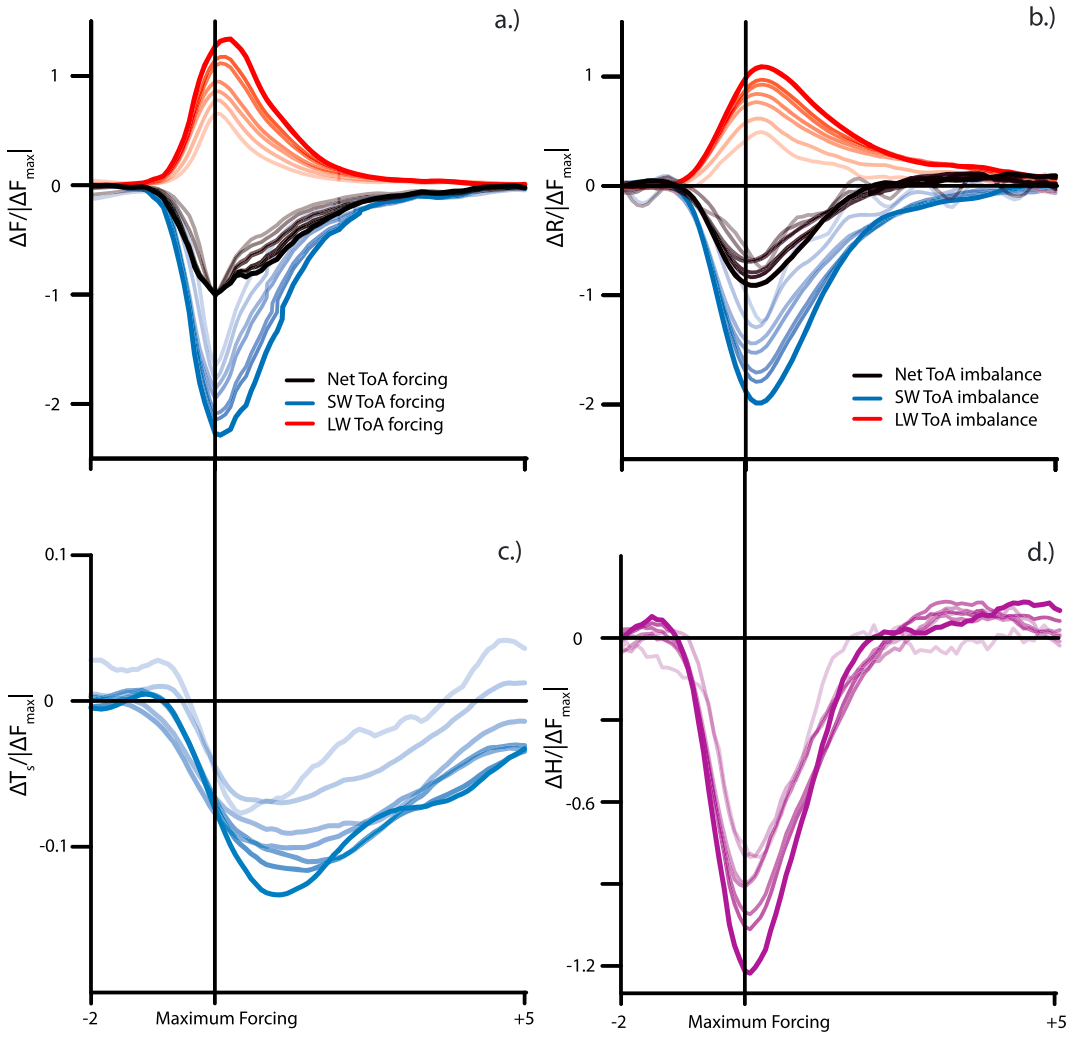

Figure 15. Composite statistics for volcanic eruptions of 10 ensemble simulations of the past millennium [*Jungclaus et al.*, 2010]: (a) composite top-of-atmosphere radiative forcing for several volcanoes (see details below), (b) as for Figure 15a but showing radiative imbalance, (c) as for Figure 15a but showing surface temperature response, and (d) as for Figure 15a but showing ocean heat uptake, H. All quantities were normalized by the maximum forcing of each volcano before the mean of all 10 simulations was calculated. Furthermore, the seasonal cycle was removed from all time series. Color coding indicates the threshold of the minimum forcing for all considered volcanoes. Lightest color considers all volcanoes with a forcing larger than −0.1 W/m^2, and then the threshold increases in steps of 0.5 W/m^2 from −0.5 to −3.0 W/m^2 (Figure is adapted from *Klocke* [2011]).

particularly in the UTLS (e.g., see section 3). Despite these limitations, the SAGE-4λ data set represents the state of the art for a long-term stratospheric aerosol data set for chemistry-climate models and is currently going through further refinement to support the Coupled Model Intercomparison Project Phase 6 (CMIP6) activity.

6.2. Climate Impact of Stratospheric Aerosol

6.2.1. Climate Modeling With Prescribed Stratospheric Aerosol Forcing

Climate model simulations of the Earth's past typically include radiative forcing from stratospheric aerosol, based on direct observations or deduced from proxies (section 6.1.1). For example, CMIP experiments simulating the historical (1850-present) and millennium (1000–2000 Common Era) periods have used reconstructions of stratospheric aerosol. Since the variability of stratospheric aerosol is dominated by volcanic eruptions, most analysis of stratospheric aerosol has focused on the volcanic impact. An increasing number of model studies have been published, which not only accounted for the volcanic impact on temperature and

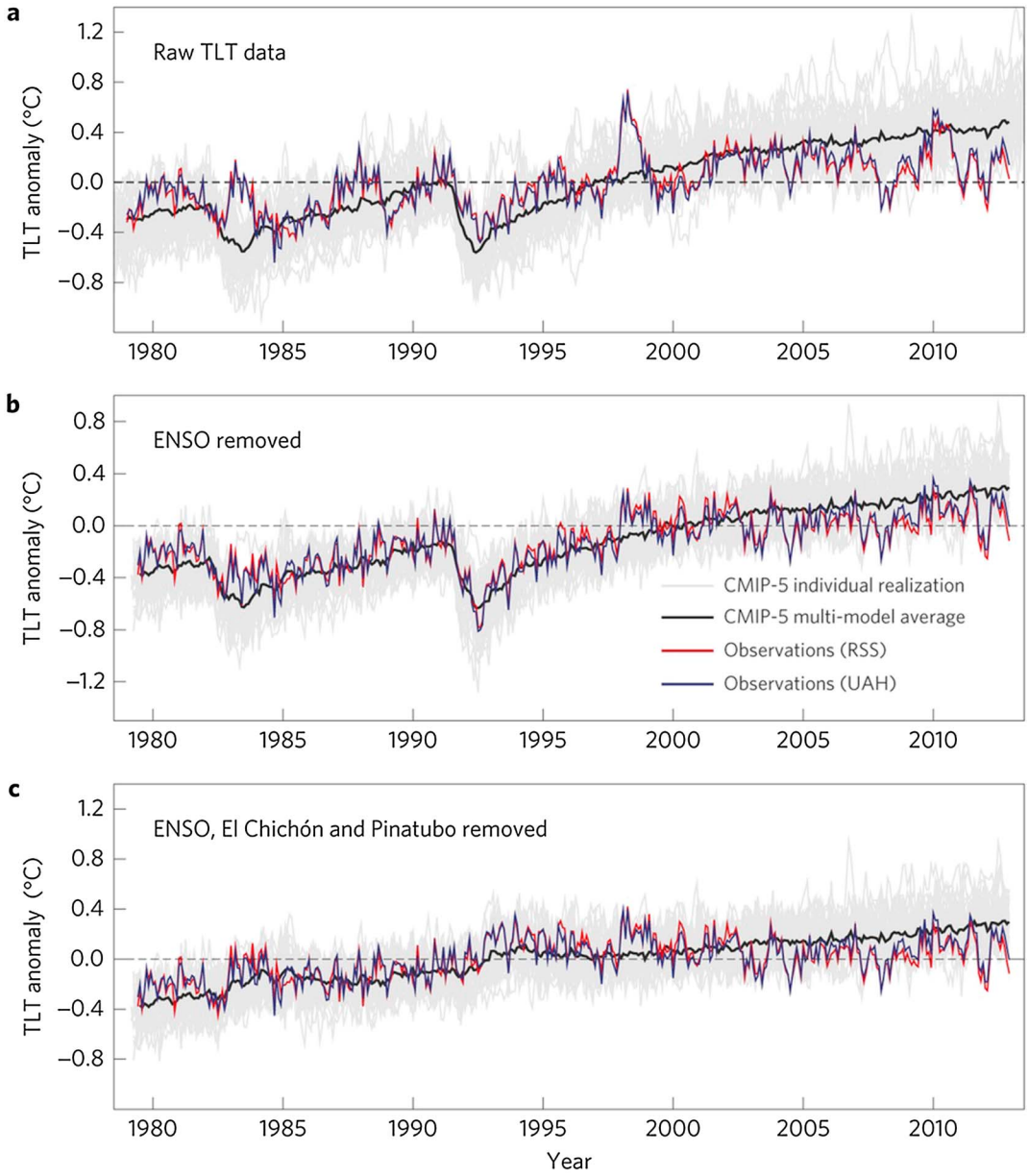

Figure 16. Modeled and observed near-global (82.5°N–70°S) monthly mean temperature anomalies of the lower troposphere (TLT) before and after statistical removal of El Niño–Southern Oscillation (ENSO) and volcano signals. (a) The original TLT anomalies are departures from the climatological monthly means over January 1979–December 2012. (b) Removal of the estimated ENSO signal in TLT reduces the noise that partially obscures the temperature response to the eruptions of El Chichón and Pinatubo. (c) Temperature residuals derived from subtracting the ENSO, El Chichón, and Pinatubo signals from the original TLT data. Figure from *Santer et al.* [2014].

on atmospheric dynamics and composition but also on the hydrological cycle [e.g., *Haywood et al.,* 2013; *Iles et al.,* 2013; *Zhuo et al.,* 2014], ocean heat content and dynamics [e.g., *Stenchikov et al.,* 2009; *Zanchettin et al.,* 2012, 2013], marine and terrestrial biogeochemistry [e.g., *Brovkin et al.,* 2010; *Frölicher et al.,* 2011; *Segschneider et al.,* 2013], and the cryosphere [e.g., *Miller et al.,* 2012; *Berdahl and Robock*, 2013; *Zanchettin et al.,* 2014]. A number of review papers give an overview of the current scientific understanding of volcanic-climate interactions [e.g., *Cole-Dai*, 2010; *Timmreck*, 2012].

Analyzing the relationship between the strength of the volcanic forcing and surface temperatures anomalies in the Max Planck Institute for Meteorology (MPI-M) Earth System Model Millennium ensemble simulations,

Klocke [2011] found that surface temperature response lags the forcing by 12 to 24 months depending on the strength of the forcing (Figure 15). The temperature relaxes back to the equilibrium temperature slower than the radiative flux perturbations decay. The adjustment time and the normalized peak cooling are strongly dependent on the strength of the volcanic eruption, indicating a nonlinear relationship. The ocean dampens the surface temperature anomaly significantly, releasing heat to the atmosphere of the same order of magnitude as that of the radiative forcing (Figure 15).

CMIP5 simulations reveal large uncertainties in the climatic responses to strong volcanic eruptions, such as El Chichón and Mount Pinatubo, with respect to the radiative forcing during periods of strong volcanic activity (Figure 16) [*Santer et al.,* 2014], and tend to overestimate the observed posteruption global surface cooling [*Marotzke and Forster*, 2015]. Further uncertainties are evident in the Northern Hemispheric winter response [*Driscoll et al.,* 2012; *Charlton-Perez et al.,* 2013], the precipitation [*Iles and Hegerl*, 2014], and the ocean response [*Ding et al.,* 2014]. In addition, there is a mismatch between the simulated postvolcanic climate change after very large volcanic eruptions of the last millennium and corresponding reconstructed surface temperature anomalies [*Anchukaitis et al.,* 2012; *D'Arrigo et al.,* 2013; *Mann et al.,* 2013]. In part, the aforementioned differences can be explained as resulting from differences in the model characteristics and feedback processes, but partially they also relate to the treatment of volcanic radiative forcing in the global models [*Timmreck*, 2012]. In general, global climate models do not calculate the aerosol optical properties online but rather prescribe them in various ways and with different aerosol forcing data sets (section 6.1). However, testing the impact of the volcanic aerosols on the dynamical response in Northern Hemispheric winter to different Pinatubo forcing data sets, *Toohey et al.* [2014] found the boreal polar vortex response to be sensitive to the structure of the forcing, which implies a need for an accurate representation of the space and time structure of the volcanic aerosol forcing for the simulation of regional postvolcanic climate changes.

6.2.2. Coupled Aerosol-Climate Modeling

Since the *SPARC* [2006] report has been published, there have been significant improvements in the capacity to model stratospheric aerosol, in particular to simulate aspects of the aerosol properties and to account for interaction between circulation and aerosol evolution. In 2006, only a few global climate models with stratospheric aerosol capability were available to test the quantitative understanding of the processes controlling the formation and evolution of the stratospheric aerosol layer, and the majority was two-dimensional. Since that time, the development and advancement of global three-dimensional stratospheric aerosol models have made significant progress due to the rising interest in improving our understanding of (1) the climate impact of large volcanic eruptions, (2) the effect of proposed climate engineering on chemistry, atmospheric composition and climate, and (3) the impact of the variability of the stratospheric aerosol layer on stratospheric chemistry and climate. Currently, at least 15 global three-dimensional stratospheric aerosol-climate models are active. Those models are summarized in Table A2.

The development of stratospheric aerosol models has been fostered by the recent development of global tropospheric aerosol models in the framework of the "Aerosol Comparisons between Observations and Models" (AeroCOM) project, an international science initiative on aerosol and climate [*Kinne et al.,* 2006; *Textor et al.,* 2006]. Many of the state-of-the-art global three-dimensional chemistry-climate models, with stratospheric aerosol models, calculate not only aerosol microphysical processes online but also account for the aerosol-radiation and/or aerosol-chemistry interactions consistent with simulated global variations in particle size distribution. These models have great potential to reliably simulate the impact of stratospheric aerosol on atmospheric circulation and composition, as well as on radiative forcing and climate.

Different methods are used to incorporate stratospheric aerosol into global circulation models. The mass-only (bulk) approach [*Takigawa et al.,* 2002; *Aquila et al.,* 2012], where the total sulfate mass is a prognostic variable and a typical stratospheric aerosol size distribution is assumed for the calculation of size dependent processes such as sedimentation, coagulation, and radiative anomalies, is the simplest way to calculate the stratospheric aerosol distribution interactively. More sophisticated are size-segregated approaches, two of which are most widely used. One is the modal approach, where one or more lognormal size distributions are applied to prescribe the aerosol size distribution [*Niemeier et al.,* 2009; *Brühl et al.,* 2012], and the other is the sectional or bin model approach [e.g, *English et al.,* 2013], where the particle size distribution is broken

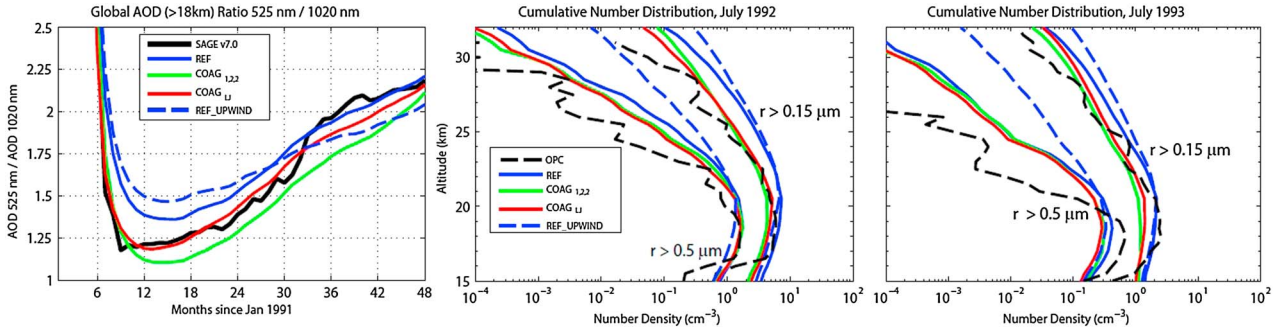

Figure 17. Model-measurement comparison of SAGE II AOD ratios (black line), WOPC in situ measurements (black dashed line), and SOCOL-AER simulations (colors). The blue line represents results from the reference run with standard setup of SOCOL-AER. The experiment $COAG_{1,2,2}$ doubles the coagulation efficiency in transition and free molecular regimes as a simplification of attractive van der Waals forces (green line), and $COAG_{LJ}$ represents the coagulation efficiency as a smooth function of the Knudsen number (red line). The experiment REF_UPWIND employs an upwind method as the sedimentation scheme (dashed blue line). (left) SAGE II and SOCOL-AER modeled global AOD (>18 km) ratios 525 nm/1020 nm. (middle and right) Optical particle counter (OPC) measurements and SOCOL-AER modeled cumulative number distribution for two size channels $r > 0.15$ and $r > 0.5$ µm in July 1991 and July 1992. (Figure is adapted from *Sheng* [2014]).

into size sections (bins). The width and number of the size bins are dependent on the specific model configuration.

To test the reliability of different aerosol microphysical modules (sectional and modal), an intercomparison study was carried out in a box model framework with initial SO_2 concentrations ranging from background to volcanically perturbed conditions [*Kokkola et al.,* 2009]. For very low SO_2 concentrations, all microphysics modules agree in describing the shape of the particle size distribution. However, with increasing initial SO_2 concentrations, the model results start to deviate. Specifically, for the high volcanic SO_2 loading, the aerosol modules need to be modified to properly simulate the temporal evolution of the aerosol size distribution. This agrees with findings of *Weisenstein et al.* [2007], who tested the sensitivity of the simulated aerosol size distribution with respect to the applied aerosol model configuration for three versions of a modal and a sectional model. Their results show that the representation of the aerosol size distribution can have a significant influence on the simulated aerosol decay rates in the aftermath of the Mount Pinatubo eruption.

Aerosol microphysical evolution is very important in controlling the radiative impact of volcanic eruptions. Stratospheric sulfur injection from volcanic eruptions not only increases the sulfate aerosol loading but also changes the aerosol size distribution. Larger aerosol sizes, as observed after the eruption of Pinatubo [*Deshler*, 2008], lead to smaller solar scattering efficiency and shorter stratospheric residence times via enhanced gravitational settling velocities. *Pinto et al.* [1989] indicated with a one-dimensional model that microphysical processes can limit the volcanic impact on climate. Incorporating aerosol size estimates into volcanic forcing time series for climate model simulations leads to climate responses that are not linearly related to the eruption magnitude [*Timmreck et al.,* 2009]. These results have recently been supported by global aerosol model studies [*Timmreck et al.,* 2010; *English et al.,* 2012]. Incorporating aerosol microphysical processes and the corresponding radiative forcing into an Earth System Model leads, for an extremely large volcanic eruption, to a 3 times weaker temperature response compared to assuming a fixed Pinatubo-like aerosol size distribution [*Timmreck et al.,* 2010]. Inaccuracies in the representation of aerosol size distributions in climate model simulations could also be one of the possible explanations for the mismatch between simulated and reconstructed temperature anomalies following large historical eruptions [*Anchukaitis et al.,* 2012]. Furthermore, these inaccuracies could explain, in part, the intermodel differences in the simulated climate forcing estimates [*Mann et al.,* 2015].

Microphysical processes appear to be crucial in determining volcanic impacts on climate and therefore model validations with observational data (in situ, satellite, and paleorecords), and model data intercomparison studies are necessary to better determine the volcanic aerosol radiative forcing [*Timmreck*, 2012]. As a result, a global model intercomparison project on stratospheric sulfur has recently been established. The interactive model intercomparison (ISA-MIP) (http://www.sparc-ssirc.org/) encompasses detailed model

and data intercomparison studies for background and volcanically disturbed conditions. For example, results from a detailed SOCOL-AER model study of the Mount Pinatubo eruption with different microphysical parameterizations in comparison to satellite and in situ observations are shown in Figure 17 [*Sheng*, 2014]. While the use of a sophisticated particle coagulation scheme seems to be of minor importance in the SOCOL-AER model, an accurate sedimentation scheme is essential to prevent particles from sedimenting out of the atmosphere too quickly. Numerical diffusive methods for the sedimentation parameterization can lead to undesirable transport of aerosol to the middle and upper stratosphere [*Benduhn and Lawrence*, 2013].

7. Conclusions

Substantial progress has been made in understanding the sources, processes, and radiative properties of the stratospheric aerosol layer, since the Assessment of Stratospheric Aerosol Properties [*SPARC*, 2006] was completed in 2006. Some of the main advancements are the following:

- *The current estimate of the total net sulfur mass flux from the troposphere into the stratosphere is about 1.5 times larger than the estimate reported in SPARC* [2006]. Recent model simulations by *Sheng et al.* [2015] revealed that the total net sulfur flux from the troposphere into the stratosphere, excluding primary aerosol, is 103 Gg S/yr, and including primary aerosol the flux comes to 181 Gg S/yr. Those numbers are significantly larger than 64 Gg S/yr (excluding primary aerosol) and about 130 Gg S/yr (including primary aerosol) reported in *SPARC* [2006].
- *OCS makes the largest contribution to the aerosol layer, apart from any contribution by volcanoes, as suggested by recent chemistry-climate simulations*. Transport of tropospheric SO_2 to the stratosphere is the second most important contributor to stratospheric aerosol, particularly in the lowermost stratosphere. This is well modeled by chemistry-climate models, and substantial progress has been made toward quantifying the response of relevant biogeochemical processes that produce these gases in a changing climate. The magnitude to which anthropogenic emissions of SO_2 contribute to the stratospheric aerosol loading as well as the preferred input pathway, particularly the degree to which it is reliant on "fast" upward transport, remains uncertain and is subject to debate. SO_2 input from Asia during the monsoon season has been suggested to be of a particular significance because high emissions are coupled to fast upward transport. However, more in situ measurements of SO_2 and detailed transport studies are required and necessary to investigate the preferred input pathway, and to quantify the contribution of SO_2 to the stratospheric aerosol concentrations.
- *There is scientific consensus that minor volcanic eruptions can, on limited timescales, have a nonnegligible impact on stratospheric aerosol, depending on their location and injection height*. Recent observations have demonstrated that injections of SO_2 into the lower stratosphere, even with relatively high-latitude origin, can be transported into the tropical stratosphere, from where it is spread by the Brewer-Dobson Circulation. Further research is required to determine the role of SO_2 injections into the upper troposphere on stratospheric aerosol levels. These events are much harder to characterize remotely than purely stratospheric events like the Kelud eruption which are well separated from clouds and other tropospheric phenomena. As a result, contributions from minor eruptions to the stratospheric sulfur budget are difficult to account for in chemistry-climate models.
- *The large discrepancies in aerosol properties inferred from in situ and space-based measurements during volcanically quiescent conditions have been substantially reduced*. Shortcomings in the analysis of both data sets have been identified and corrected [*Thomason et al.*, 2008; *Kovilakam and Deshler*, 2015], resulting in a substantial improvement in their agreement at all aerosol levels. This is an important development as these data sets form the core set of inputs to climate models that simulate past and future climate.
- *There has been a significant change in both the instruments and techniques for measuring aerosol from space since satellite-based measurements first started, as solar occultation has been replaced with limb and backscatter measurements since the early 2000s*. These changes induce significant challenges to constructing a consistent long-term stratospheric aerosol climatology. While there has been substantial progress made toward this goal, quantifying changes to stratospheric aerosol levels below ±20% is currently not feasible.
- *In the last decade, both the quantity and sophistication of chemistry-climate models have substantially increased*. These models, which are now three-dimensional, have a substantially improved representation

of the transport, sources, and sinks of stratospheric aerosol compared to the climate models that were available for the *SPARC* [2006] report. Furthermore, many models are now coupled to radiation and/or stratospheric chemistry modules to account for relevant feedback processes. While earlier studies focused on the impact of stratospheric aerosol changes on surface temperature, atmospheric composition, and dynamical processes, climate models are now able to account for impacts on the hydrological cycle, ocean heat content, and circulation, as well as changes in the biosphere, the carbon cycle, and the cryosphere. State-of-the-art climate models will be able to simulate the impact of future volcanic eruptions on climate, possibly down to a regional scale.

Despite the progress and advancements achieved over the recent years, important challenges and questions remain:

- *There is significant uncertainty in the role of human-derived SO_2 in changes to stratospheric aerosol levels*. Part of the difficulty to discern human and natural contributions is the impact of regular minor volcanic injections of SO_2 and ash into the lower stratosphere. It is also complicated by the relative dearth of reliable measurements of SO_2 in the tropical UTLS, particularly at the low concentrations required ($<$10 ppt). Improved observational capabilities are required to quantify the role of human activity on stratospheric aerosol levels.
- *While there is a developing understanding of the role that nonsulfate compounds play in stratospheric aerosol morphology, there is currently limited ability to account for their effects in chemistry-climate models*. About 50% of all aerosols contain nonsulfate cores of diverse origin, and above approximately 35 km, where the sulfate component evaporates, essentially all aerosols are either the nonrefractory remnant or meteoritic dust subsiding from higher altitudes. The role of nonsulfate aerosol, particularly in the lower stratosphere, is most likely small but not negligible. These nonsulfate contributions to the stratospheric aerosol are not accounted for in most chemistry-climate models to date, but they could play an important role in heterogeneous chemical reactions and for the nucleation/condensation of saturated gaseous compounds.
- *The outlook of space-based measurements of stratospheric aerosol beyond 2020 is uncertain*. The short-term prospects for global space-based aerosol measurements are excellent with observations from OSIRIS and CALIPSO expected to last several more years and the potential for an Ozone Mapping Profiler Suite stratospheric aerosol product [*Gorkavyi et al.,* 2013]. Furthermore, a new SAGE mission is expected to begin in 2016. However, the future of space-based measurements beyond 2020 is uncertain. It is critical to maintain a continuous observational record to detect unpredictable (i.e., large volcanic events) or unexpected (i.e., changes in stratospheric aerosol levels caused by nonvolcanic processes) developments. Observations remain a critical element to testing the reliability of climate model results.
- *It is not clear that current models have the full capability to simulate either the impact of smaller events, similar to those of the past decade, or mega-events such as the Toba eruption of about 73,5000 years ago, or a cataclysmic eruption of the Yellowstone super volcano*. While the simulation of the impact of smaller eruptions is highly desirable, the latter, while of academic interest, could have outcomes so severe, that forecasts could be irrelevant.
- *The stratospheric aerosol layer is still prescribed in many climate models, and as a result, future climate model simulations cannot account for interactions between the sulfur cycle and changes in climate*. Therefore, one of the goals of the climate model community is to include the sulfur/aerosol system as an interactive module in global climate models to assess its role in climate variability. A number of international activities which focus on the uncertainties in aerosol microphysical modeling such as ISA-MIP (http://www.sparc-ssirc.org/), on the climate response of volcanic forcing such as VolMIP (http://volmip.org/), and on geoengineered stratospheric aerosol such as GeoMIP (http://climate.envsci.rutgers.edu/GeoMIP/links.html), as well as on the link between volcanic forcing, climate, and society such as the Volcanic Impacts on Climate and Society initiative (http://www.pages-igbp.org/ini/wg/vics/intro) are currently underway. These activities promise to improve climate models, and the prospects for additional progress are highly favorable.

Appendix A

Table A1 provides a summary of stratospheric aerosol measurements obtained from different measurement platforms. Table A2 gives an overview about the current active stratospheric aerosol-climate models, and Table A3 summarizes all acronyms that were used within this review.

Reviews of Geophysics

10.1002/2015RG000511

Table A1. Summary of Stratospheric Aerosol Measurements Obtained From Different Measurement Platforms and Completed Within 30° Latitude Bands

Property	Instrument	Altitude Limitation	60°–90°N	30°–60°N	0°–30°N	0°–30°S	30°–60°S	60°–90°S
			Satellite-Borne					
Extinction	SAGE II		1985–2005	1985–2005	1985–2005	1985–2005	1985–2005	1985–2005
	SAGE III		2002–2005				2002–2005	
	GOMOS		2002–2012	2002–2012	2002–2012	2000–2012	2002–2012	2002–2012
	OSIRIS[a]		2001–2015	2001–2015	2001–2015	2001–2015	2001–2015	2001–2015
			Aircraft-Borne					
Size distribution	CARIBIC	tropopause +4 km	1997–2002,	1997–2002,	1997–2002,	2005–2015		
	OPSS and CPCs[a]		2005–2015	2005–2015	2005–2015			
	FCAS[a]	< 21 km	1989–2003	1987–2013	1987–2013			
Composition	PALMS[a]	< 21 km		1998–2000, 2002	1998–2000, 2002			
	CARIBIC	tropopause +4 km	1999–2002,	1999–2002,	1999–2002,	2005–2015		
	impactor sampler[a]		2005–2015	2005–2015	2005–2015			
			Balloon-Borne					
Size distribution	UWOPC[a]	< 32 km	1991–2004	1971–2015			1991–2001	1989–2010
			Ground-Based Lidar					
Backscatter	Ny Alesund[a]		1991–2015					
	Garmisch[a], Germany			1977–2015				
	Hampton, USA			1974–2002				
	Haute Provence[a], France			1991–2015				
	Boulder, USA			1999–2009				
	Table Mountain[a], USA			1989–2015				
	Mauna Loa[a], Hawaii				1993–2015			
	Mauna Loa[a], NOAA, Hawaii				1975–2015			
	Sao Jose dos Campos, Brazil					1975–2007		
	Lauder, New Zealand						1992–2008	
	Dumont d'Urville[a], Antarctica							1992–2014
	McMurdo, Antarctica							1991–2010

[a]Instruments are still active.

AGU Reviews of Geophysics

10.1002/2015RG000511

Table A2. Overview of Global Three-Dimensional Stratospheric Aerosol Models

Model	Type	Horizontal Resolution (Lat × Lon)	Vertical Resolution (Model Top, Model Levels, Total Lev. Above Tropopause)	Stratospheric Compounds[a]	Size Distribution	Het. Chem.	Radiation	References
CAM5/CARMA	CCM	1.9° × 2.5°	1.8 hPa 56 (21) levels	sulfate, meteoric dust, organics	sectional, 20 size bins	Y	Y	*Yu et al.* [2015]
CCSR/NIES	AGCM	5.6° × 5.6° (T21)	70 km 32 (20) levels	sulfate	modal, 1 mode	Y	Y	*Takigawa et al.* [2002]
CESM(WACCM)	CCM	1.9° × 2.5°	4.5×10^{-6} hPa 70 (48) levels[b]	sulfate, PSC[c], organics	modal, 3 modes	Y	Y	*Mills et al.* [2016]
ECHAM5-HAM-SALSA	AGCM	1.9° × 1.9° (T63)	0.01 hPa 47 (24) levels	sulfate	sectional, 17 size bins	N	Y	*Bergman et al.* [2012b] *Laakso et al.* [2012]
EMAC	AGCM	2.8° × 2.8° (T42)	0.01 hPa 90 (63) levels	sulfate, organics, dust, black carbon, PSC	modal, 7 modes	Y	Y	*Brühl et al.* [2012] and *Brühl et al.* [2015]
GEOS-5/CARMA	CCM	2° × 2.5°	0.01 hPa 72 (40) levels	sulfate	sectional, 22 size bins	Y	Y	Colarco, personal communication, 2015
GEOS-5/GOCART	CCM	2° × ° 2.5°	0.01 hPa 72 (40) levels	sulfate	modal, 1 mode	Y	Y	*Aquila et al.* [2013]
GISS ModelE2 + MATRIX	GCM	2.0° × 2.5°	0.1 hPa 40 (15) levels	sulfate, PSC	modal, 16 modes	Y[d]	Y	*Bauer et al.* [2008]
MAECHAM5-HAM	AGCM	2.8° × 2.8° (T42)	0.01 hPa 39 (24) levels	sulfate	modal, 7 modes	N	Y	*Niemeier et al.* [2009] and *Toohey et al.* [2013b]
MAECHAM5.5-HAM2	AGCM	1.9° × 1.9° (T63)	0.01 hPa, 47 (24) levels	sulfate	modal, 7 modes	N	Y	*Laakso et al.* [2012]
MAECHAM5-SAM2	AGCM	2.8° × 2.8° (T42)	0.01 hPa47 (24) levels	sulfate	sectional, 35 size bins	N	N	*Hommel et al.* [2011]
MRI-ESM1	ESM	1.6° × 1.6° (TL95)[e]	0.01 hPa 48 (21) levels	sulfate	modal, 1 mode	Y	Y	*Yukimoto et al.* [2011] and *Tanaka et al.* [2003]
SOCOL-AER	CCM	3.75° × 3.75° (T31)	0.01 hPa 39 (15) levels[f]	sulfate, PSC	sectional, 40 size bins	Y	Y	*Sheng et al.* [2015]
TM5	CTM	2° × 3°	0.01 hPa 60 (24–34) levels	sulfate	modal, 7 modes	Y	N	*Bânda et al.* [2015] and *van Noije et al.* [2014]
ULAQ_CCM	CCM	5° × 6°	0.04 hPa 126 (98) levels	sulfate, PSC	sectional, 15 size bins	Y	Y	*Pitari et al.* [2014]
UKESM-LO (incl.UKCA-GLOMAP)	CCM	1.25° × 1.875° (N96)	84 km 85 levels	sulfate, organics, meteoric dust, PSC[j]	modal, 7 modes	Y	Y	*Morgenstern et al.* [2009] and *Dhomse et al.* [2014]
CESM(WACCM)-CARMA[h]	CCM	1.9° × 2.5°	4.5×10^{-6} hPa 88 (54) levels[g]	sulfate	sectional, 30 size bins	Y	N	*Campbell et al.* [2014]
CESM(WACCM)-CARMA	CCM	1.9° × 2.5°	4.5×10^{-6} hPa, 88 (54) levels[g]	sulfate, PSCs	sectional, 20 size bins	Y	N	*Zhu et al.* [2015]
MIROC-CHASER/SPRINT AS	CCM	2.8° × 2.8° (T42)	52 km, 57 (24) levels[i]	sulfate, fine volcanic ash	modal 3 modes	Y	Y	[*Sekiya et al.*, 2016]

[a]Sulfate PSC, meteoric dust, organic compounds.
[b]88 (54) levels when nudged with specified dynamics.
[c]PSC treatment includes Supersaturated Ternary Solution (STS), Nitric Acid Trihydrate (NAT), and water ice. Sedimentation of PSC particles is included in the model.
[d]N_2O_5 hydration on aerosols.
[e]Reference to the aerosol part of model—other atmospheric model components are the atmospheric general circulation model (AGCM) with 1.1° × 1.1° (TL159) and the chemical in 2.8° × 2.8° (T42).
[f]Model is also used with 90 levels.
[g]66 (48) levels when free running.
[h]Previous version is WACCM3-CARMA [e.g., *English et al.*, 2013].
[i]24 vertical levels above the tropopause over the tropics and 41 levels over the middle-high latitudes.
[j]NAT-PSCs are assumed to be in equilibrium with gas phase HNO_3. Sedimentation of PSC particles is included in the model.

Table A3. Acronyms as Used in This Paper (Ordered Alphabetically)

Acronym	Definition
ACE-FTS	Atmospheric Chemistry Experiment-Fourier Transform Spectrometer
AER model	Atmospheric and Environmental Research model
AeroCOM	Aerosol Comparisons between Observations and Models
ATAL	Asian Tropopause Aerosol Layer
ATLAS	Atmospheric Laboratory for Applications and Science
ATMOS	Atmospheric Trace Molecule Spectroscopy Experiment
AOD	Aerosol Optical Depth
BB	Biomass burning
BC	Black carbon
BDC	Brewer-Dobson Circulation
CALIOP	Cloud-Aerosol with Orthogonal Polarization Lidar
CALIPSO	Cloud-Aerosol Lidar and Infrared Pathfinder Satellite Observation
CMIP5/6	Coupled Model Intercomparison Project Phase 5/6
CARIBIC	Civil Aircraft for Regular Investigation of the atmosphere Based on an Instrument Container
CCMI	SPARC Chemistry Climate Model Initiative
CLAES	Cryogenic Limb Emission Spectrometer
CN	Condensation Nuclei
DCPP	Decadal Climate Prediction Panel
FCAS	Focused Cavity Aerosol Spectrometer
FTIR	Fourier Transform Infrared spectrometers
GISS	Goddard Institute for Space Studies
GOME-2	Global Ozone Monitoring Experiment-2
GOMOS	Global Ozone Monitoring by Occultation of Stars
HALOE	Halogen Occultation Experiment
IASI	Infrared Atmospheric Sounding Interferometer
ISAMS	Improved Stratospheric and Mesospheric Sounder
LCP	Lagrangian Cold Point
MIPAS	Michelson Interferometer for Passive Atmospheric Sounding
MPI-M	Max Planck Institute for Meteorology
MSP	Meteoric Smoke Particles
NATAL	North American Tropopause Aerosol Layer
NDACC	Network for the Detection of Atmospheric Composition Change
NMASS	Nucleation-Mode Aerosol Size Spectrometer
OC	Organic carbon
OMI	Ozone Monitoring Instrument
OPC	Optical Particle Counter
OSIRIS	Optical Spectrograph and InfraRed Imaging System
POAM	Polar Ozone and Aerosol Measurement
ppt	Parts per trillion, 10^{-12}
PSC	Polar Stratospheric Cloud
PyroCb	Pyrocumulonimbus
QBO	Quasi-Biennial Oscillation
SAM	Stratospheric Aerosol Measurement
SAD	Surface Area Density
SAGE II	Stratospheric Aerosol and Gas Experiment
SEM	Scanning Electron Microscopy
SSiRC	Stratospheric Sulfur and its Role in Climate
ISA-MIP	Interactive mode intercomparison project
SPARC	Stratosphere-troposphere Processes and their Role in Climate
TES	Tropospheric Emission Spectrometer
TOMS	Total Ozone Mapping Spectrometer
TOVS	TIROS (Television InfraredObservation Satellite) Observational Vertical Sounder
TTL	Tropical Tropopause Layer
UARS-MLS	Upper Atmosphere Research Satellite-Microwave Limb Sounder
UTLS	Upper Troposphere/Lower Stratosphere
UV	ultraviolet
VEI	Volcanic Explosivity Index
VolMIP	Model Intercomparison Project on the climate response to Volcanic forcing
WCB	Warm Conveyor Belts
WOPC	Wyoming's balloon-borne optical particle counters

Acknowledgments

We would like to thank Thomas Peter, Stephan Borrmann, and Beiping Luo for the many very helpful discussions and suggestions. We would like to thank Aimee V. Amin, SSAI (Hampton, VA, USA) for the design of Figure 1, Michael Höpfner for providing Figure 6, Horst Jäger for his assistance in generating underlying data files for parts of Figure 10/Figure 12, and Steven Smith for providing the anthropogenic sulfur emissions data for Figure 14. The authors thank the International Space Science Institute (ISSI, Bern, Switzerland) through their support of the SSiRC science team that made this publication possible. We would like to thank SPARC for their support of the SSiRC activity. L. Clarisse is a research associate with the F.N.R.S. S. Kremser would like to thank the Royal Society of New Zealand for support through the Marsden Fast-Start fund. J.M.C. Plane and A.D. James are supported by a grant from the European Research Council (project 291332-CODITA). C. Timmreck and M. Toohey acknowledge support from the German federal Ministry of Education (BMBF), research program "MiKlip" (FKZ:01LP130A(CT):/01LP1130B (MT)). R. Weigel and M. v. Hobe are supported by SPITFIRE which is funded by the German BMBF under the ROMIC (ROle of the MIddle atmosphere in Climate) programme. Work on this review was partly supported by the European Union Seventh Framework Programme (FP7/2007–2013) under grant agreement 603557. The data presented in this study are listed in the provided references. Requests for data used in this paper can be directed to S. Kremser (stefanie@bodekerscientific.com).

References

Abalos, M., F. Ploeger, P. Konopka, W. J. Randel, and E. Serrano (2013), Ozone seasonality above the tropical tropopause: Reconciling the Eulerian and Lagrangian perspectives of transport processes, *Atmos. Chem. Phys.*, *13*(21), 10,787–10,794, doi:10.5194/acp-13-10787-2013.

Albu, M., I. Barnes, K. H. Becker, I. Patroescu-Klotz, T. Benter, and R. Mocanu (2008), Ft-Ir product study on the OH radical initiated oxidation of dimethyl sulfide: Temperature and O(2) partial pressure dependence, in *Simulation and Assessment of Chemical Processes in a Multiphase Environment*, edited by I. Barnes and M. M. Kharytonov, pp. 501–513, Springer, Dordrecht.

Ammann, C. M., G. A. Meehl, W. M. Washington, and C. S. Zender (2003), A monthly and latitudinally varying volcanic forcing dataset in simulations of 20th century climate, *Geophys. Res. Lett.*, *30*(12), 1657, doi:10.1029/2003GL016875.

Amyx, K., Z. Sternovsky, S. Knappmiller, S. Robertson, M. Horanyi, and J. Gumbel (2008), In-situ measurement of smoke particles in the wintertime polar mesosphere between 80 and 85 km altitude, *J. Atmos. Sol. Terr. Phys.*, *70*(1), 61–70, doi:10.1016/j.jastp.2007.09.013.

Anchukaitis, K. J., et al. (2012), Tree rings and volcanic cooling, *Nat. Geosci. Corr.*, *5*, 836–837, doi:10.1038/ngeo1645.

Andersson, S. M., B. G. Martinsson, J. Friberg, C. A. M. Brenninkmeijer, A. Rauthe-schöch, M. Hermann, P. F. J. van Velthoven, and A. Zahn (2013), Composition and evolution of volcanic aerosol from eruptions of Kasatochi, Sarychev and Eyjafjallajökull in 2008–2010 based on CARIBIC observations, *Atmos. Chem. Phys.*, *13*, 1781–1796, doi:10.5194/acp-13-1781-2013.

Ansmann, A., M. Riebesell, U. Wandinger, C. Weitkamp, E. Voss, W. Lahmann, and W. Michaelis (1992), Combined raman elastic-backscatter LIDAR for vertical profiling of moisture, aerosol extinction, backscatter, and LIDAR ratio, *Appl. Phys. B*, *55*(1), 18–28.

Antuña, J. C., A. Robock, G. L. Stenchikov, L. W. Thomason, and J. E. Barnes (2002), Lidar validation of SAGE II aerosol measurements after the 1991 Mount Pinatubo eruption, *J. Geophys. Res.*, *104*(D14), 4194, doi:10.1029/2001JD001441.

Antuña, J. C., A. Robock, G. Stenchikov, J. Zhou, C. David, J. Barnes, and L. Thomason (2003), Spatial and temporal variability of the stratospheric aerosol cloud produced by the 1991 Mount Pinatubo eruption, *J. Geophys. Res.*, *108*(D20), 4624, doi:10.1029/2003JD003722.

Aquila, V., L. D. Oman, R. S. Stolarski, P. R. Colarco, and P. A. Newman (2012), Dispersion of the volcanic sulfate cloud from a Mount Pinatubo-like eruption, *J. Geophys. Res.*, *117*, D06216, doi:10.1029/2011JD016968.

Aquila, V., L. D. Oman, R. Stolarski, A. R. Douglass, and P. A. Newman (2013), The response of ozone and nitrogen dioxide to the eruption of Mt. Pinatubo at southern and northern midlatitudes, *J. Atmos. Sci.*, *70*(3), 894–900, doi:10.1175/JAS-D-12-0143.1.

Arfeuille, F., B. P. Luo, P. Heckendorn, D. Weisenstein, J. X. Sheng, E. Rozanov, M. Schraner, S. Brönnimann, L. W. Thomason, and T. Peter (2013), Modeling the stratospheric warming following the Mt. Pinatubo eruption: Uncertainties in aerosol extinctions, *Atmos. Chem. Phys.*, *13*, 11,221–11,234, doi:10.5194/acp-13-11221-2013.

Arnold, F., J. Schneider, K. Gollinger, H. Schlager, P. Schulte, D. Hagen, P. Whitefield, and P. van Velthoven (1997), Observation of upper tropospheric sulfur dioxide- and acetone-pollution: Potential implications for hydroxyl radical and aerosol formation, *Geophys. Res. Lett.*, *24*, 57–60, doi:10.1029/96GL03693.

Aschmann, J., B.-M. Sinnhuber, M. P. Chipperfield, and R. Hossaini (2011), Impact of deep convection and dehydration on bromine loading in the upper troposphere and lower stratosphere, *Atmos. Chem. Phys.*, *11*, 2671–2687, doi:10.5194/acp-11-2671-2011.

Aydin, M., M. B. Williams, C. Tatum, and E. S. Saltzman (2008), Carbonyl sulfide in air extracted from a South Pole ice core: A 2000 year record, *Atmos. Chem. Phys.*, *8*(24), 7533–7542.

Aydin, M., T. J. Fudge, K. R. Verhulst, M. R. Nicewonger, E. D. Waddington, and E. S. Saltzman (2014), Carbonyl sulfide hydrolysis in Antarctic ice cores and an atmospheric history for the last 8000 years, *J. Geophys. Res. Atmos.*, *119*, 8500–8514, doi:10.1002/2014JD021618.

Baldwin, M. P., et al. (2001), The Quasi-Biennial Oscillation, *Rev. Geophys.*, *39*(2), 179–229, doi:10.1029/1999RG000073.

Bånda, N., M. Krol, T. van Noije, M. van Weele, J. E. Williams, P. L. Sager, U. Niemeier, L. Thomason, and T. Röckmann (2015), The effect of stratospheric sulfur from Mount Pinatubo on tropospheric oxidizing capacity and methane, *J. Geophys. Res. Atmos.*, *120*, 1202–1220, doi:10.1002/2014JD022137.

Baran, A. J., and J. S. Foot (1994), New application of the operational sounder HIRS in determining a climatology of sulphuric acid aerosol from the Pinatubo eruption, *J. Geophys. Res.*, *99*(D), 25,673–25,679, doi:10.1029/94JD02044.

Bardeen, C. G., O. B. Toon, E. J. Jensen, D. R. Marsh, and V. L. Harvey (2008), Numerical simulations of the three-dimensional distribution of meteoric dust in the mesosphere and upper stratosphere, *J. Geophys. Res.*, *113*, D17202, doi:10.1029/2007JD009515.

Barkley, M. P., P. I. Palmer, C. D. Boone, P. F. Bernath, and P. Suntharalingam (2008), Global distributions of carbonyl sulfide in the upper troposphere and stratosphere, *Geophys. Res. Lett.*, *35*, L14810, doi:10.1029/2008GL034270.

Barnes, I., K. H. Becker, and N. Mihalopoulos (1994), An FTIR product study of the photooxidation of dimethyl disulfide, *J. Atmos. Chem.*, *18*(3), 267–289.

Bauer, S. E., D. L. Wright, D. Koch, E. R. Lewis, R. Mcgraw, L.-S. Chang, S. E. Schwartz, and R. Ruedy (2008), MATRIX (Multiconfiguration Aerosol TRacker of mIXing state): An aerosol microphysical module for global atmospheric models, *Atmos. Chem. Phys.*, *8*, 6003–6035, doi:10.5194/acp-8-6003-2008.

Bauman, J. J., P. B. Russel, M. A. Geller, and P. Hamill (2003), A stratospheric aerosol climatology from SAGE II and CLAES measurements: 1. Methodology, *J. Geophys. Res.*, *108*(D13), 4382, doi:10.1029/2002JD002992.

Baumann, R., and H. Schlager (2012), Lagrangian modeling of transport and dispersion of air constituents, in *Atmospheric Physics: Background-Methods-Trends*, edited by U. Schumann, pp. 381–399, Springer, Heidelberg, New York, doi:10.1007/978-3-642-30183-4_23.

Beirle, S., C. Hoermann, M. P. de Vries, S. Doerner, C. Kern, and T. Wagner (2014), Estimating the volcanic emission rate and atmospheric lifetime of SO2 from space: A case study for Kilauea volcano, Hawaii, *Atmos. Chem. Phys.*, *14*(16), 8309–8322, doi:10.5194/acp-14-8309-2014.

Benduhn, F., and M. G. Lawrence (2013), An investigation of the role of sedimentation for stratospheric solar radiation management, *J. Geophys. Res. Atmos.*, *118*, 7905–7921, doi:10.1002/jgrd.50622.

Berdahl, M., and A. Robock (2013), Northern Hemispheric cryosphere response to volcanic eruptions in the Paleoclimate Modeling Intercomparison Project 3 last millennium simulations, *J. Geophys. Res. Atmos.*, *118*, 12,359–12,370, doi:10.1002/2013JD019914.

Bergman, J. W., E. J. Jensen, L. Pfister, and Q. Yang (2012a), Seasonal differences of vertical-transport efficiency in the tropical tropopause layer: On the interplay between tropical deep convection, large-scale vertical ascent, and horizontal circulations, *J. Geophys. Res.*, *117*, D05302, doi:10.1029/2011JD016992.

Bergman, T., V.-M. Kerminen, H. Korhonen, K. J. Lehtinen, R. Makkonen, A. Arola, T. Mielonen, S. Romakkaniemi, M. Kulmala, and H. Kokkola (2012b), Evaluation of the sectional aerosol microphysics module SALSA implementation in ECHAM5-HAM aerosol-climate model, *Geosci. Model Dev.*, *5*, 845–868, doi:10.5194/gmd-5-845-2012.

Berry, J., et al. (2013), A coupled model of the global cycles of carbonyl sulfide and CO_2: A possible new window on the carbon cycle, *J. Geophys. Res. Biogeosci.*, *118*, 842–852, doi:10.1002/jgrg.20068.

Bertrand, C., N. Clerbaux, A. Ipe, and L. Gonzalez (2003), Estimation of the 2002 Mount Etna eruption cloud radiative forcing from Meteosat-7 data, *Remote Sens. Environ.*, *87*, 257–272.
Bigg, E. K. (2012), Sources of insoluble inclusions in stratospheric sulfate particles, *Meteorit. Planet. Sci.*, *47*(5), 799–805, doi:10.1111/j.1945-5100.2012.01346.x.
Bigg, E. K., A. Ono, and W. J. Thompson (1970), Aerosols at altitudes between 20 and 37 km, *Tellus*, *22*(5), 550–563, doi:10.1111/j.2153-3490.1970.tb00522.x.
Bingen, C., D. Fussen, and F. Vanhellemont (2004), A global climatology of stratospheric aerosol size distribution parameters derived from SAGE II data over the period 1894-2000: 1. Methodology and climatological observations, *J. Geophys. Res.*, *109*, D06201, doi:10.1029/2003JD003518.
Blake, D. F., and K. Kato (1995), Latitudinal distribution of black carbon soot in the upper troposphere and lower stratosphere, *J. Geophys. Res.*, *100*, 7195–7202, doi:10.1029/94JD03118.
Bond, T. C., et al. (2013), Bounding the role of black carbon in the climate system: A scientific assessment, *J. Geophys. Res. Atmos*, *118*, 5380–5552, doi:10.1002/jgrd.50171.
Borrmann, S., et al. (2010), Aerosols in the tropical and subtropical UT/LS: In-situ measurements of submicron particle abundance and volatility, *Atmos. Chem. Phys.*, *10*(12), 5573–5592, doi:10.5194/acp-10-5573-2010.
Bourassa, A. E., D. A. Degenstein, R. L. Gattinger, and E. J. Llewellyn (2007), Stratospheric aerosol retrieval with optical spectrograph and infrared imaging system limb scatter measurements, *J. Geophys. Res.*, *112*, D10217, doi:10.1029/2006JD008079.
Bourassa, A. E., L. A. Rieger, N. D. Lloyd, and D. A. Degenstein (2012a), Odin-OSIRIS stratospheric aerosol data product and SAGE III intercomparison, *Atmos. Chem. Phys.*, *12*, 605–614, doi:10.5194/acp-12-605-2012.
Bourassa, A. E., A. Robock, W. J. Randel, T. Deshler, L. A. Rieger, N. D. Lloyd, E. J. Llewellyn, and D. A. Degenstein (2012b), Large volcanic aerosol load in the stratosphere linked to Asian monsoon transport, *Science*, *337*, 78–81, doi:10.1126/science.1219371.
Brock, C. A., P. Hamill, J. C. Wilson, H. H. Jonsson, and K. R. Chan (1995), Particle formation in the upper tropical troposphere: A source of nuclei for the stratospheric aerosol, *Science*, *270*(5242), 1650–1653, doi:10.2307/2887916.
Brock, C. A., F. Schröder, B. Kärcher, A. Petzold, R. Busen, and M. Fiebig (2000), Ultrafine particle size distributions measured in aircraft exhaust plumes, *J. Geophys. Res.*, *105*(D21), 26,555–26,567, doi:10.1029/2000JD900360.
Brovkin, V., S. J. Lorenz, J. Jungclaus, T. Raddatz, C. Timmreck, C. H. Reick, J. Segschneider, and K. Six (2010), Sensitivity of a coupled climate-carbon cycle model to large volcanic eruptions during the last millennium, *Tellus B*, *62*(5), 674–681, doi:10.1111/j.1600-0889.2010.00471.x.
Brühl, C., J. Lelieveld, P. J. Crutzen, and H. Tost (2012), The role of carbonyl sulphide as a source of stratospheric sulphate aerosol and its impact on climate, *Atmos. Chem. Phys.*, *12*, 1239–1253, doi:10.5194/acp-12-1239-2012.
Brühl, C., J. Lelieveld, H. Tost, M. Höpfner, and N. Glatthor (2015), Stratospheric sulphur and its implications for radiative forcing simulated by the chemistry climate model EMAC, *J. Geophys. Res. Atmos.*, *120*, 2103–2118, doi:10.1002/2014JD022430.
Burkholder, J., M. Mills, and S. McKeen (2000), Upper limit for the UV absorption cross sections of H_2SO_4, *Geophys. Res. Lett.*, *27*, 2493–2496, doi:10.1029/1999GL011271.
Butchart, N. (2014), The Brewer-Dobson circulation, *Rev. Geophys.*, *52*, 157–184, doi:10.1002/2013RG000448.
Cameron-Smith, P., S. Elliott, M. Maltrud, D. Erickson, and O. Wingenter (2011), Changes in dimethyl sulfide oceanic distribution due to climate change, *Geophys. Res. Lett.*, *38*, L07704, doi:10.1029/2011GL047069.
Campbell, J. E., et al. (2008), Photosynthetic control of atmospheric carbonyl sulfide during the growing season, *Science*, *322*(5904), 1085–1088.
Campbell, J. E., M. E. Whelan, U. Seibt, S. J. Smith, J. A. Berry, and T. W. Hilton (2015), Atmospheric carbonyl sulfide sources from anthropogenic activity: Implications for carbon cycle constraints, *Geophys. Res. Lett.*, *42*, 3004–3010, doi:10.1002/2015GL063445.
Campbell, P., and T. Deshler (2014), Condensation nuclei measurements in the midlatitude (1982–2012) and Antarctic (1986–2010) stratosphere between 20 and 35 km, *J. Geophys. Res. Atmos.*, *119*, 137–152, doi:10.1002/2013JD019710.
Campbell, P., M. Mills, and T. Deshler (2014), The global extent of the mid stratospheric CN layer: A three-dimensional modelling study, *J. Geophys. Res. Atmos.*, *119*, 1015–1030, doi:10.1002/2013JD020503.
Carboni, E., R. G. Grainger, T. A. Mather, D. M. Pyle, G. E. Thomas, R. Siddans, A. J. A. Smith, A. Dudhia, M. E. Koukouli, and D. Balis (2016), The vertical distribution of volcanic SO_2 plumes measured by IASI, *Atmos. Chem. Phys.*, *16*, 4343–4367, doi:10.5194/acp-16-4343-2016.
Carn, S., and T. M. Lopez (2011), Opportunistic validation of sulfur dioxide in the Sarychev Peak volcanic eruption cloud, *Atmos. Meas. Tech.*, *4*, 1705–1712, doi:10.5194/amt-4-1705-2011.
Carn, S., L. Clarisse, and A. J. Prata (2016), Multi-decadal satellite measurements of global volcanic degassing, *J. Volcanol. Geotherm. Res.*, 99–134, doi:10.1016/j.jvolgeores.2016.01.002.
Carn, S. A., and F. J. Prata (2010), Satellite-based constraints on explosive SO_2 release from Soufrière Hills Volcano, Montserrat, *Geophys. Res. Lett.*, *37*, L00E22, doi:10.1029/2010GL044971.
Carn, S. A., et al. (2011), In situ measurements of tropospheric volcanic plumes in Ecuador and Colombia during TC4, *Geophys. Res. Lett.*, *116*, D00J24, doi:10.1029/2010JD014718.
Cess, R. D., et al. (1993), Uncertainties in carbon dioxide radiative forcing in atmospheric general circulation models, *Science*, *262*, 1252–1255, doi:10.1126/science.262.5137.1252.
Chagnon, C. W., and C. E. Junge (1961), The vertical distribution of sub-micron particles in the stratosphere, *J. Meteorol.*, *18*, 746–752.
Chang, H.-Y. A., T. Koop, L. T. Molina, and M. J. Molina (1999), Phase transitions in emulsified HNO3/H2O and HNO3/H2SO4/H2O solutions, *J. Phys. Chem. A*, *103*(15), 2673–2679, doi:10.1021/jp9841034.
Charlton-Perez, A., et al. (2013), On the lack of stratospheric dynamical variability in low-top versions of the CMIP5 models, *J. Geophys. Res. Atmos.*, *118*, 24,94–25,052, doi:10.1002/jgrd.50125.
Chemel, C., M. R. Russo, J. A. Pyle, R. S. Sokhi, and C. Schiller (2009), Quantifying the imprint of a severe Hector Thunderstorm during ACTIVE/SCOUT-O3 onto the water content in the upper troposphere/lower stratosphere, *Mon. Weather Rev.*, *137*, 2493–2514, doi:10.1175/2008MWR2666.1.
Chin, M., and D. D. Davis (1993), Global sources and sinks of OCS and CS2 and their distribution, *Global Biogeochem. Cycles*, *7*(2), 321–337, doi:10.1029/93GB00568.
Chin, M., and D. D. Davis (1995), A reanalysis of carbonyl sulfide as a source of stratospheric background sulfur aerosol, *J. Geophys. Res.*, *100*(D5), 8993–9005, doi:10.1029/95JD00275.
Clarisse, L., and F. Prata (2015), Infrared sounding of volcanic ash, in *Volcanic Ash: Methods of Observation and Monitoring*, edited by S. Mackie, et al., in press.
Clarisse, L., P. F. Coheur, A. J. Prata, D. Hurtmans, A. Razavi, T. Phulpin, J. Hadji-Lazaro, and C. Clerbaux (2008), Tracking and quantifying volcanic SO_2 with IASI, the September 2007 eruption at Jebel at Tair, *Atmos. Chem. Phys.*, *8*, 7723–7734.

Clarisse, L., M. Fromm, Y. Ngadi, L. Emmons, C. Clerbaux, D. Hurtmans, and P. Coheur (2011), Intercontinental transport of anthropogenic sulfur dioxide and other pollutants: An infrared remote sensing case study, *Geophys. Res. Lett.*, *38*, L19806, doi:10.1029/2011GL048976.

Clarisse, L., P.-F. Coheur, N. Theys, D. Hurtmans, and C. Clerbaux (2014), The 2011 Nabro eruption, a SO_2 plume height analysis using IASI measurements, *Atmos. Chem. Phys.*, *14*, 3095–3111, doi:10.5194/acp-14-3095-2014.

Coffey, M. T., and J. W. Hannigan (2010), The temporal trend of stratospheric carbonyl sulfide, *J. Atmos. Chem.*, *67*(1), 61–70.

Cole-Dai, J. (2010), Volcanoes and climate, *Wiley Interdiscip. Rev. Clim. Change*, *1*(6), 824–839, doi:10.1002/wcc.76.

Corti, T. (2008), Unprecedented evidence for deep convection hydrating the tropical stratosphere, *Geophys. Res. Lett.*, *35*, L10810, doi:10.1029/2008GL033641.

Crowley, T. J., and M. B. Unterman (2013), Technical details concerning development of a 1200 yr proxy index for global volcanism, *Earth Syst. Sci. Data*, *5*(1), 187–197, doi:10.1002/jgrd.50692.

Crutzen, P. J. (1976), The possible importance of CSO for the sulfate layer of the stratosphere, *Geophys. Res. Lett.*, *3*, 73–76, doi:10.1029/GL003i002p00073.

Curtius, J., et al. (2005), Observations of meteoric material and implications for aerosol nucleation in the winter Arctic lower stratosphere derived from in situ particle measurements, *Atmos. Chem. Phys.*, *5*, 3053–3069.

Cziczo, D. J., D. S. Thomson, and D. M. Murphy (2001), Ablation, flux, and atmospheric implications of meteors inferred from stratospheric aerosol, *Science*, *291*(5509), 1772–1775.

Dahlkötter, F., M. Gysel, D. Sauer, A. Minikin, R. Baumann, P. Seifert, A. Ansmann, M. Fromm, C. Voigt, and B. Weinzierl (2014), The Pagami Creek smoke plume after long-range transport to the upper troposphere over Europe—Aerosol properties and black carbon mixing state, *Atmos. Chem. Phys.*, *14*, 6111–6137, doi:10.5194/acp-14-6111-2014.

Damoah, R., N. Spichtinger, R. Servranckx, M. Fromm, E. Eloranta, I. Razenkov, P. James, M. Shulski, C. Forster, and A. Stohl (2006), A case study of pyro-convection using a transport model and remote sensing data, *Atmos. Chem. Phys.*, *6*, 173–185.

D'Arrigo, R., R. Wilson, and K. J. Anchukaitis (2013), Volcanic cooling signal in tree ring temperature records for the past millennium, *J. Geophys. Res. Atmos.*, *118*, 9000–9010, doi:10.1002/jgrd.50692.

Della Corte, V., F. J. M. Rietmeijer, A. Rotundi, M. Ferrari, and P. Palumbo (2013), Meteoric CaO and carbon smoke particles collected in the upper stratosphere from an unanticipated source, *Tellus B*, *65*, doi:10.3402/Tellusb.V65i0.20174.

Deshler, T. (2008), A review of global stratospheric aerosol: Measurements, importance, life cycle, and local stratospheric aerosol, *Atmos. Res.*, *90*, 223–232.

Deshler, T., M. E. Hervig, D. J. Hofmann, J. M. Rosen, and J. B. Liley (2003), Thirty years of in situ stratospheric aerosol size distribution measurements from Laramie, Wyoming (41°N), using balloon-borne instruments, *J. Geophys. Res.*, *108*(D5), 4167, doi:10.1029/2002JD002514.

Deshler, T., R. Anderson-Sprecher, H. Jäger, J. Barnes, D. J. Hofmann, B. Clemesha, D. Simonich, M. Osborn, R. G. Grainger, and S. Godin-Beekmann (2006), Trends in the nonvolcanic component of stratospheric aerosol over the period 1971–2004, *J. Geophys. Res.*, *111*, D01201, doi:10.1029/2005JD006089.

Devasthale, A., and S. Fueglistaler (2010), A climatological perspective of deep convection penetrating the TTL during the Indian summer monsoon from the AVHRR and MODIS instruments, *Atmos. Chem. Phys.*, *10*, 4573–4582, doi:10.5194/acp-10-4573-2010.

Dhomse, S. S., R. W. Saunders, W. Tian, M. P. Chipperfield, and J. M. C. Plane (2013), Plutonium-238 observations as a test of modeled transport and surface deposition of meteoric smoke particles, *Geophys. Res. Lett.*, *40*, 4454–4458, doi:10.1002/grl.50840.

Dhomse, S. S., et al. (2014), Aerosol microphysics simulations of the Mt. Pinatubo eruption with the UM-UKCA composition-climate model, *Atmos. Chem. Phys.*, *14*, 11,221–11,246, doi:10.5194/acp-14-11221-2014.

Ding, Y., J. A. Carton, G. A. Chepurin, G. Stenchikov, A. Robock, L. T. Sentman, and J. P. Krasting (2014), Ocean response to volcanic eruptions in Coupled Model Intercomparison Project 5 simulations, *J. Geophys. Res. Oceans*, *119*, 5622–5637, doi:10.1002/2013JC009780.

Dinh, T., and S. Fueglistaler (2014), Cirrus, transport, and mixing in the tropical upper troposphere, *J. Atmos. Sci.*, *71*, 1339–1352, doi:10.1175/JAS-D-13-0147.1.

Driscoll, S., A. Bozzo, L. J. Gray, A. Robock, and G. Stenchikov (2012), Coupled Model Intercomparison Project 5 (CMIP5) simulations of climate following volcanic eruptions, *J. Geophys. Res.*, *117*, D17105, doi:10.1029/2012JD017607.

Eckhardt, S., A. Stohl, H. Wernli, P. James, C. Forster, and N. Spichtinger (2004), A 15-year climatology of warm conveyor belts, *J. Clim.*, *17*, 218–237.

Eckhardt, S., A. J. Prata, P. Seibert, K. Stebel, and A. Stohl (2008), Estimation of the vertical profile of sulfur dioxide injection into the atmosphere by a volcanic eruption using satellite column measurements and inverse transport modeling, *Atmos. Chem. Phys.*, *8*, 3881–3897, doi:10.5194/acp-8-3881-2008.

Elliott, S. (2009), Dependence of DMS global sea-air flux distribution on transfer velocity and concentration field type, *J. Geophys. Res.*, *114*, G02001, doi:10.1029/2008JG000710.

Eloranta, E. E. (2005), High spectral resolution lidar, in *Lidar Range-Resolved Optical Remote Sensing of the Atmosphere*, edited by C. Weitkamp, Springer, New York, doi: 10.1007/b106786.

English, J. M., O. B. Toon, M. J. Mills, and F. Yu (2011), Microphysical simulations of new particle formation in the upper troposphere and lower stratosphere, *Atmos. Chem. Phys.*, *11*(17), 9303–9322.

English, J. M., O. B. Toon, and M. J. Mills (2012), Microphysical simulations of sulfur burdens from stratospheric sulfur geoengineering, *Atmos. Chem. Phys.*, *12*, 4775–4793, doi:10.5194/acp-12-4775-2012.

English, J. M., O. B. Toon, and M. J. Mills (2013), Microphysical simulations of large volcanic eruptions: Pinatubo and Toba, *J. Geophys. Res. Oceans*, *118*, 1880–1895, doi:10.1002/jgrd.50196.

Fahey, D. W., et al. (1993), *In situ* measurements constraining the role of sulphate aerosols in mid-latitude ozone depletion, *Nature*, *363*, 509–514.

Fahey, D. W., et al. (2001), The detection of large HNO_3-containing particles in the winter Arctic stratosphere, *Science*, *291*(5506), 1026–1031, doi:10.1126/science.1057265.

Fairlie, T. D., J. P. Vernier, M. Natarajan, and K. M. Bedka (2014), Dispersion of the Nabro volcanic plume and its relation to the Asian summer monsoon, *Atmos. Chem. Phys.*, *14*(13), 7045–7057, doi:10.5194/acp-14-7045-2014.

Feierabend, K. J., D. K. Havey, S. S. Brown, and V. Vaida (2006), Experimental absolute intensities of the 4v(9) and 5v(9) O-H stretching overtones of H_2SO_4, *Chem. Phys. Lett.*, *420*(4-6), 438–442, doi:10.1016/j.cplett.01.013.

Fiedler, V., F. Arnold, H. Schlager, A. Dörnbrack, L. Pirjola, and A. Stohl (2009a), East Asian SO_2 pollution plume over Europe—Part 2: Evolution and potential impact, *Atmos. Chem. Phys.*, *9*, 4729–4745.

Fiedler, V., R. Nau, S. Ludmann, F. Arnold, H. Schlager, and A. Stohl (2009b), East Asian SO_2 pollution plume over Europe—Part 1: Airborne trace gas measurements and source identification by particle dispersion model simulations, *Atmos. Chem. Phys.*, *9*, 4717–4728.

Fiocco, G., and G. Grams (1964), Observations of the aerosol layer at 20 km by optical radar, *J. Atmos. Sci.*, *21*, 323–324.

Folkins, I., M. Lowewenstein, J. Podolske, S. Oltmans, and M. Proffitt (1999), A barrier to vertical mixing at 14 km in the tropics: Evidence from ozonesondes and aircraft measurements, *J. Geophys. Res.*, *104*(D18), 22,095–22,102, doi:10.1029/1999JD900404.

Frankland, V. L., and J. M. C. Plane (2015), Fe embedded in ice: The impacts of sublimation and energetic particle bombardment, *J. Atmos. Sol. Terr. Phys.*, *127*, 103–110, doi:10.1016/j.jastp.2014.12.004.

Frankland, V. L., A. D. James, W. Feng, and J. M. C. Plane (2015), The uptake of HNO_3 on meteoric smoke analogues, *J. Atmos. Sol. Terr. Phys.*, *127*, 150–160, doi:10.1016/j.jastp.2015.01.010.

Frey, W., R. Schofield, P. Hoor, D. Kunkel, F. Ravegnani, A. Ulanovsky, S. Viciani, F. D'amato, and T. P. Lane (2015), The impact of overshooting deep convection on local transport and mixing in the tropical upper troposphere/lower stratosphere (UTLS), *Atmos. Chem. Phys.*, *15*, 6467–6486.

Friberg, J., B. G. Martinsson, S. M. Andersson, C. A. M. Brenninkmeijer, M. Hermann, P. F. J. Van Velthoven, and A. Zahn (2014), Sources of increase in lowermost stratospheric sulphurous and carbonaceous aerosol background concentrations during 1999–2008 derived from CARIBIC flights, *Tellus*, doi:10.3402/tellusb.v66.23428.

Friedrich, M., M. Rapp, T. Blix, U. P. Hoppe, K. Torkar, S. Robertson, S. Dickson, and K. Lynch (2012), Electron loss and meteoric dust in the mesosphere, *Ann. Geophys.*, *30*(10), 1495–1501, doi:10.5194/angeo-30-1495-2012.

Frölicher, T. L., F. Joos, and C. C. Raible (2011), Sensitivity of atmospheric CO_2 and climate to explosive volcanic eruptions, *Biogeosciences*, *8*, 2317–2339, doi:10.5194/bg-8-2317-2011.

Fromm, M., R. Bevilacqua, R. Servranckx, J. Rosen, J. P. Thayer, J. Herman, and D. Larko (2005), Pyro-cumulonimbus injection of smoke to the stratosphere: Observations and impact of a super blowup in northwestern Canada on 3–4 August 1998, *Geophys. Res. Lett.*, *110*, D08205, doi:10.1029/2004JD005350.

Fromm, M., D. T. Lindsey, R. Servranckx, G. Yue, T. Trickl, R. Sica, P. Doucet, and S. Godin-beekmann (2010), The untold story of pyrocumulonimbus, *Bull. Am. Meteorol. Soc.*, *91*, 1193–1209, doi:10.1175/2010BAMS3004.1.

Fromm, M., G. Kablick, G. Nedoluha, E. Carboni, R. Grainger, J. Campbell, and J. Lewis (2014), Correcting the record of volcanic stratospheric aerosol impact: Nabro and Sarychev Peak, *J. Geophys. Res. Atmos.*, *119*, 10,343–10,364, doi:10.1002/2014JD021507.

Froyd, K. D., D. M. Murphy, T. J. Sanford, D. S. Thomson, J. C. Wilson, L. Pfister, and L. Lait (2009), Aerosol composition of the tropical upper troposphere, *Atmos. Chem. Phys.*, *9*, 4363–4385.

Fueglistaler, S., M. Bonazzola, P. H. Haynes, and T. Peter (2005), Stratospheric water vapor predicted from the Lagrangian temperature history of air entering the stratosphere in the tropics, *J. Geophys. Res.*, *110*, D08107, doi:10.1029/2004JD005516.

Fueglistaler, S., A. E. Dessler, T. J. Dunkerton, I. Folkins, Q. Fu, and P. W. Mote (2009), Tropical tropopause layer, *Rev. Geophys.*, *47*, RG1004, doi:10.1029/2008RG000267.

Gabrielli, P., et al. (2004), Meteoric smoke fallout over the Holocene epoch revealed by iridium and platinum in Greenland ice, *Nature*, *432*(7020), 1011–1014.

Gao, C., A. Robock, and C. Ammann (2008a), Volcanic forcing of climate over the past 1500 years: An improved ice core-based index for climate models, *J. Geophys. Res.*, *113*, D23111, doi:10.1029/2008JD010239.

Gao, R. S., S. R. Hall, W. H. Swartz, J. P. Schwarz, J. R. Spackman, L. A. Watts, D. W. Fahey, K. C. Aikin, R. E. Shetter, and T. P. Bui (2008b), Calculations of solar shortwave heating rates due to black carbon and ozone absorption using in situ measurements, *J. Geophys. Res.*, *113*, D14203, doi:10.1029/2007JD009358.

Glatthor, N., et al. (2015), Tropical sources and sinks of carbonyl sulfide observed from space, *Geophys. Res. Lett.*, *42*, 10,082–10,090, doi:10.1002/2015GL066293.

Gettelman, A., P. Hoor, L. L. Pan, W. J. Randel, M. I. Hegglin, and T. Birner (2011), The extratropical upper troposphere and lower stratosphere, *Rev. Geophys.*, *49*, RG3003, doi:10.1029/2011RG000355.

Gonzi, S., P. I. Palmer, R. Paugam, M. Wooster, and M. N. Deeter (2015), Quantifying pyroconvective injection heights using observations of fire energy: Sensitivity of spaceborne observations of carbon monoxide, *Atmos. Chem. Phys.*, *15*, 4339–4355.

Gorkavyi, N., D. F. Rault, P. A. Newman, A. M. da Silva, and A. E. Dudorov (2013), New stratospheric dust belt due to the Chelyabinsk bolide, *Geophys. Res. Lett.*, *40*, 4728–4733, doi:10.1002/grl.50788.

Griessbach, S., L. Hoffmann, R. Spang, and M. Riese (2014), Volcanic ash detection with infrared limb sounding: MIPAS observations and radiative transfer simulations, *Atmos. Meas. Tech.*, *7*, 1487–1507, doi:10.5194/amt-7-1487-2014.

Griessbach, S., L. Hoffmann, R. Spang, M. von Hobe, R. Müller, and M. Riese (2015), Infrared limb emission measurements of aerosol in the troposphere and stratosphere, *Atmos. Meas. Tech. Discuss.*, *8*, 4379–4412, doi:10.5194/amtd-8-4379-2015.

Guan, H., R. Esswein, J. Lopez, R. Bergstrom, A. Warnock, M. Follette-cook, M. Fromm, and L. T. Iraci (2010), A multi-decadal history of biomass burning plume heights identified using aerosol index measurements, *Atmos. Chem. Phys.*, *10*, 6461–6469, doi:10.5194/acp-10-6461-2010.

Guo, S., G. J. S. Bluth, W. I. Rose, I. M. Watson, and A. J. Prata (2004a), Re-evaluation of SO_2 release of the 15 June 1991 Pinatubo eruption using ultraviolet and infrared satellite sensors, *Geochem. Geophys. Geosyst.*, *5*, Q04001, doi:10.1029/2003GC000654.

Guo, S., W. I. Rose, G. J. S. Bluth, and I. M. Watson (2004b), Particles in the great Pinatubo volcanic cloud of June 1991: The role of ice, *Geochem. Geophys. Geosyst.*, *5,* Q05003, doi:10.1029/2003GC000655.

Halloran, P. R., T. G. Bell, and I. J. Totterdell (2010), Can we trust empirical marine DMS parameterisations within projections of future climate?, *Biogeosciences*, *7*(5), 1645–1656.

Hamill, P., O. B. Toon, and R. P. Turco (1990), Aerosol nucleation in the winter Arctic and Antarctic stratospheres, *Geophys. Res. Lett.*, *17*(4), 417–420, doi:10.1029/GL017i004p00417.

Hansen, J., A. Lacis, R. Ruedy, and M. Sato (1992), Potential climate impact of Mount Pinatubo eruption, *Geophys. Res. Lett.*, *19*, 215–218, doi:10.1029/91GL02788.

Hassim, M. E. E., and T. P. Lane (2010), A model study on the influence of overshooting convection on TTL water vapour, *Atmos. Chem. Phys.*, *10*, 9833–9849, doi:10.5194/acp-10-9833-2010.

Haywood, J. M., et al. (2010), Observations of the eruption of the Sarychev volcano and simulations using the HadGEM2 climate model, *J. Geophys. Res.*, *115*, D21212, doi:10.1029/2010JD014447.

Haywood, J. M., A. Jones, N. Bellouin, and D. Stephenson (2013), Asymmetric forcing from stratospheric aerosols impacts Sahelian rainfall, *Nat. Clim. Change*, *3*, 660–665, doi:10.1038/nclimate1857.

Hegerl, G. C., T. J. Crowley, M. Allen, W. T. Hyde, H. N. Pollack, J. Smerdon, and E. Zorita (2007), Detection of human influence on a new, validated 1500-year temperature reconstruction, *J. Clim.*, *20*(4), 650–666, doi:10.1175/JCLI4011.1.

Hendricks, J., B. Kärcher, A. Döpelheuer, J. Feichter, U. Lohmann, and D. Baumgardner (2004), Simulating the global atmospheric black carbon cycle: A revisit to the contribution of aircraft emissions, *Atmos. Chem. Phys.*, *4*, 2521–2541.

Hermann, M., and A. Wiedensohler (2001), Counting efficiency of condensation particle counters at low-pressures with illustrative data from the upper troposphere, *J. Aerosol Sci.*, *32*(8), 975–991.
Hervig, M. E., and T. Deshler (2002), Evaluation of aerosol measurements from SAGE II, HALOE, and balloonborne optical particle counters, *J. Geophys. Res.*, *107*(D3), 4031, doi:10.1029/2001JD000703.
Hervig, M. E., J. Russell, L. L. Gordley, J. H. Park, S. R. Drayson, and T. Deshler (1996), Validation of aerosol measurements from the Halogen Occultation Experiment, *J. Geophys. Res.*, *101*(D6), 10,267–10,275, doi:10.1029/95JD02464.
Hervig, M. E., T. Deshler, and J. M. Russell III (1998), Aerosol size distributions obtained from HALOE spectral extinction measurements, *J. Geophys. Res.*, *103*(D1), 1573–1583, doi:10.1029/97JD03081.
Hervig, M. E., L. L. Gordley, L. E. Deaver, D. E. Siskind, M. H. Stevens, J. M. Russell, S. M. Bailey, L. Megner, and C. G. Bardeen (2009), First satellite observations of meteoric smoke in the middle atmosphere, *Geophys. Res. Lett.*, *36*, L18805, doi:10.1029/2009GL039737.
Hervig, M. E., L. E. Deaver, C. G. Bardeen, J. M. Russell, S. M. Bailey, and L. L. Gordley (2012), The content and composition of meteoric smoke in mesospheric ice particles from SOFIE observations, *J. Atmos. Sol. Terr. Phys.*, *84–85*, 1–6, doi:10.1016/j.jastp.2012.04.005.
Hintze, P. E., H. G. Kjaergaard, V. Vaida, and J. B. Burkholder (2003), Vibrational and electronic spectroscopy of sulfuric acid vapor, *J. Phys. Chem. A*, *107*(8), 1112–1118, doi:10.1021/jp0263626.
Hobbs, P. V., L. F. Radke, M. W. Eltgroth, and D. A. Hegg (1981), Airborne studies of the emissions from the volcanic eruptions of Mount St. Helens, *Science*, *211*(4484), 816–818.
Hofmann, D., J. Barnes, M. O'Neill, M. Trudeau, and R. Neely (2009), Increase in background stratospheric aerosol observed with lidar at Mauna Loa Observatory and Boulder, Colorado, *Geophys. Res. Lett.*, *36*, L15808, doi:10.1029/2009GL039008.
Hofmann, D. J., J. M. Rosen, T. J. Pepin, and R. G. Pinnick (1975), Stratospheric aerosol measurements I: Time variations at northern midlatitudes, *J. Atmos. Sci.*, *32*, 1446–1456.
Hofmann, D. J., J. M. Rosen, and W. Gringel (1985), Delayed production of sulfuric acid condensation nuclei in the polar stratosphere from El Chichon volcanic vapors, *J. Geophys. Res.*, *90*(D1), 2341–2354, doi:10.1029/JD090iD01p02341.
Holton, J. R. (2004), *An Introduction to Dynamic Meteorology*, 4th ed., Elsevier Academic Press, Oxford, U. K.
Holton, J. R., P. Haynes, M. E. McIntyre, A. R. Douglass, R. B. Rood, and L. Pfister (1995), Stratosphere-troposphere exchange, *Rev. Geophys.*, *33*(4), 403–439, doi:10.1029/95RG02097.
Hommel, R., C. Timmreck, and H. F. Graf (2011), The global middle-atmosphere aerosol model MAECHAM5-SAM2: Comparison with satellite and in-situ observations, *Geosci. Model Dev.*, *4*, 809–834, doi:10.5194/gmd-4-809-2011.
Höpfner, M., N. Glatthor, U. Grabowski, S. Kellmann, M. Kiefer, A. Linden, J. Orphal, G. Stiller, T. von Clarmann, and B. Funke (2013), Sulfur dioxide (SO_2) as observed by MIPAS/Envisat: Temporal development and spatial distribution at 15–45 km altitude, *Atmos. Chem. Phys.*, *13*(20), 10,405–10,423, doi:10.5194/acp-13-10405-2013.
Höpfner, M., et al. (2015), Sulfur dioxide (SO2) from MIPAS in the upper troposphere and lower stratosphere 2002–2012, *Atmos. Chem. Phys.*, *15*, 7017–7037, doi:10.5194/acp-15-7017-2015.
Hsu, N. C., C. Li, N. A. Krotkov, Q. Liang, K. Yang, and S.-C. Tsay (2012), Rapid transpacific transport in autumn observed by the A-train satellites, *J. Geophys. Res.*, *117*, D06312, doi:10.1029/2011JD016626.
Huang, W., X. Chu, C. S. Gardner, J. D. Carrillo-Sánchez, W. Feng, J. M. C. Plane, and D. Nesvorný (2015), Measurements of the vertical fluxes of atomic Fe and Na at the mesopause: Implications for the velocity of cosmic dust entering the atmosphere, *Geophys. Res. Lett.*, *42*, 169–175, doi:10.1002/2014GL062390.
Hudson, P. K., D. M. Murphy, D. J. Cziczo, D. S. Thomson, J. A. de Gouw, J. A. Warneke, J. Holloway, H.-J. Jost, and G. Hübler (2004), Biomass-burning particle measurements: Characteristic composition and chemical processing, *J. Geophys. Res.*, *109*, D23S27, doi:10.1029/2003JD004398.
Iles, C. E., and G. C. Hegerl (2014), The global precipitation response to volcanic eruptions in the CMIP5 models, *Environ. Res. Lett.*, *9*(10), doi:10.1088/1748-9326/9/10/104012.
Iles, C. E., G. C. Hegerl, A. P. Schurer, and X. Zhang (2013), The effect of volcanic eruptions on global precipitation, *J. Geophys. Res. Atmos.*, *118*, 8770–8786, doi:10.1002/jgrd.50678.
Illingworth, A. J., et al. (2015), The EarthCARE satellite: The next step forward in global measurements of clouds, aerosols, precipitation, and radiation, *Bull. Am. Meteorol. Soc.*, *96*(8), doi:10.1175/BAMS-D-12-00227.
Inn, E. C. Y., and J. F. Vedder (1981), Measurements of stratospheric sulfur constituents, *Geophys. Res. Lett.*, *8*, 5–8, doi:10.1029/GL008i001p00005.
Jacob, D. J. (1999), *Introduction to Atmospheric Chemistry*, 280 pp., Princeton Univ. Press, Princeton, New Jersey N. J.
Jäger, H. (2005), Long-term record of lidar observations of the stratospheric aerosol layer at Garmisch-Partenkirchen, *J. Geophys. Res.*, *110*, D08106, doi:10.1029/2004JD005506.
Jäger, H., and T. Deshler (2002), Lidar backscatter to extinction, mass and area conversions for stratospheric aerosols based on midlatitude balloon-borne size distribution measurements, *Geophys. Res. Lett.*, *29*(19), 1929, doi:10.1029/2002GL015609.
Jäger, H., and T. Deshler (2003), Correction to Lidar backscatter to extinction, mass and area conversions for stratospheric aerosols based on midlatitude balloonborne size distribution measurements, *Geophys. Res. Lett.*, *30*(7), 1382, doi:10.1029/2003GL017189.
Jenniskens, P., M. A. Wilson, D. Packan, C. O. Laux, C. H. Krüger, I. D. Boyd, O. P. Popova, and M. Fonda (2000), Meteors: A delivery mechanism of organic matter to the early Earth, *Earth Moon Planets*, *82-83*, 57–70.
Jensen, E. J., A. S. Ackerman, and J. A. Smith (2007), Can overshooting convection dehydrate the tropical tropopause layer?, *J. Geophys. Res.*, *112*, D11209, doi:10.1029/2006JD007943.
Jonsson, H. H., et al. (1995), Performance of a focused cavity aerosol spectrometer for measurements in the stratosphere of particle size in the 0.06–2.0-μm-diameter range, *J. Atmos. Oceanic Technol.*, *12*, 115–129.
Jungclaus, J. H., et al. (2010), Climate and carbon-cycle variability over the last millennium, *Clim. Past*, *6*, 723–737, doi:10.5194/cp-6-723-2010.
Junge, C. E., and J. E. Manson (1961), Stratospheric aerosol studies, *J. Geophys. Res.*, *66*, 2163–2182, doi:10.1029/JZ066i007p02163.
Junge, C. E., C. W. Chagnon, and J. E. Manson (1961), Stratospheric aerosols, *J. Meteorol.*, *18*, 81–108.
Karagulian, F., L. Clarisse, C. Clerbaux, A. J. Prata, D. Hurtmans, and P. F. Coheur (2010), Detection of volcanic SO_2, ash, and H_2SO_4 using the Infrared Atmospheric Sounding Interferometer (IASI), *J. Geophys. Res.*, *115*, DO0L02, doi:10.1029/2009JD012786.
Kärcher, B., O. Möhler, P. J. Demott, S. Pechtl, and F. Yu (2007), Insights into the role of soot aerosols in cirrus cloud formation, *Atmos. Chem. Phys.*, *7*, 4293–4227, doi:10.5194/acp-7-4203-2007.
Kaye, J. A., and T. L. Miller (1996), The ATLAS series of shuttle missions, *Geophys. Res. Lett.*, *23*(17), 2285–2288, doi:10.1029/96GL02228.
Kent, G. S., C. Trepte, P.-H. Wang, and P. Lucker (2003), Problems in separating aerosol and cloud in the Stratospheric Aerosol and Gas Experiment (SAGE) II data set under conditions of lofted dust: Application to the Asian deserts, *J. Geophys. Res.*, *108*(D14), 4410, doi:10.1029/2002JD002412.

Kettle, A. J., and M. O. Andreae (2000), Flux of dimethylsulfide from the oceans: A comparison of updated data seas and flux models, *J. Geophys. Res.*, *105*(D22), 26,793–26,808, doi:10.1029/2000JD900252.
Kettle, A. J., et al. (1999), A global database of sea surface dimethylsulfide (DMS) measurements and a procedure to predict sea surface DMS as a function of latitude, longitude, and month, *Global Biogeochem. Cycles*, *13*(2), 399–444, doi:10.1029/1999GB900004.
Kettle, A. J., T. S. Rhee, M. von Hobe, A. Poulton, J. Aiken, and M. O. Andreae (2001), Assessing the flux of different volatile sulfur gases from the ocean to the atmosphere, *J. Geophys. Res.*, *106*(D11), 12,193–12,209, doi:10.1029/2000JD900630.
Kettle, A. J., U. Kuhn, M. von Hobe, J. Kesselmeier, and M. O. Andreae (2002a), Global budget of atmospheric carbonyl sulfide: Temporal and spatial variations of the dominant sources and sinks, *J. Geophys. Res.*, *107*(D22), 4658, doi:10.1029/2002JD002187.
Kettle, A. J., U. Kuhn, M. von Hobe, J. Kesselmeier, P. S. Liss, and M. O. Andreae (2002b), Comparing forward and inverse models to estimate the seasonal variation of hemisphere-integrated fluxes of carbonyl sulfide, *Atmos. Chem. Phys.*, *2*, 343–361.
Kinne, S., et al. (2006), An AeroCom initial assessment optical properties in aerosol component modules of global models, *Atmos. Chem. Phys.*, *6*, 1815–1834.
Klett, J. D. (1985), Lidar inversion with variable backscatter/extinction ratios, *Appl. Opt.*, *24*(11), 1638–1643, doi:10.1364/AO.24.001638.
Klocke, D. (2011), Assessing the uncertainty in climate sensitivity, PhD thesis, 87 pp., Max Planck Institute for Meteorology Hamburg, Germany.
Kokkola, H., R. Hommel, J. Kazil, U. Niemeier, A.-I. Partanen, J. Feichter, and C. Timmreck (2009), Aerosol microphysics modules in the framework of the ECHAM5 climate model—Intercomparison under stratospheric conditions, *Geosci. Model Dev.*, *2*, 97–112, doi:10.5194/gmd-2-97-2009.
Konopka, P., J.-U. Grooß, F. Plöger, and R. Müller (2009), Annual cycle of horizontal in-mixing into the lower tropical stratosphere, *J. Geophys. Res.*, *114*, D19111, doi:10.1029/2009JD011955.
Kovilakam, M., and T. Deshler (2015), On the accuracy of stratospheric aerosol extinction derived from in situ size distribution measurements and surface area density derived from remote SAGE II and HALOE extinction measurements, *J. Geophys. Res. Atmos.*, *120*, 8426–8447, doi:10.1002/2015JD023303.
Krämer, M., C. Twohy, M. Hermann, A. Afchine, S. Dhaniyala, and A. Korolev (2013), Aerosol and cloud particle sampling, in *Airborne Measurements for Environmental Research: Methods and Instruments,* edited by M. Wendisch and J.-L. Brenguier, Wiley-VCH Verlag GmbH & Co. KGaA, Weinheim, Germany, doi:10.1002/9783527653218.ch6.
Kremser, S., I. Wohltmann, M. Rex, U. Langematz, M. Dameris, and M. Kunze (2009), Water vapour transport in the tropical tropopause region in coupled Chemistry-Climate Models and ERA-40 reanalysis data, *Atmos. Chem. Phys.*, *9*, 2679–2694.
Kremser, S., N. B. Jones, M. Palm, B. Lejeune, Y. Wang, D. Smale, and N. M. Deutscher (2015), Positive trends in Southern Hemisphere carbonyl sulfide (OCS), *Geophys. Res. Lett.*, *42*, 9473–9480, doi:10.1002/2015GL065879.
Kristiansen, N. I., et al. (2010), Remote sensing and inverse transport modeling of the Kasatochi eruption sulfur dioxide cloud, *J. Geophys. Res.*, *115*, D00L16, doi:10.1029/2009JD013286.
Krotkov, N. A., M. R. Schoeberl, G. A. Morris, S. Carn, and K. Yang (2010), Dispersion and lifetime of the SO_2 cloud from the August 2008 Kasatochi eruption, *J. Geophys. Res.*, *115*, D00L20, doi:10.1029/2010JD013984.
Krysztofiak, G., Y. V. Te, V. Catoire, G. Berthet, G. C. Toon, F. Jegou, P. Jeseck, and C. Robert (2015), Carbonyl sulphide (OCS) variability with latitude in the atmosphere, *Atmos. Ocean*, *53*(1), 89–101, doi:10.1080/07055900.2013.876609.
Kuai, L., J. Worden, S. S. Kulawik, S. A. Montzka, and J. Liu (2014), Characterization of Aura TES carbonyl sulfide retrievals over ocean, *Atmos. Meas. Tech.*, *7*(1), 163–172, doi:10.5194/amt-7-163-2014.
Kulmala, M., H. Vehkamäki, T. Petäjä, M. D. Maso, A. Lauri, V.-M. Kerminen, W. Birmili, and P. H. Mcmurry (2004), Formation and growth rates of ultrafine atmospheric particles: A review of observations, *J. Aerosol Sci.*, *35*(2), 143–176, doi:10.1016/j.jaerosci.2003.10.003.
Laakso, A., A.-I. Partanen, H. Kokkola, A. Laaksonen, K. E. J. Lehtinen, and H. Korhonen (2012), Stratospheric passenger flights are likely an inefficient geoengineering strategy, *Environ. Res. Lett.*, *7*(3), doi:10.1088/1748-9326/7/3/034021.
Lambert, A., R. G. Grainger, J. J. Remedios, C. D. Rodgers, M. Corney, and F. W. Taylor (1993), Measurements of the evolution of the Mt. Pinatubo aerosol cloud by ISAMS, *Geophys. Res. Lett.*, *20*(12), 1287–1290, doi:10.1029/93GL00827.
Lambert, A., R. G. Grainger, J. J. Remedios, W. J. Reburn, C. D. Rodgers, F. W. Taylor, A. E. Roche, J. B. Kumer, S. T. Massie, and T. Deshler (1996), Validation of aerosol measurements from the improved stratospheric and mesospheric sounder, *J. Geophys. Res.*, *101*(D6), 9811–9830, doi:10.1029/95JD01702.
Lana, A., et al. (2011), An updated climatology of surface dimethylsulfide concentrations and emission fluxes in the global ocean, *Global Biogeochem. Cycles*, *25*, GB1004, doi:10.1029/2010GB003850.
Lanciki, A., J. Cole-Dai, M. H. Thiemens, and J. Savarino (2012), Sulfur isotope evidence of little or no stratospheric impact by the 1783 Laki volcanic eruption, *Geophys. Res. Lett.*, *39*, L01806, doi:10.1029/2011GL050075.
Land, P. E., J. D. Shutler, T. G. Bell, and M. Yang (2014), Exploiting satellite Earth observation to quantify current global oceanic DMS flux and its future climate sensitivity, *J. Geophys. Res. Oceans*, *119*, 7725–7740, doi:10.1002/2014JC010104.
Lane, J. R., and H. G. Kjaergaard (2008), Calculated electronic transitions in sulfuric acid and implications for its photodissociation in the atmosphere, *J. Phys. Chem. A*, *112*(22), 4958–4964, doi:10.1021/jp710863r.
Launois, T., S. Belviso, L. Bopp, C. G. Fichot, and P. Peylin (2015), A new model for the global biogeochemical cycle of carbonyl sulfide—Part 1: Assessment of direct marine emissions with an oceanic general circulation and biogeochemistry model, *Atmos. Chem. Phys.*, *15*(5), 2295–2312.
Lee, C., R. V. Martin, A. van Donkelaar, H. Lee, R. R. Dickerson, J. C. Hains, N. Krotkov, A. Richter, K. Vinnikov, and J. J. Schwab (2011), SO_2 emissions and lifetimes: Estimates from inverse modeling using in situ and global, space-based (SCIAMACHY and OMI) observations, *J. Geophys. Res.*, *116*, D06304, doi:10.1029/2010JD014758.
Lelieveld, J. (1993), *Multi-Phase Processes in the Atmospheric Sulfur Cycle*, pp. 305–331, Springer, New York.
Lopez, T., S. Carn, C. Werner, D. Fee, P. Kelly, M. Doukas, M. Pfeffer, P. Webley, C. Cahill, and D. Schneider (2013), Evaluation of Redoubt Volcano's sulfur dioxide emissions by the Ozone Monitoring Instrument, *J. Volcanol. Geotherm. Res.*, *259*, 290–307, doi:10.1016/j.jvolgeores.2012.03.002.
Mackinnon, I. D. R., D. S. Mckay, G. Nace, and A. M. Isaacs (1982), Classification of the Johnson Space Center stratospheric dust collection, *J. Geophys. Res.*, *87*, A413–A421, doi:10.1029/JB087iS01p0A413.
Madonna, E., H. Wernli, and H. Joos (2014), Warm conveyor belts in the ERA-Interim dataset (1979–2010). Part I: Climatology and potential vorticity evolution, *J. Clim.*, *27*, 3–26.
Mann, G., S. Dhomse, A. Schmidt, R. Neely, C. Timmreck, T. Deshler, and L. Thomason (2015), Realistic global particle size evolution key to improved volcanic forcings, *Past Global Changes Magazine*, *23*(2), 52–53.

Mann, M. E., S. Rutherford, A. Schurer, S. F. Tett, and J. D. Fuentes (2013), Discrepancies between the modeled and proxy-reconstructed response to volcanic forcing over the past millennium: Implications and possible mechanisms, *J. Geophys. Res. Atmos.*, *118*, 7617–7627, doi:10.1002/jgrd.50609.

Marandino, C. A., S. Tegtmeier, K. Krüger, C. Zindler, E. L. Atlas, F. Moore, and H. W. Bange (2013), Dimethylsulphide (DMS) emissions from the western Pacific Ocean: A potential marine source for stratospheric sulphur?, *Atmos. Chem. Phys.*, *13*(16), 8427–8437, doi:10.5194/acp-13-8427-2013.

Marotzke, J., and P. M. Forster (2015), Forcing, feedback and internal variability in global temperature trends, *Nature*, *517*, 565–570, doi:10.1038/nature14117.

Massie, S. T., et al. (1996), Validation studies using multiwavelength Cryogenic Limb Array Etalon Spectrometer (CLAES) observations of stratospheric aerosol, *J. Geophys. Res.*, *101*(D6), 9757–9773, doi:10.1029/95JD03225.

Mathews, J. D., D. Janches, D. D. Meisel, and Q. H. Zhou (2001), The micrometeoroid mass flux into the upper atmosphere: Arecibo results and a comparison with prior estimates, *Geophys. Res. Lett.*, *28*(10), 1929–1932, doi:10.1029/2000GL012621.

McCormick, B., M. Edmonds, T. Mather, R. Campion, C. S. L. Hayer, H. Thomas, and S. Carn (2013), Volcano monitoring applications of the Ozone Monitoring Instrument, *Geol. Soc. Spec. Publ.*, *380*, 259–291, doi:10.1144/SP380.11.

McCormick, B. T., M. Edmonds, T. A. Mather, and S. A. Carn (2012), First synoptic analysis of volcanic degassing in Papua New Guinea, *Geochem. Geophys. Geosyst.*, *13*, Q03008, doi:10.1029/2011GC003945.

McCormick, M. P., and R. E. Veiga (1992), SAGE II measurements of early Pinatubo aerosols, *Geophys. Res. Lett.*, *19*, 155–158, doi:10.1029/91GL02790.

McCormick, M. P., L. W. Thomason, and C. R. Trepte (1995), Atmospheric effects of the Mt Pinatubo eruption, *Nature*, *373*, 399–404.

McIntyre, M. E., and T. N. Palmer (1983), Breaking planetary waves in the stratosphere, *Nature*, *305*, 593–600.

Megner, L., D. E. Siskind, M. Rapp, and J. Gumbel (2008), Global and temporal distribution of meteoric smoke: A two-dimensional simulation study, *J. Geophys. Res.*, *113*, D03202, doi:10.1029/2007JD009054.

Merikanto, J., I. Napari, H. Vehkamäki, T. Anttila, and M. Kulmala (2007), New parameterization of sulfuric acid-ammonia-water ternary nucleation rates at tropospheric conditions, *J. Geophys. Res.*, *112*, D15207, doi:10.1029/2006JD007977.

Miller, G. H., et al. (2012), Abrupt onset of the Little Ice Age triggered by volcanism and sustained by sea-ice/ocean feedbacks, *Geophys. Res. Lett.*, *39*, L02708, doi:10.1029/2011GL050168.

Miller, Y., R. B. Gerber, and V. Vaida (2007), Photodissociation yields for vibrationally excited states of sulfuric acid under atmospheric conditions, *Geophys. Res. Lett.*, *34*, L16820, doi:10.1029/2007GL030529.

Mills, M. J., A. O. Langford, T. J. O'Leary, K. Arpag, H. L. Miller, M. H. Proffitt, R. W. Sanders, and S. Solomon (1993), On the relationship between stratospheric aerosol and nitrogen dioxide, *Geophys. Res. Lett.*, *20*, 1187–1190, doi:10.1029/93GL01124.

Mills, M. J., O. B. Toon, and S. Solomon (1999), A 2D microphysical model of the polar stratospheric CN layer, *Geophys. Res. Lett.*, *26*, 1133–1136, doi:10.1029/1999GL900187.

Mills, M. J., O. B. Toon, and G. E. Thomas (2005a), Mesospheric sulfate aerosol layer, *J. Geophys. Res.*, *110*, D24208, doi:10.1029/2005JD006242.

Mills, M. J., O. B. Toon, V. Vaida, P. E. Hintze, H. G. Kjaergaard, D. P. Schofield, and T. W. Robinson (2005b), Photolysis of sulfuric acid vapor by visible light as a source of the polar stratospheric CN layer, *J. Geophys. Res.*, *110*, D08201, doi:10.1029/2004JD005519.

Mills, M. J., et al. (2016), Global volcanic aerosol properties derived from emissions, 1990-2014, using CESM1(WACCM), *J. Geophys. Res. Atmos.*, doi:10.1002/2015JD024290.

Montzka, S. A., P. Calvert, B. D. Hall, J. W. Elkins, T. J. Conway, P. P. Tans, and C. Sweeney (2007), On the global distribution, seasonality, and budget of atmospheric carbonyl sulfide (COS) and some similarities to CO_2, *J. Geophys. Res.*, *112*, D09302, doi:10.1029/2006JD007665.

Morgenstern, O., P. Braesicke, F. M. O'Connor, A. C. Bushell, C. E. Johnson, S. M. Osprey, and J. A. Pyle (2009), Evaluation of the new UKCA climate-composition model—Part 1: The stratosphere, *Geosci. Model Dev.*, *2*, 43–57, doi:10.5194/gmd-2-43-2009.

Murphy, D. M., D. J. Cziczo, P. K. Hudson, and D. S. Thomson (2007), Carbonaceous material in aerosol particles in the lower stratosphere and tropopause region, *J. Geophys. Res.*, *112,* D04203, doi:10.1029/2006JD007297.

Murphy, D. M., K. D. Froyd, J. P. Schwarz, and J. C. Wilson (2014), Observations of the chemical composition of stratospheric aerosol particles, *Q. J. R. Meteorol. Soc.*, *140*(681), 1269–1278, doi:10.1002/qj.2213.

Naik, V., et al. (2013), Preindustrial to present-day changes in tropospheric hydroxyl radical and methane lifetime from the Atmospheric Chemistry and Climate Model Intercomparison Project (ACCMIP), *Atmos. Chem. Phys.*, *13*(10), 5277–5298, doi:10.5194/acp-13-5277-2013.

Neely, R. R., et al. (2013), Recent anthropogenic increases in SO_2 from Asia have minimal impact on stratospheric aerosol, *Geophys. Res. Lett.*, *40*, 999–1004, doi:10.1002/grl.50263.

Neely, R. R., P. Yu, K. H. Rosenlof, O. B. Toon, J. S. Daniel, S. Solomon, and H. L. Miller (2014), The contribution of anthropogenic SO_2 emissions to the Asian tropopause aerosol layer, *J. Geophys. Res. Atmos.*, *119*, 1571–1579, doi:10.1002/2013JD020578.

Neu, J. L., and R. A. Plumb (1999), Age of air in a "leaky pipe" model of stratospheric transport, *J. Geophys. Res.*, *104*(D16), 19,243–19,255, doi:10.1029/1999JD900251.

Newhall, C., and S. Self (1982), The Volcanic Explosivity Index (VEI): An estimate of explosive magnitude for historical volcanism, *J. Geophys. Res.*, *87*(C2), 1231–1238, doi:10.1029/JC087iC02p01231.

Nguyen, H. N., A. Gudmundsson, and B. G. Martinsson (2006), Design and calibration of a multi-channel aerosol sampler for tropopause region studies from the CARIBIC platform, *Aerosol Sci. Technol.*, *40*, 649–655.

Nguyen, H. N., et al. (2008), Chemical composition and morphology of individual aerosol particles from a CARIBIC flight at 10 km altitude between 50 N and 30S, *J. Geophys. Res.*, *113*, D23209, doi:10.1029/2008JD009956.

Niemeier, U., and C. Timmreck (2015), What is the limit of climate engineering by stratospheric injection of SO_2?, *Atmos. Chem. Phys.*, *15*(16), 9129–9141, doi:10.5194/acp-15-9129-2015.

Niemeier, U., C. Timmreck, H.-F. Graf, S. Kinne, S. Rast, and S. Self (2009), Initial fate of fine ash and sulfur from large volcanic eruptions, *Atmos. Chem. Phys.*, *9*, 9043–9057, doi:10.5194/acp-9-9043-2009.

Notholt, J., et al. (2003), Enhanced upper tropical tropospheric COS: Impact on the stratospheric aerosol layer, *Science*, *300*, 307–310.

Notholt, J., et al. (2005), Influence of tropospheric SO_2 emissions on particle formation and the stratospheric humidity, *Geophys. Res. Lett.*, *32*, L07810, doi:10.1029/2004GL022159.

Oppenheimer, C., P. Francis, and J. Stix (1998), Depletion rates of sulfur dioxide in tropospheric volcanic plumes, *Geophys. Res. Lett.*, *25*(14), 2671–2674, doi:10.1029/98GL01988.

Park, M., W. J. Randel, L. K. Emmons, P. F. Bernath, K. A. Walker, and C. D. Boone (2008), Chemical isolation in the Asian monsoon anticyclone observed in Atmospheric Chemistry Experiment (ACE-FTS) data, *Atmos. Chem. Phys.*, *8*(3), 757–764.

Park, S., et al. (2010), Vertical transport rates and concentrations of OH and Cl radicals in the tropical tropopause layer from observations of CO_2 and halocarbons: Implications for distributions of long- and short-lived chemical species, *Atmos. Chem. Phys.*, *10*(14), 6669–6684, doi:10.5194/acp-10-6669-2010.

Peter, T., and J. Grooß (2012), Polar stratospheric clouds and sulfate aerosol particles: Microphysics, denitrification and heterogeneous chemistry, in *Stratospheric Ozone Depletion and Climate Change*, pp. 108–144, Royal Society of Chemistry, Cambridge, U. K.

Pifko, S., D. Janches, S. Close, J. Sparks, T. Nakamura, and D. Nesvorny (2013), The meteoroid input function and predictions of mid-latitude meteor observations by the MU radar, *Icarus*, *223*(1), 444–459, doi:10.1016/j.icarus.2012.12.014.

Pinto, J. P., R. P. Turco, and O. B. Toon (1989), Self-limiting physical and chemical effects in volcanic eruption clouds, *J. Geophys. Res.*, *94*(D8), 11,165–11,174, doi:10.1029/JD094iD08p11165.

Pitari, G., V. Aquila, B. Kravitz, A. Robock, S. Watanabe, I. Cionni, N. De Luca, G. Di Genova, E. Mancini, and S. Tilmes (2014), Stratospheric ozone response to sulphate geoengineering: Results from the Geoengineering Model Intercomparison Project (GeoMIP), *J. Geophys. Res. Atmos.*, *119*, 2629–2653, doi:10.1002/2013JD020566.

Plane, J. M. C. (2012), Cosmic dust in the Earth's atmosphere, *Chem. Soc. Rev.*, *41*(19), 6507–6518.

Plane, J. M. C., et al. (2014), A combined rocket-borne and ground-based study of the sodium layer and charged dust in the upper mesosphere, *J. Atmos. Sol. Terr. Phys.*, *118*, 151–160.

Plane, J. M. C., W. Feng, and E. C. M. Dawkins (2015), The mesosphere and metals: Chemistry and changes, *Chem. Rev.*, *115*, 4497–4541, doi:10.1021/cr500501m.

Ploeger, F., G. Gunther, P. Konopka, S. Fueglistaler, R. Muller, C. Hoppe, A. Kunz, R. Spang, J.-U. Grooß, and M. Riese (2013), Horizontal water vapor transport in the lower stratosphere from subtropics to high latitudes during boreal summer, *J. Geophys. Res. Atmos.*, *118*, 8111–8127, doi:10.1002/jgrd.50636.

Plumb, R. A. (1996), A "tropical pipe" model of stratospheric transport, *J. Geophys. Res.*, *101*(D2), 3957–3972, doi:10.1029/95JD03002.

Plumb, R. A. (2002), Stratospheric transport, *J. Meteorol. Soc. Jpn.*, *80*, 793–809.

Post, M. J. (1996), A graphical technique for retrieving size distribution parameters from multiple measurements: Visualization and error analysis, *J. Atmos. Oceanic Technol.*, *13*, 863–873.

Prata, A. J. (2009), Satellite detection of hazardous volcanic clouds, *Nat. Hazards*, *51*, 302–324, doi:10.1007/s11069-008-9273-z.

Prata, A. J., S. A. Carn, A. Stohl, and J. Kerkmann (2007), Long range transport and fate of a stratospheric volcanic cloud from Soufriere Hills volcano, Montserrat, *Atmos. Chem. Phys.*, *7*, 5093–5103.

Prata, A. J., G. Gangale, L. Clarisse, and F. Karagulian (2010), Ash and sulfur dioxide in the 2008 eruptions of Okmok and Kasatochi: Insights from high spectral resolution satellite measurements, *J. Geophys. Res.*, *115*, D00L18, doi:10.1029/2009JD013556.

Prather, M. J., and J. M. Rodriguez (1988), Antarctic ozone: Meteoric control of HNO_3, *Geophys. Res. Lett.*, *15*(1), 1–4, doi:10.1029/GL015i001p00001.

Pumphrey, H. C., M. L. Santee, N. J. Livesey, M. J. Schwartz, and W. G. Read (2011), Microwave Limb Sounder observations of biomass-burning products from the Australian bush fires of February 2009, *Atmos. Chem. Phys.*, *11*, 6285–6296, doi:10.5194/acp-11-6285-2011.

Rampino, M. R., and S. Self (1992), Volcanic winter and accelerated glaciation following the Toba super-eruption, *Nature*, *359*, 50–52.

Randall, C. E., R. M. Bevilacqua, J. D. Lumpe, K. W. Hoppel, D. W. Rusch, and E. P. Shettle (2000), Comparison of Polar Ozone and Aerosol Measurement (POAM) II and Stratospheric Aerosol and Gas Experiment (SAGE) II aerosol measurements from 1994 to 1996, *J. Geophys. Res.*, *105*(D3), 3929–3942, doi:10.1029/1999JD901024.

Randall, C. E., R. M. Bevilacqua, J. D. Lumpe, and K. W. Hoppel (2001), Validation of POAM III aerosols: Comparison to SAGE II and HALOE, *J. Geophys. Res.*, *106*(D21), 27,525–27,536, doi:10.1029/2001JD000528.

Randel, W. J., M. Park, L. Emmons, D. Kinnison, P. Bernath, K. A. Walker, C. Boone, and H. Pumphrey (2010), Asian monsoon transport of pollution to the stratosphere, *Science*, *328*(5978), 611–613.

Rapp, M., J. M. C. Plane, B. Strelnikov, G. Stober, S. Ernst, J. Hedin, M. Friedrich, and U. P. Hoppe (2012), In situ observations of meteor smoke particles (MSP) during the Geminids 2010: Constraints on MSP size, work function and composition, *Ann. Geophys.*, *30*(12), 1661–1673, doi:10.5194/angeo-30-1661-2012.

Read, W. G., L. Froidevaux, and J. W. Waters (1993), Microwave limb sounder measurement of stratospheric SO_2 from the Mount Pinatubo volcano, *Geophys. Res. Lett.*, *20*, 1299–1302, doi:10.1029/93GL00831.

Reeves, J. M., J. C. Wilson, C. A. Brock, and T. P. Bui (2008), Comparison of aerosol extinction coefficients, surface area density, and volume density from SAGE II and in situ aircraft measurements, *J. Geophys. Res.*, *113*, D10202, doi:10.1029/2007JD009357.

Reid, J. S., R. Koppmann, T. F. Eck, and P. D. Eleuterio (2005), A review of biomass burning emissions part II: Intensive physical properties of biomass burning particles, *Atmos. Chem. Phys.*, *5*, 799–8825.

Reiner, T., and F. Arnold (1994), Laboratory investigations of gaseous sulfuric acid formation via $SO_3 + H_2O + M \rightarrow H_2SO_4 + M$: Measurement of the rate constant and product identification, *J. Chem. Phys.*, *101*, 7399–7407.

Rex, M., et al. (2014), A tropical West Pacific OH minimum and implications for stratospheric composition, *Atmos. Chem. Phys.*, *14*(9), 4827–4841, doi:10.5194/acp-14-4827-2014.

Ridley, D. A., et al. (2014), Total volcanic stratospheric aerosol optical depths and implications for global climate change, *Geophys. Res. Lett.*, *41*, 7763–7769, doi:10.1002/2014GL061541.

Rieger, L. A., A. E. Bourassa, and D. A. Degenstein (2014), Stratospheric aerosol particle size information in Odin-OSIRIS limb scatter spectra, *Atmos. Meas. Tech.*, *7*(2), 507–522, doi:10.5194/amt-7-507-2014.

Rieger, L. A., A. E. Bourassa, and D. A. Degenstein (2015), A merged SAGE II-OSIRIS stratospheric aerosol record, *J. Geophys. Res. Atmos.*, *120*, 8890–8904, doi:10.1002/2015JD023133.

Rinsland, C. P., M. R. Gunson, M. K. W. Ko, D. W. Weisenstein, R. Zander, M. C. Abrams, A. Goldman, N. D. Sze, and G. K. Yue (1995), H_2SO_4 photolysis—A source of sulfur-dioxide in the upper stratosphere, *Geophys. Res. Lett.*, *22*(9), 1109–1112, doi:10.1029/95GL00917.

Rinsland, C. P., L. Chiou, E. Mahieu, R. Zander, C. D. Boone, and P. F. Bernath (2008), Measurements of long-term changes in atmospheric OCS (carbonyl sulfide) from infrared solar observations, *J. Quant. Spectros. Radiat. Transfer*, *109*, 2679–2686.

Robinson, T. W., D. P. Schofield, and H. G. Kjaergaard (2003), High level ab initio studies of the excited states of sulfuric acid and sulfur trioxide, *J. Chem. Phys.*, *118*(16), 7226–7232, doi:10.1063/1.1561852.

Robock, A. (2000), Volcanic eruptions and climate, *Rev. Geophys.*, *38*(2), 191–219, doi:10.1029/1998RG000054.

Robock, A., and J. Mao (1995), The volcanic signal in surface temperature observations, *J. Clim.*, *8*, 1086–1103, doi:10.1175/1520-0442(1995)008,1086:TVSIST.2.0.CO;2.

Rogers, R. R., et al. (2011), Assessment of the CALIPSO Lidar 532 nm attenuated backscatter calibration using the NASA LaRC airborne high spectral resolution lidar, *Atmos. Chem. Phys.*, *11*(3), 1295–1311, doi:10.5194/acp-11-1295-2011.

Rose, W. I., and A. J. Durant (2009), Fine ash content of explosive eruptions, *J. Volcanol. Geotherm. Res.*, *186*(1–2), 32–39.
Rose, W. I., et al. (2006), Atmospheric chemistry of a 33–34 hour old volcanic cloud from Hekla Volcano (Iceland): Insights from direct sampling and the application of chemical box modeling, *J. Geophys. Res.*, *111*, D20206, doi:10.1029/2005JD006872.
Rosen, J. M. (1964), The vertical distribution of dust to 30 km, *J. Geophys. Res.*, *69*, 4673–4676, doi:10.1029/JZ069i021p04673.
Rosenfeld, D., M. Fromm, J. Trentmann, G. Luderer, M. O. Andreae, and R. Servranckx (2007), The Chisholm firestorm: Observed, precipitation and lightning activity of a pyro-cumulonimbus, *Atmos. Chem. Phys.*, *7*, 645–659.
Russell, P. B., T. J. Swissler, and M. P. McCormick (1979), Methodology for error analysis and simulation of lidar aerosol measurements, *Appl. Opt.*, *18*(22), 3783–3797, doi:10.1364/AO.18.003783.
Sander, S. P., et al. (2011), Chemical kinetics and photochemical data for use in atmospheric studies, *Rep. 10-6*, Jet Propulsion Laboratory, Pasadena.
Sandoval-Soto, L., M. Stanimirov, M. von Hobe, V. Schmitt, J. Valdes, A. Wild, and J. Kesselmeier (2005), Global uptake of carbonyl sulfide (COS) by terrestrial vegetation: Estimates corrected by deposition velocities normalized to the uptake of carbon dioxide (CO_2), *Biogeosciences*, *2*(2), 125–132.
Santer, B. D., et al. (2014), Volcanic contribution to decadal changes in tropospheric temperature, *Nat. Geosci.*, *7*, 185–189, doi:10.1038/NGEO2098.
Sato, M., J. E. Hansen, M. P. McCormick, and J. B. Pollack (1993), Stratospheric aerosol optical depths, 1850–1990, *J. Geophys. Res.*, *98*(D12), 22,987–22,994, doi:10.1029/93JD02553.
Saunders, R. W., et al. (2010), An aerosol chamber investigation of the heterogeneous ice nucleating potential of refractory nanoparticles, *Atmos. Chem. Phys.*, *10*(3), 1227–1247, doi:10.5194/acp-10-1227-2010.
Saunders, R. W., S. Dhomse, W. S. Tian, M. P. Chipperfield, and J. M. C. Plane (2012), Interactions of meteoric smoke particles with sulphuric acid in the Earth's stratosphere, *Atmos. Chem. Phys.*, *12*(10), 4387–4398, doi:10.5194/acp-12-4387-2012.
Scaillet, B. J., F. Luhr, and M. R. Carroll (2003), Petrological and volcanological constraints on volcanic sulfur emissions to the atmosphere, in *Volcanism and the Earth's Atmosphere*, edited by A. Robock and C. Oppenheimer, pp. 11–40, AGU, Washington D. C.
Schlager, H., and F. Arnold (1987), Balloon-borne composition measurements of stratospheric negative ions and inferred sulfuric acid vapour abundances during the MAP/GLOBUS campaign, *Plan. Space Sci.*, *35*, 693–701.
Schmidt, A., T. Thordarson, L. D. Oman, A. Robock, and S. Self (2012), Climatic impact of the long-lasting 1783 Laki eruption: Inapplicability of mass-independent sulfur isotopic composition measurements, *J. Geophys. Res.*, *117*, D23116, doi:10.1029/2012JD018414.
Schmidt, H., et al. (2013), Response of the middle atmosphere to anthropogenic and natural forcings in the CMIP5 simulations with the Max Planck Institute Earth system model, *J. Adv. Model. Earth Syst.*, *5*, 98–116, doi:10.1002/jame.20014.
Schneider, D. J., W. I. Rose, L. R. Coke, G. J. S. Bluth, I. E. Sprod, and A. J. Krueger (1999), Early evolution of a stratospheric volcanic eruption cloud as observed with TOMS and AVHRR, *J. Geophys. Res.*, *104*(D4), 4037–4050, doi:10.1029/1998JD200073.
Schumann, U., et al. (2011), Airborne observations of the Eyjafjalla volcano ash cloud over Europe during air space closure in April and May 2010, *Atmos. Chem. Phys.*, *11*(5), 2245–2279, doi:10.5194/acp-11-2245-2011.
Schwarz, J. P., et al. (2008), Coatings and their enhancement of black carbon light absorption in the tropical atmosphere, *J. Geophys. Res.*, *113*, D03203, doi:10.1029/2007JD009042.
Schwarz, J. P., B. H. Samset, A. E. Perring, J. R. Spackman, R. S. Gao, P. Stier, M. Schulz, F. L. Moore, E. A. Ray, and D. W. Fahey (2013), Global-scale seasonally resolved black carbon vertical profiles over the Pacific, *Geophys. Res. Lett.*, *40*, 5542–5547, doi:10.1002/2013GL057775.
Segschneider, J., A. Beitsch, C. Timmreck, V. Brovkin, T. Ilyina, J. Jungclaus, S. J. Lorenz, K. D. Six, and D. Zanchettin (2013), Impact of an extremely large magnitude volcanic eruption on the global climate and carbon cycle estimated from ensemble Earth System Model simulations, *Biogeosciences*, *10*, 669–687, doi:10.5194/bg-10-669-2013.
Seinfeld, J., and S. Pandis (2006), *Atmospheric Chemistry and Physics*, John Wiley, N. J.
Sekiya, T., K. Sudo, and T. Nagai (2016), Evolution of stratospheric sulfate aerosol from the 1991 Pinatubo eruption: Roles of aerosol microphysical processes, *J. Geophys. Res. Atmos.*, *121*, doi:10.1002/2015JD024313.
Sheng, J. (2014), Modeling stratospheric aerosols using a coupled aerosol-chemistry-climate model, PhD thesis, 96 pp., Swiss Federal Institute of Technology, ETH Zurich.
Sheng, J.-X., D. K. Weisenstein, B.-P. Luo, E. Rozanov, A. Stenke, J. Anet, H. Bingemer, and T. Peter (2015), Global atmospheric sulfur budget under volcanically quiescent conditions: Aerosol-chemistry-climate model predictions and validation, *J. Geophys. Res. Atmos.*, *120*, 256–276, doi:10.1002/2014JD021985.
Shepherd, T. G. (2002), Issues in stratosphere-troposphere coupling, *J. Meteorol. Soc. Jpn.*, *80*(4B), 769–792.
Siddaway, J. M., and S. V. Petelina (2011), Transport and evolution of the 2009 Australian Black Saturday bushfire smoke in the lower stratosphere observed by OSIRIS on Odin, *J. Geophys. Res.*, *116*, D06203, doi:10.1029/2010JD015162.
Sigl, M., et al. (2014), Insights from Antarctica on volcanic forcing during the Common Era, *Nat. Clim. Change*, *4*, 693–697, doi:10.1038/nclimate2293.
Sigmarsson, O., B. Haddadi, S. Carn, S. Moune, J. Gudnason, K. Yang, and L. Clarisse (2013), The sulfur budget of the 2011 Grímsvötn eruption, Iceland, *Geophys. Res. Lett.*, *40*, 6095–6100, doi:10.1002/2013GL057760.
Simkin, T., and R. Fiske (1983), *Krakatau 1883: The Volcanic Eruption and Its Effects*, Smithsonian Institution Press, Washington, D. C.
Sinnhuber, B.-M., and I. Folkins (2006), Estimating the contribution of bromoform to stratospheric bromine and its relation to dehydration in the tropical tropopause layer, *Atmos. Chem. Phys.*, *6*, 4755–4761.
Smith, S. J., J. van Aardenne, Z. Klimont, R. J. Andres, A. Volke, and S. D. Arias (2011), Anthropogenic sulfur dioxide emissions: 1850–2005, *Atmos. Chem. Phys.*, *11*, 1101–1116, doi:10.5194/acp-11-1101-2011.
Solomon, S., J. S. Daniel, R. R. Neely III, J. P. Vernier, E. G. Dutton, and L. W. Thomason (2011), The persistently variable "background" stratospheric aerosol layer and global climate change, *Science*, 866–870.
Stratosphere-troposphere Processes and their Role in Climate (SPARC) (2006), Assessment of Stratospheric Aerosol Properties (ASAP), *WCRP-124, WMO/TD No. 1295*, *SPARC Rep. 4*, 348 pp.
Steele, H. M., J. D. Lumpe, R. P. Turco, R. M. Bevilacqua, and S. T. Massie (1999), Retrieval of aerosol surface area and volume densities from extinction measurements: Application to POAM II and SAGE II, *J. Geophys. Res.*, *104*(D8), 9325–9336, doi:10.1029/1999JD900032.
Stenchikov, G. L., I. Kirchner, A. Robock, H.-F. Graf, J. C. Antuña, R. G. Grainger, A. Lambert, and L. Thomason (1998), Radiative forcing from the 1991 Mount Pinatubo volcanic eruption, *J. Geophys. Res.*, *103*(D12), 13,837–13,857, doi:10.1029/98JD00693.
Stenchikov, G., T. L. Delworth, V. Ramaswamy, R. J. Stouffer, A. Wittenberg, and F. Zeng (2009), Volcanic signals in oceans, *J. Geophys. Res.*, D16104, *114*, doi:10.1029/2008JD011673.
Stickel, R. E., M. Chin, E. P. Daykin, A. J. Hynes, P. H. Wine, and T. J. Wallington (1993), Mechanistic studies of the OH-initiated oxidation of CS2 in the presence of O_2, *J. Phys. Chem.*, *97*(51), 13,653–13,661.

Stimler, K., S. A. Montzka, J. A. Berry, Y. Rudich, and D. Yakir (2010a), Relationships between carbonyl sulfide (COS) and CO_2 during leaf gas exchange, *New Phytol.*, *186*(4), 869–878.
Stimler, K., D. Nelson, and D. Yakir (2010b), High precision measurements of atmospheric concentrations and plant exchange rates of carbonyl sulfide using mid-IR quantum cascade laser, *Global Change Biol.*, *16*(9), 2496–2503, doi:10.1111/j.1365-2486.2009.02088.x.
Stothers, R. B. (2001), Major optical depth perturbations to the stratosphere from volcanic eruptions: Stellar extinction period, 1961–1978, *J. Geophys. Res.*, *106*(D3), 2993–3003, doi:10.1029/2000JD900652.
Suntharalingam, P., A. J. Kettle, S. M. Montzka, and D. J. Jacob (2008), Global 3-D model analysis of the seasonal cycle of atmospheric carbonyl sulfide: Implications for terrestrial vegetation uptake, *Geophys. Res. Lett.*, *35*, L19801, doi:10.1029/2008GL034332.
Surono, J., et al. (2012), The 2010 explosive eruption of Java's Merapi volcano—A '100-year' event, *J. Volcanol. Geotherm. Res.*, *241–242*, 121–135, doi:10.1016/j.jvolgeores.2012.06.018.
Takigawa, M., M. Takahashi, and H. Akiyoshi (2002), Simulation of stratospheric sulfate aerosols using a Center for Climate System Research/National Institute for Environmental Studies atmospheric GCM with coupled chemistry 1. Nonvolcanic simulation, *J. Geophys. Res.*, *107*(D22), 4610, doi:10.1029/2001JD001007.
Tanaka, T. Y., K. Orito, T. T. Sekiyama, K. Shibata, and M. Chiba (2003), MASINGAR, a global tropospheric aerosol chemical transport model coupled with MRI/JMA98 GCM: Model description, *Pap. Meteorol. Geophys.*, *53*(4), 119–138, doi:10.2467/mripapers.53.119.
Taylor, S., J. H. Lever, and R. P. Harvey (1998), Accretion rate of cosmic spherules measured at the South Pole, *Nature*, *392*(6679), 899–903.
Textor, C., et al. (2006), Analysis and quantification of the diversities of aerosol life cycles within AeroCom, *Atmos. Chem. Phys.*, *6*, 1777–1813.
Thomas, H. E., I. M. Watsona, S. A. Carn, A. J. Prata, and V. J. Realmuto (2011), A comparison of AIRS, MODIS and OMI sulphur dioxide retrievals in volcanic clouds, *Geomatics, Nat. Hazards Risk*, *2*(3), doi:10.1080/19475705.2011.564212.
Thomason, L. W. (2012), Toward a combined SAGE II-HALOE aerosol climatology: An evaluation of HALOE version 19 stratospheric aerosol extinction coefficient observations, *Atmos. Chem. Phys.*, *12*(17), 8177–8188, doi:10.5194/acp-12-8177-2012.
Thomason, L. W., and L. R. Poole (1993), Use of stratospheric aerosol properties as diagnostics of Antarctic vortex processes, *J. Geophys. Res.*, *98*(D12), 23,003–23,012, doi:10.1029/93JD02461.
Thomason, L. W., and J. P. Vernier (2013), Improved SAGE II cloud/aerosol categorization and observations of the Asian tropopause aerosol layer: 1989–2005, *Atmos. Chem. Phys.*, *13*(9), 4605–4616, doi:10.5194/acp-13-4605-2013.
Thomason, L. W., L. R. Poole, and T. Deshler (1997), A global climatology of stratospheric aerosol surface area density deduced from Stratospheric Aerosol and Gas Experiment II measurements: 1984–1994, *J. Geophys. Res.*, *102*(D7), 8967–8976, doi:10.1029/96JD02962.
Thomason, L. W., S. P. Burton, B.-P. Luo, and T. Peter (2008), SAGE II measurements of stratospheric aerosol properties at non-volcanic levels, *Atmos. Chem. Phys.*, *8*, 983–995, doi:10.5194/acp-8-983-2008.
Thomason, L. W., J. R. Moore, M. C. Pitts, J. M. Zawodny, and E.-W. Chiou (2010), An evaluation of the SAGE III version 4 aerosol extinction coefficient and water vapor data products, *Atmos. Chem. Phys.*, *10*, 2159–2173.
Thompson, D. W. J., J. M. Wallace, P. D. Jones, and J. J. Kennedy (2009), Identifying signatures of natural climate variability in time series of global-mean surface temperature: Methodology and insights, *J. Clim.*, *22*, 6120–6141.
Thornton, D. C., A. R. Bandy, B. W. Blomquist, A. R. Driedger, and T. P. Wade (1999), Sulfur dioxide distribution over the Pacific Ocean 1991–1996, *J. Geophys. Res.*, *104*(D5), 5845–5854, doi:10.1029/1998JD100048.
Timmreck, C. (2012), Modeling the climatic effects of large explosive volcanic eruptions, *Wiley Interdiscip. Rev. Clim. Change*, *3*(6), 545–564, doi:10.1002/wcc.192.
Timmreck, C., S. J. Lorenz, T. J. Crowley, S. Kinne, T. J. Raddatz, M. A. Thomas, and J. H. Jungclaus (2009), Limited temperature response to the very large AD 1258 volcanic eruption, *Geophys. Res. Lett.*, *36*, L21708, doi:10.1029/2009GL040083.
Timmreck, C., H.-F. Graf, S. J. Lorenz, U. Niemeier, D. Zanchettin, D. Matei, J. H. Jungclaus, and T. J. Crowley (2010), Aerosol size confines climate response to volcanic super-eruptions, *Geophys. Res. Lett.*, *37*, L24705, doi:10.1029/2010GL045464.
Toohey, M., et al. (2013a), Characterizing sampling biases in the trace gas climatologies of the SPARC data initiative, *J. Geophys. Res. Atmos.*, *118*, 11,847–11,862, doi:10.1002/jgrd.50874.
Toohey, M., K. Krüger, and C. Timmreck (2013b), Volcanic sulfate deposition to Greenland and Antarctica: A modeling sensitivity study, *J. Geophys. Res. Atmos.*, *118*, 4788–4800, doi:10.1002/jgrd.50428.
Toohey, M., K. Krüger, M. Bittner, C. Timmreck, and H. Schmidt (2014), The impact of volcanic aerosol on the Northern Hemisphere stratospheric polar vortex: Mechanisms and sensitivity to forcing structure, *Atmos. Chem. Phys.*, *14*, 13,063–13,079, doi:10.5194/acp-14-13063-2014.
Trepte, C. R., and M. H. Hitchman (1992), Tropical stratospheric circulation deduced from satellite aerosol data, *Nature*, *355*, 626–628, doi:10.1038/355626a0.
Trickl, T., H. Giehl, H. Jäger, and H. Vogelmann (2013), 35 yr of stratospheric aerosol measurements at Garmisch-Partenkirchen: From Fuego to Eyjafjallajökull, and beyond, *Atmos. Chem. Phys.*, *13*, 5205–5225, doi:10.5194/acp-13-5205-2013.
Tzella, A., and B. Legras (2011), A Lagrangian view of convective sources for transport of air across the tropical tropopause layer: Distribution, times and the radiative influence of clouds, *Atmos. Chem. Phys.*, *11*, 12,517–12,534, doi:10.5194/acp-11-12517-2011.
Ulshöfer, V. S., and M. O. Andreae (1997), Carbonyl sulfide (COS) in the surface ocean and the atmospheric COS budget, *Aquat. Geochem.*, *3*(4), 283–303.
Vaida, V., H. G. Kjaergaard, P. E. Hintze, and D. J. Donaldson (2003), Photolysis of sulfuric acid vapor by visible solar radiation, *Science*, *299*(5612), 1566–1568, doi:10.1126/science.1079297.
van Diest, H., and J. Kesselmeier (2008), Soil atmosphere exchange of carbonyl sulfide (COS) regulated by diffusivity depending on water-filled pore space, *Biogeosciences*, *5*(2), 475–483.
van Noije, T. P. C., P. Le Sager, A. J. Segers, P. F. J. Van Velthoven, M. C. Krol, W. Hazeleger, A. G. Williams, and S. D. Chambers (2014), Simulation of tropospheric chemistry and aerosols with the climate model EC-Earth, *Geosci. Model Dev.*, *7*, 2435–2475, doi:10.5194/gmd-7-2435-2014.
Vanhellemont, F., et al. (2005), A 2003 stratospheric aerosol extinction and PSC climatology from GOMOS measurements on Envisat, *Atmos. Chem. Phys.*, *5*, 2413–2417.
Vanhellemont, F., et al. (2010), Optical extinction by upper tropospheric/stratospheric aerosols and clouds: GOMOS observations for the period 2002–2008, *Atmos. Chem. Phys.*, *10*(16), 7997–8009, doi:10.5194/acp-10-7997-2010.
Vehkamäki, H., M. Kulmala, I. Napari, K. E. J. Lehtinen, C. Timmreck, M. Noppel, and A. Laaksonen (2002), An improved parameterization for sulfuric acid water nucleation rates for tropospheric and stratospheric conditions, *J. Geophys. Res.*, *107*(D22), 4622, doi:10.1029/2002JD002184.
Vernier, J. P., et al. (2009), Tropical stratospheric aerosol layer from CALIPSO lidar observations, *J. Geophys. Res.*, *114*, D00H10, doi:10.1029/2009JD011946.

Vernier, J. P., L. W. Thomason, and J. Kar (2011c), CALIPSO detection of an Asian tropopause aerosol layer, *Geophys. Res. Lett.*, *38*, L07804, doi:10.1029/2010GL046614.

Vernier, J.-P., J. P. Pommereau, L. W. Thomason, J. Pelon, A. Garnier, T. Deshler, J. Jumelet, and J. K. Nielsen (2011a), Overshooting of clean tropospheric air in the tropical lower stratosphere as seen by the CALIPSO lidar, *Atmos. Chem. Phys.*, *11*, 9683–9696, doi:10.5194/acp-11-9683-2011.

Vernier, J.-P., et al. (2011b), Major influence of tropical volcanic eruptions on the stratospheric aerosol layer during the last decade, *Geophys. Res. Lett.*, *38*, L12807, doi:10.1029/2011GL047563.

Vernier, J.-P., T. D. Fairlie, M. Natarajan, F. G. Wienhold, J. Bian, B. G. Martinsson, S. Crumeyrolle, L. W. Thomason, and K. M. Bedka (2015), Increase in upper tropospheric and lower stratospheric aerosol levels and its potential connection with Asian pollution, *J. Geophys. Res. Atmos.*, *120*, 1608–1619, doi:10.1002/2014JD022372.

Vogel, B., G. Günther, R. Müller, J.-U. Grooß, and M. Riese (2015), Impact of different Asian source regions on the composition of the Asian monsoon anticyclone and on the extratropical lowermost stratosphere, *Atmos. Chem. Phys. Discuss.*, *15*, 9941–9995, doi:10.5194/acpd-15-9941-2015.

Volz, F. E. (1975), Distribution of turbidity after the 1912 Katmai eruption in Alaska, *J. Geophys. Res.*, *80*, 2643–2648, doi:10.1029/JC080i018p02643.

von Glasow, R. (2010), Atmospheric chemistry in volcanic plumes, *Proc. Natl. Acad. Sci. U.S.A.*, *107*(15), 6594–6599, doi:10.1073/pnas.0913164107.

von Hobe, M., R. G. Najjar, A. J. Kettle, and M. O. Andreae (2003), Photochemical and physical modeling of carbonyl sulfide in the ocean, *J. Geophys. Res.*, *108*(C7), 3229, doi:10.1029/2000JC000712.

Voulgarakis, A., et al. (2013), Analysis of present day and future OH and methane lifetime in the ACCMIP simulations, *Atmos. Chem. Phys.*, *13*(5), 2563–2587, doi:10.5194/acp-13-2563-2013.

Wandinger, U., A. Ansmann, J. Reichardt, and T. Deshler (1995), Determination of stratospheric aerosol microphysical properties from independent extinction and backscattering measurements with a Raman lidar, *Appl. Opt.*, *34*(36), 8315–8329, doi:10.1364/AO.34.008315.

Ward, S. M., T. Deshler, and A. Hertzog (2014), Quasi-Lagrangian measurements of nitric acid trihydrate formation over Antarctica, *J. Geophys. Res. Atmos.*, *119*, 245–258, doi:10.1002/2013JD020326.

Watts, S. F. (2000), The mass budgets of carbonyl sulfide, dimethyl sulfide, carbon disulfide and hydrogen sulfide, *Atmos. Environ.*, *34*(5), 761–779.

Waugh, D. W., and T. M. Hall (2002), Age of stratospheric air: Theory, observations and models, *Rev. Geophys.*, *40*(4), 1010, doi:10.1029/2000RG000101.

Weigel, R., et al. (2011), In situ observations of new particle formation in the tropical upper troposphere: The role of clouds and the nucleation mechanism, *Atmos. Chem. Phys.*, *11*, 9983–10,010.

Weigel, R., C. M. Volk, K. Kandler, E. Hosen, G. Gunther, B. Vogel, J. U. Grooss, S. Khaykin, G. V. Belyaev, and S. Borrmann (2014), Enhancements of the refractory submicron aerosol fraction in the Arctic polar vortex: Feature or exception?, *Atmos. Chem. Phys.*, *14*(22), 12,319–12,342, doi:10.5194/acp-14-12319-2014.

Weisenstein, D. K., G. K. Yue, M. K. W. Ko, N. D. Sze, J. M. Rodriguez, and C. J. Scott (1997), A two-dimensional model of sulfur species and aerosols, *J. Geophys. Res.*, *102*(11D), 13,019–13,035, doi:10.1029/97JD00901.

Weisenstein, D. K., J. E. Penner, M. Herzog, and X. Liu (2007), Global 2-D intercomparison of sectional and modal aerosol modules, *Atmos. Chem. Phys.*, *7*, 2339–2355, doi:10.5194/acp-7-2339-2007.

Wise, M. E., S. D. Brooks, R. M. Garland, D. J. Cziczo, S. T. Martin, and M. A. Tolbert (2003), Solubility and freezing effects of Fe2+ and Mg2+ in H_2SO_4 solutions representative of upper tropospheric and lower stratospheric sulfate particles, *J. Geophys. Res.*, *108*(D14), 4434, doi:10.1029/2003JD003420.

Xu, X., H. G. Bingemer, H.-W. Georgii, U. Schmidt, and U. Bartell (2001), Measurements of carbonyl sulfide (COS) in surface seawater and marine air, and estimates of the air-sea flux from observations during two Atlantic cruises, *J. Geophys. Res.*, *106*(D4), 3491–3502, doi:10.1029/2000JD900571.

Yu, P., O. B. Toon, R. R. Neely, B. G. Martinsson, and C. A. M. Brenninkmeijer (2015), Composition and physical properties of the Asian tropopause aerosol layer and the North American tropospheric aerosol layer, *Geophys. Res. Lett.*, *42*, 2540–2546, doi:10.1002/2015GL063181.

Yue, G. K., M. P. Mccormick, W. P. Chu, P. Wang, and M. T. Osborn (1989), Comparative studies of aerosol extinction measurements made by the SAM II and SAGE II satellite experiments, *J. Geophys. Res.*, *94*(D6), 8412–8424, doi:10.1029/JD094iD06p08412.

Yukimoto, S., et al. (2011), Meteorological Research Institute-Earth System Model Version 1 (MRI-ESM1)—Model description, *Technical Reports of the Meteorological Research Institute*, *No. 64*, doi:10.11483/mritechrepo.64.

Zanchettin, D., C. Timmreck, H.-F. Graf, A. Rubino, S. Lorenz, K. Lohmann, K. Krüger, and J. H. Jungclaus (2012), Bi-decadal variability excited in the coupled ocean-atmosphere system by strong tropical volcanic eruptions, *Clim. Dyn.*, *39*(1–2), 419–444.

Zanchettin, D., O. Bothe, H. F. Graf, S. J. Lorenz, J. Luterbacher, C. Timmreck, and J. H. Jungclaus (2013), Background conditions influence the decadal climate response to strong volcanic eruptions, *J. Geophys. Res. Atmos.*, *118*, 4090–4106, doi:10.1002/jgrd.50229.

Zanchettin, D., O. Bothe, C. Timmreck, J. Bader, A. Beitsch, H.-F. Graf, D. Notz, and J. H. Jungclaus (2014), Inter-hemispheric asymmetry in the sea-ice response to volcanic forcing simulated by MPI-ESM (COSMOS-Mill), *Earth Syst. Dyn.*, *5*, 223–242, doi:10.5194/esd-5-223-2014.

Zhu, Y., O. B. Toon, A. Lambert, D. E. Kinnison, M. Brakebusch, C. G. Bardeen, M. J. Mills, and J. M. English (2015), Development of a polar stratospheric cloud model within the Community Earth System Model using constraints on Type I PSCs from the 2010–2011 Arctic winter, *J. Adv. Model. Earth Syst.*, *7*, 551–585, doi:10.1002/2015MS000427.

Zhuo, Z., C. Gao, and Y. Pan (2014), Proxy evidence for China's monsoon precipitation response to volcanic aerosols over the past seven centuries, *J. Geophys. Res. Atmos.*, *119*, 6638–6652, doi:10.1002/2013JD021061.